December 2020

Investigation of SHOT1-binding ATPases in Arabidopsis thaliana

Sam Zelman

INVESTIGATION OF SHOT1-BINDING ATPASES IN *ARABIDOPSIS THALIANA*

A Thesis Presented

by

SAMUEL ZELMAN

Submitted to the Graduate School of the
University of Massachusetts Amherst in partial
fulfillment of the requirements for the degree of

MASTER OF SCIENCE

September 2020

Biochemistry and Molecular Biology

INVESTIGATION OF SHOT1-BINDING ATPASES IN *ARABIDOPSIS THALIANA*

A Thesis Presented

by

SAMUEL H. ZELMAN

Approved as to style and content by:

DocuSigned by:
Elizabeth Vierling
B8862A1BD280493...
Elizabeth Vierling, Chair

DocuSigned by:
Leonid Pobezinsky
662D3BC3DB66434...
Leonid Pobezinsky, Member

DocuSigned by:
Amy Springer
3CA40F175C394BC...
Amy Springer, Member

DocuSigned by:
Jennifer Normanly
7265AE30ED10469...
Dr. Jennifer Normanly, Department Head

Biochemistry and Molecular Biology

DEDICATION

I dedicate this work to my parents Alex and Ida, as well as my brother Simon. Without their unending love and support, this work would not have been possible.

ACKNOWLEDGMENTS

Firstly, I would like to thank my advisor, Dr. Elizabeth Vierling. Her constant guidance, support, and vested interest in my success have molded me into the scientist I am today. I will be forever grateful for the many opportunities afforded to me over the past three years in Dr. Vierling's lab. I would also like to express gratitude to the members of my committee, Drs. Springer and Pobezinsky, for their guidance and advice in the creation of this work.

I want to thank Dr. Minsoo Kim for his tireless technical support and mentorship, from which I learned many key skills and techniques that helped immensely throughout this work. I'd also like to thank Dr. Kim for providing materials such as plasmid vectors and transgenic plants for the purposes of my research. I would like to express my gratitude to Dr. Patrick Treffon for his immense help in assay/equipment training and development, without which many of the data in this work would not have been possible to acquire. Next, I would like to thank Dr. Jim Chambers from the Light Microscopy Facility for his help with training and use of the LMF.

A special thank you to Dr. Normanly for the fantastic opportunity to work with her in the teaching labs. The many teaching skills I learned from her helped to better my own scientific habits and practices. Finally, a big thank-you to all the members of the Vierling Lab whose support and friendship kept me on course throughout my time as a researcher.

This work was made possible by a grant from the National Science Foundation (IOS-1354960).

ABSTRACT

INVESTIGATION OF SHOT1-BINDING ATPASES IN ARABIDOPSIS THALIANA

SEPTEMBER 2020

SAMUEL ZELMAN, B.S., UNIVERSITY OF MASSACHUSETTS AMHERST

M.S., UNIVERSITY OF MASSACHUSETTS AMHERST

Directed by: Professor Elizabeth Vierling, Ph.D

Mitochondria play critical roles not only in primary metabolism as a central organelle for ATP generation, but also in responding to abiotic stresses. We identified a mutation in the *MTERF18 (Mitochondrial Transcription Termination factor)/SHOT1* (*Suppressor of hot1-4 1*) gene in *Arabidopsis thaliana* that enables plants to better tolerate heat and oxidative stresses, presumably due to reduced oxidative damage, but the exact molecular mechanism of the heat tolerance is unknown. In order to reveal the stress tolerance mechanisms of *mterf18*/*shot1* mutations, it is critical to understand the molecular defects of the mutant and to identify the molecular targets of the MTERF18/SHOT1 protein. MTERF18/SHOT1, a mitochondrial matrix protein, was found to bind to membrane-spanning mitochondrial AAA+ proteins homologous to ATAD3a of humans and other multicellular eukaryotes. *A. thaliana* has four ATAD3a homologues in two clades, and plants require one gene from each clade for viability. Previous studies of the topology and ATPase activity of ATAD3a suggest a role in endoplasmic reticulum (ER)-mitochondria contact sites. These sites are poorly defined in plants, and their relationship to heat stress tolerance is intriguing. To better understand ATAD3 function I expressed and purified the soluble, matrix-located, catalytic C-terminal ATPase domain of these proteins in order to assay their ATPase activity and oligomerization states. Transgenic plants with fluorescently labelled ER and mitochondria have been generated to observe effects of the MTERF18/SHOT1 mutation on ER-mitochondria dynamics. These studies of the four ATAD3 proteins will provide insights into ER-mitochondrial contact sites in plants, and into their link to MTERF18/SHOT1 and heat stress tolerance. I also provide a review of our current knowledge of ER-mitochondria contact site protein components in plants with reference to these proteins in *A. thaliana*.

TABLE OF CONTENTS

Page

LIST OF TABLES

LIST OF FIGURES

CHAPTER 1: ARABIDOPSIS HEAT STRESS AND THE MITOCHONDRION

1.1. Hsp101 is required for heat tolerance in plants

Plants, as sessile organisms, operate under a unique set of constraints in terms of homeostatic response. Because of their inability to move, homeostatic processes such as thermo- and drought-tolerance must be regulated through an intricate network of biological and biochemical responses. It is well established that plants and other organisms have a higher propensity to tolerate normally lethal heat stress conditions after acclimation at moderate temperatures (Vierling 1991). To define components of the plant thermotolerance pathway, ethane methyl sulfonate (EMS) was used to generate point mutants in *Arabidopsis thaliana* plants to identify genes that are integral to heat stress response. These mutants were then assessed for thermotolerance and mapped to the *A. thaliana* genome. Through this screen, multiple mutant alleles of the chaperone HSP101 (AGI: AT1G74310) were identified. This specific protein is a member of the Hsp101/ClpB protein family (Queitsch et al., 2000; Hong and Vierling 2000, 2001). Proteins of this family are known to participate in refolding proteins that have lost their function due to heat stress-mediated denaturation and aggregation (Parsell and Lindquist, 1993; Zavilgelsky et al., 2020). These data defined a key piece of the plant thermotolerance mechanism and highlighted the importance of protein homeostasis.

Multiple alleles of Hsp101 were discovered and named sequentially as *hot1-[x]* due to their loss of growth after heat stress (Lee et al., 2005). Thermotolerance was assessed using an assay of hypocotyl elongation (Kim et al., 2017), described in further detail in Chapter II. The first two mutants that were characterized were *hot1-1* (missense; E637K) and *hot1-3* (null, T-DNA insertion in exon 3) (Hong and Vierling, 2000, 2001). At optimal temperatures, Hsp101 mutations did not cause any significant changes to plant growth or development. Additional

screening identified more heat sensitive *hot1* alleles that also lacked thermotolerance at 45ºC, even after acclimation at moderate temperatures. Mutants identified were mapped to the *A. thaliana* genome and one was found within the HSP101 region and named *hot1-4* (A499T) (Lee et al., 2005). This alanine to threonine mutation was localized to a unique Hsp100/ClpB coiled-coil linker region. Studies with the *E. coli* homologue ClpB showed that the deleting the coiled-coil region did not affect *in vitro* oligomerization but did severely limit *in vitro* ATPase activity (Mogk et al., 2003). Conversely, *in vivo* studies show that loss of the coiled-coil linker region causes loss of thermotolerance (Mogk et al., 2003; DeSantis and Shorter, 2012). Notably, the *hot1-4* mutant showed inhibited growth at acclimation temperatures (38 ºC), a temperature that is permissive for wild type and the treatment that is necessary for acclimation to 45 ºC (Lee et al., 2005). Thus, the *hot1-4* allele acts in a dominant negative fashion to inhibit acclimation to high temperature.

1.2. Defining new aspects of plant thermotolerance

To identify factors involved in the *hot1-4* phenotype and to further define the plant thermotolerance pathway, Vierling and colleagues used EMS to mutagenize *hot1-4* and screened seedlings to identify both intragenic and extragenic suppressors of the *hot1-4* phenotype. This screen identified 43 total suppressors, of which 4 were found to be extragenic (Lee et al., 2005). Further research focused on the extragenic suppressors of *hot1-4*, with the goal of identifying partners involved in Hsp101 function or to identify independent pathways required for plant thermotolerance. The gene encoding one of these extragenic suppressors (AGI: AT3G60400), named *shot1-1* for suppressor of *hot1-4*, was cloned and found to be a mutation within an mTERF (mitochondrial transcription termination factor) protein (Lee et al., 2005). The first protein of this family to be characterized was human mTERF1, which was observed to function in transcription

termination by binding mitochondrial rRNA. SHOT1 was subsequently named mTERF18 in an analysis of the mTERF family of proteins in *A. thaliana* (Kruse et al., 1989). The main structural characteristics of mTERF proteins are mTERF motifs, which are two α-helices followed by a 3_{10} helix (Yakubovskaya et al., 2010). The SHOT1/mTERF18 protein contains five of these mTERF motifs, identified in Figure 1.1A. The *shot1-1* allele contains a point mutation upstream of the first mTERF motif, which causes a Gly to Asp conversion (Kim et al., 2012). The second allele of SHOT1/mTERF18 to be identified, known as *shot1-2*, is a T-DNA insertion following the last mTERF motif. This mutation causes a 44 amino acid truncation due to an in-frame stop codon, which was confirmed by RT-PCR (Kim et al., 2012). Both *shot1-1* and *shot1-2* displayed a retarded growth phenotype. However, both mutants also showed growth after heat stress in the dominant-negative *hot1-4* background (Figure 1.1B), indicating that SHOT1/mTERF18 mutation caused an HSP101-independent restoration of thermotolerance (Kim et al., 2012). Mutations in mitochondrial mTERF proteins had not previously been identified in plants, and the *shot1* mutants offered an opportunity to investigate their functions. Examining SHOT1 interactions with other plant proteins provided a promising next step in defining the plant thermotolerance pathway.

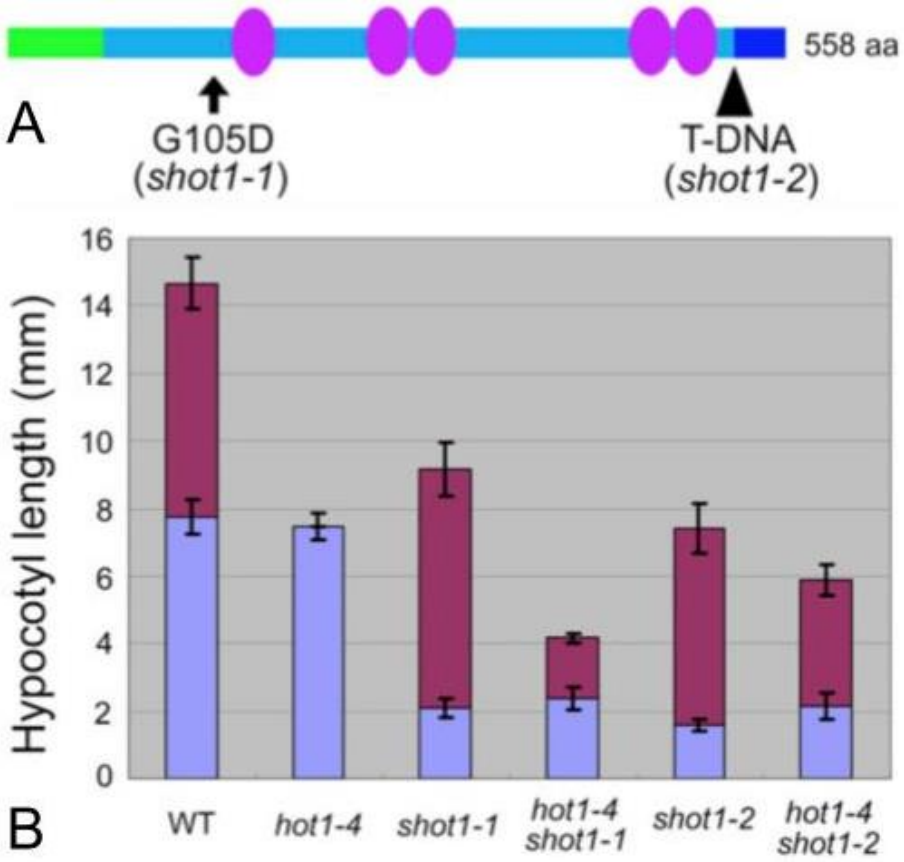

Figure 1.1: Domain organization and thermotolerance of *shot1* alleles. (A) Linear representation of the SHOT1 protein. Green and dark blue regions indicate N- and C-termini, respectively. Purple ovals indicate location of mTERF motifs. The locations of the point mutant *shot1-1* and C-terminal truncation mutant *shot1-2* are indicated by black arrows. (B) Heat stress tolerance of WT, *hot1-4*, and *shot1* plants. Violet and maroon bars show hypocotyl elongation before and after heat stress, respectively. Data adapted from Kim et al., 2012.

1.3. SHOT1 binds mtDNA and interacts with mitochondrial ATPases

Previous reports had shown mTERF1 in humans was actively bound to mtDNA (Kruse et al., 1989). SHOT1/mTERF18 was also to bind mtDNA by chemical crosslinking of DNA-protein interactions in isolated mitochondria from *shot1-2* plants transformed with SHOT1-GFP, followed by enrichment of SHOT1-bound nucleotides by GFP-Trap enrichment and sequencing. These experiments confirmed that SHOT1 binds mtDNA but did not reveal any evidence that

SHOT1/mTERF18 regulates transcription or translation of the mitochondrial genome (Kim et al., 2020).

As an additional approach to investigating protein function, experiments were performed to identify SHOT1/mTERF18 interacting partners. Mitochondria prepared from plants transformed with a SHOT1-GFP construct were used for immunoprecipitation/mass spectrometry (IP/MS). These experiments showed specific enrichment of three mitochondrial AAA (ATPase associated with diverse cellular activity) family proteins across all samples (Kim et al., 2020). Sequence similarity showed that these proteins were homologous to human ATAD3a (ATPase family AAA-domain containing protein 3a). Though not found in the IP/MS experiments, a fourth ATAD3a homolog was identified through sequence similarity to the other three proteins (Kim et al., 2020). These four proteins were named SBA proteins (SHOT1-binding ATPase) and will be referred to as SBA1 (AT3G03060), SBA2 (AT5G16930), SBA3 (AT2G18330), and SBA4 (AT4G36580) throughout the rest of this work. This result was significant given that no ATAD3a homologue had previously been identified in *A. thaliana*. Previous work on ATAD3a in other model organisms (discussed in subsequent sections) had shown that ATAD3a displayed a very interesting localization pattern: though its C-terminus resided within the mitochondrial matrix, its N-terminal domain was able to span across both the mitochondrial inner and outer membranes, and protrude through to the cytosol (Gilquin et al., 2010; Baudier, 2018). This unique membrane-spanning orientation led to ATAD3a being identified as one of the first proteins to bridge the mitochondria-ER contact sites (Csordas et al., 2019). These contact sites regulate multiple processes through organellar crosstalk (defined in further sections), but are poorly described in plants. Discovery of ATAD3a homologs in *A. thaliana* therefore represented a unique opportunity to investigate the dynamics of these contact sites and to perhaps identify the HSP101-independent restoration of thermotolerance in *shot1-2*.

1.4. Mitochondrial protein complexes and their connections to ATAD3a

Modern day mitochondria arose from the phagocytosis of ancient alpha-proteobacteria by early eukaryotic organisms billions of years ago (Anderson et al., 2019). Due to this origin, mitochondria are divided into four distinct compartments: the outer membrane (MOM), the intermembrane space (IMS), the inner membrane (IMM), and the matrix (Anderson et al., 2019). Discrete functions are performed at the interfaces between the different compartments, such as protein import and assembly, lipid metabolism, and mtDNA maintenance (Wideman and Munoz-Gomez, 2016). Many of these processes are dependent not only on components of the four mitochondrial compartments, but also on the association of the mitochondria with organelles such as the ER (Wideman and Munoz-Gomez, 2016; Baudier, 2018). To define the characteristic complexes that comprise these separate functions, the system was broadly defined as the ER-mitochondria organizing network, or ERMIONE. This supercomplex contains multiple sub-complexes and associated proteins, each with distinct features and functions. Roughly, the two most well-characterized subcomplexes of the ERMIONE are the mitochondrial cristae organizing system (MICOS) and ER-mitochondria encounter structure (ERMES). Additionally, the function of the ERMIONE is dependent upon a novel membrane, known as the mitochondria-associated membrane (MAM). This region is typically defined as the area in which the inner membrane is closely tethered to the outer membrane, which itself is in contact with the ER membrane (Csordas et al., 2018). Both of these systems, as well as other accessory systems of the ERMIONE are defined in greater detail in Chapter V.

So far, protein components of ERMES have only been identified in yeast, but not in humans or plants (Wideman and Munoz-Gomez, 2016). As its name suggests, the ERMES system is primarily responsible for tethering the ER and mitochondria together. This tethering is key for mitochondrial fission/fusion, as well as some of the protein and lipid exchange occurring

at the membrane interface of the two organelles (Wideman and Munoz-Gomez, 2016; Kundu and Pasrija, 2020).

MICOS protein components are the more conserved system in eukaryotes. All eukaryotes possess at least one subunit of the MICOS system (Wideman and Munoz-Gomez, 2016). While ERMES is hypothesized to reside on the MOM, the MICOS system is typically localized to specific puncta on the MIM that are proximal to crista boundary membrane and crista junctions (Friedman et al., 2018). It is at those locations that the MICOS system performs its functions of cristae biogenesis and distribution, mtDNA maintenance, and cholesterol biosynthesis (Baudier, 2018; Gerhold et al., 2015). More details of the roles of individual MICOS subunits and their specific functions can be found in Chapter V. Importantly, in humans, yeast, and plants perturbation of key MICOS complex subunits almost always results in malformed/defective cristae, defective respiration, and altered mitochondrial morphology (Friedman et al., 2018; Wollweber et al., 2017; Michaud et al., 2016; Baudier, 2018). Based on previous data, some researchers believe that ATAD3a is a MICOS protein, an idea that will be focused on throughout the rest of this work.

1.5. ATAD3 proteins

1.5.1. Genetic information

The discovery of ATAD3 homologues in plants presents a unique research opportunity. As mentioned previously, both ATAD3a and mitochondria-ER contact sites (MERCs) remain unstudied in any plant systems. Additionally, phylogenetic analyses predict the existence of the MICOS system in plants, but only one MICOS protein has so far been identified in plants (Michaud et al., 2016). As a result, the study of ATAD3a and SBA proteins represents a novel opportunity to learn about the dynamics of MERCs in plants. The *ATAD3a* gene is conserved in

multicellular organisms, providing some background on the role of its plant homologs. However, studies on this gene and its protein product have focused almost exclusively on human, fruit fly, and mouse ATAD3 (Baudier, 2018). Flies and mice contain only the ATAD3a gene, while humans contain three genes (*ATAD3a, ATAD3b,* and *ATAD3c*) due to multiple duplication events (Baudier, 2018). Of these genes, *ATAD3a* produces one predominant isoform [UniProtKB Q9NVI7-2, 586 amino acids] (Merle et al., 2012).

1.5.2. ATAD3a localization and topology

Sequence analysis of the human ATAD3a identified multiple conserved domains and motifs (Figure 1.2A). The first of these is the proline rich motif (PRM), a short region that has been shown to assist in membrane anchoring and protein-protein interactions (Baudier, 2018). This region is followed by two 3,4 heptad coiled-coil domains (CC) that are responsible for oligomerization of ATAD3a monomers (Gilquin et al., 2010). Predictive software (HMMTOP; Tusnady and Simon 1999, 2001) for amphipathic transmembrane domains has predicted two such successive domains on human ATAD3a that are separated by a five amino acid linker. The same predictive program also indicates a large amphipathic moment in the first TM domain, but not for the second (Baudier, 2018).

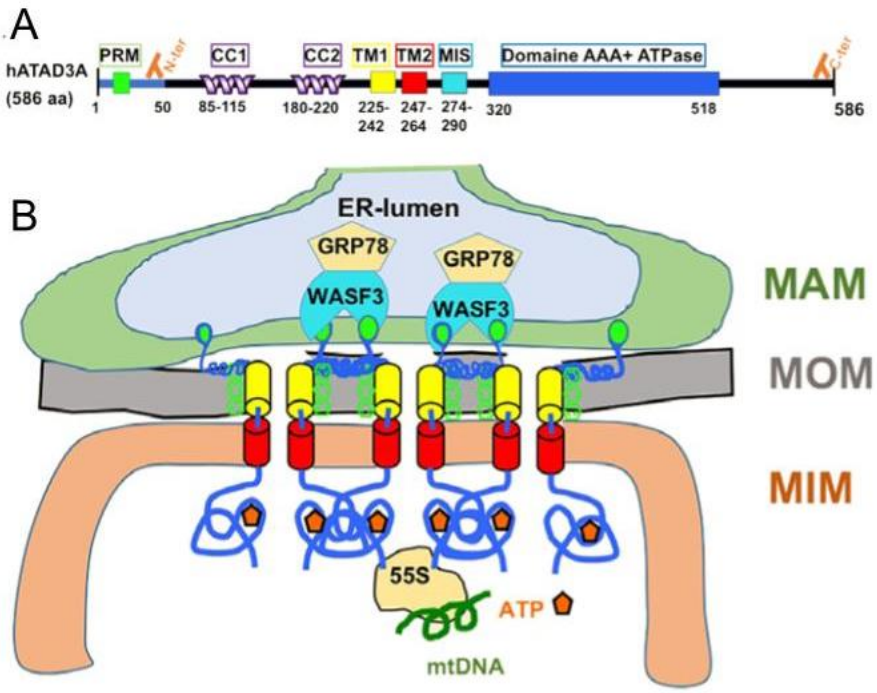

Figure 1.2: Domain organization and model of the human mitochondrial ATAD3a protein. **(A)** Domain organization of ATAD3a. The protein comprises 586 amino acids, including a proline-rich motif (PRM), two coiled-coil domains (CC), two transmembrane helices (TM), a mitochondrial import sequence (MIS), and AAA+ domain. **(B)** Modelling the membrane localization of human ATAD3a. Biochemical analyses propose that ATAD3a retains its C-terminus in the mitochondrial matrix and is involved in ribosomal and mtDNA binding. The two transmembrane regions orient perpendicular to the mitochondrial inner membrane (MIM) and mitochondrial outer membrane (MOM), allowing the N-terminal PRM to interact with the endoplasmic reticulum at the mitochondria-associated membrane (MAM). Data adapted from Baudier, 2018, and Gilquin et al., 2010.

These data would indicate that TM2 is able to span the inner membrane, while TM1 remains parallel and provides a scaffold for the N-terminus to protrude through the outer membrane towards the ER. Though most mitochondria-localized proteins contain an import sequence on their N-terminus, the mitochondrial targeting sequence of ATAD3a is located following the second TM domain (Fig. 1.2A). This finding was confirmed using expression of truncation proteins, where it was observed that ATAD3a 1-220 did not localize to mitochondria

in human cell lines, but ATAD3a 1-250 does (Gilquin et al., 2010). The most conserved domain of ATAD3a is the C-terminal ATPase domain. Within this domain are the Walker A and Walker B sequence motifs for the binding and hydrolysis of ATP (Mogk et al., 2003), as well as an arginine finger and SRH (second region of homology) motif (Gilquin et al., 2010).

The exact localization of ATAD3a within mitochondria is a complicated topic. Mitochondria are enveloped in an outer membrane (MOM), as well as an inner membrane (MIM). Furthermore, invaginations within the inner membrane create crista membranes and crista junctions. In the proximity of mitochondria-ER contact sites (MERCs), it has been observed that the crista junctions, MIM, and MOM are "scrunched" together to form a complex milieu referred to as the mitochondria-associated membrane (MAM). Gilquin et al. (2010) performed studies to understand ATAD3a localization within these membranes. Truncated and fluorescently tagged ATAD3a proteins were expressed in human cell lines, from which mitochondria were purified and subjected to selective membrane solubilization/permeabilization experiments, as well as protease accessibility assays. The authors concluded that the C-terminal ATPase domain resides within the mitochondrial matrix, where it may interact with mtDNA. The N-terminal region of ATAD3a protrudes through to the surface of the MOM, where it may interact with the ER membrane (Gilquin et al., 2010). Additionally, fluorescently tagged ATAD3a 1-220 (lacking the mitochondrial import sequence) produced a staining pattern highly similar to that of fluorescently tagged protein disulfide isomerase (PDI), a known ER lumen protein. These data suggest that the ATAD3a N-terminus contains an ER-specific localization sequence as well (Gilquin et al., 2010). This observation was further developed by data showing that PRM domains can also facilitate membrane anchoring (Ren and Hurley, 2011). Finally, fluorescence microscopy of the whole ATAD3a protein in Leydig cells shows colocalization of fluorescent signals of ATAD3a with those of MAM markers (Issop et al., 2015). These observations sum to the conclusion that

ATAD3a spans both mitochondrial membranes and is therefore a MERC linker protein that functionally tethers the two organelles without the presence of other complexes (Csordas et al., 2018).

1.5.4. Oligomeric state of ATAD3a

Biochemical properties of ATAD3a are better understood through the lens of other AAA (ATPase associated with diverse cellular activities) proteins. AAA proteins are well conserved, as they have been identified in both prokaryotes and eukaryotes (Vale, 2007). As their name implies, AAA proteins perform a wide variety of functions such as proteolytic cleavage, DNA unwinding (helicase), and chaperoning (Lupas and Martin, 2002). To mediate these activities, AAA proteins are dependent on conserved sequence features. The first of these is known as the Walker A motif, responsible for nucleotide binding. It is denoted by a conserved GKT/S motif wherein the lysine residue is necessary for contacting the γ-phosphate of ATP to stabilize the protein-nucleotide interaction (Wiese et al., 2006). The second motif, known as Walker B, catalyzes the removal of the γ-phosphate from ATP and is typically recognized as a DEAD box motif (Wiese et al., 2006). The use of a Mg^{+2} cofactor in the enzymatic removal of phosphate is key, as it stabilizes anionic reaction intermediates and activates ATP for nucleophilic attack (Zimmerman et al., 1998). Importantly, each AAA+ domain contains each of these motifs. Proteins with multiple AAA+ domains will therefore contain multiple Walker A and Walker B motifs.

AAA proteins tend to operate as oligomers and to follow discrete oligomerization patterns. The majority of proteins containing a single AAA domain tend to form ring shaped hexamers that feature a central pore (Vale, 2000; Lupas and Martin, 2002). The oligomerization of these proteins is dependent on substrate binding or nucleotide binding, while absence of either results in a predominantly monomeric structure (Vale, 2000). Proteins containing multiple AAA

domains (such as ClpB) follow a similar pattern and form a dual, stacked hexameric ring structure (Vale, 2007). Interestingly, the formation of the dual ring structure is solely nucleotide-binding dependent. Blockage of the nucleotide binding region/Walker A motif, or release of nucleotides causes the superstructure to dissociate to the monomeric state (Vale, 2007). *In vitro* studies using proteins with two AAA domains, such as ClpB, showed that blockage of one nucleotide binding motif is insufficient to cause full dissociation of the oligomer. However, blockage of Walker A/nucleotide binding regions in both AAA domains caused complete monomerization, demonstrating that the oligomeric state of AAA proteins is dependent upon nucleotide binding (Mogk et al., 2003).

As mentioned previously, ATAD3a contains two coiled-coil domains that serve as a scaffold for oligomerization (Gilquin et al., 2010). *In vivo* crosslinking has tested the oligomeric state of ATAD3a, but with sometimes conflicting data. In crude mitochondria from human U373 cells, application of the water-soluble crosslinker 3,3'-dithiobis- (sulfosuccinimidyl propionate) (DTSSP) showed that ATAD3a was mostly oligomerized as dimers, and to a smaller extent as tetramers and hexamers (Baudier, 2018). Since DTSSP is unable to penetrate membranes, these data would suggest that at least some portion of the ATAD3a N-terminus remains outside of the MOM, making them accessible to the crosslinking agent. Conversely, application of the membrane-soluble crosslinker dithiobis-(succinimidyl propionate) (DSP) and subsequent immunoblotting showed that nearly all of the ATAD3a protein was present in hexameric complexes. Taken together, these studies concluded that ATAD3a most likely hexamerizes, and localizes much of this complex within the matrix compartment (Baudier, 2018). However, crosslinking using bismaleimidohexane (BMH) in human neuronal cells has indicated that ATAD3a may form dimers, leading to lingering questions about the oligomeric state of ATAD3a (Zhao et al., 2019).

1.5.5. ATAD3a mutant phenotypes

As mentioned earlier, MICOS subunit mutants typically display phenotypes related to malformed cristae, altered mitochondrial morphology, and impacted respiration (Friedman et al., 2018; Wollweber et al., 2017; Michaud et al., 2016; Baudier 2018). Interestingly, mutants of ATAD3a show similar characteristics, many of which are dependent upon the oligomeric state of ATAD3a. Expression of ATAD3a proteins deficient in oligomerization (through loss of ATP binding due to mutation of the Walker A motif) results in a mitochondrial fragmentation phenotype, as well as loss of contact between the inner and outer mitochondrial membranes (Gilquin et al., 2010). One hypothesis for the two phenomena is that loss of ATP binding ablates oligomerization, which in turn reduces interactions with the mitochondrial outer membrane, a key player in MERCs. Considering that co-translational import of protein from the ER to the mitochondria is dependent upon functional tethering, loss of the ATAD3a tether at the mitochondrial outer membrane is believed to activate the ER stress response, leading to the mitochondrial fragmentation phenotype (Gilquin et al., 2010; Gadir et al., 2011; Baudier 2018).

Recent studies have posited that mitochondrial fission via the DRP1 pathway typically invokes a stress response in order to destroy damaged mitochondria via mitophagy (Zorov et al., 2019). Previous work with ATAD3a in human neuronal cells also showed that overexpression of ATAD3a triggers this pathway as well (Cooper et al., 2017; Zhao et al., 2019). Overall, this suggests that perturbation of ATAD3a oligomerization triggers DRP1 fission machinery for the beginning of mitophagy. Considering that plants contain two DRP1 homologs (DRP3a, AT4G33650; DRP3B, AT2G14120), it remains possible that the oligomeric state of SBA proteins can control the overall health and function of plant mitochondria.

Similar phenotypes of ATAD3a mutants have been observed in mice. Using a Cre-Lox recombinase system, it was observed that ATAD3a knockout caused massive changes in

mitochondrial dynamics (Peralta et al., 2018). Among these, severe morphological changes could be seen in the cristae, where nearly all cristae within each mitochondrion were distributed to only one side of the organelle. Additionally, the number of cristae junctions in each mitochondrion was significantly decreased as compared to wild-type mitochondria. ATAD3a-KO mitochondria also exhibited increased mitochondrial fragmentation phenotypes, indicative of mitochondrial dysfunction. In addition to structural irregularities, ATAD3a knockout mitochondria showed increased rates of mtDNA breakpoint mutations as compared to mtDNA from wild-type mice. This result indicates that ATAD3a is somehow involved in mtDNA maintenance, a role typically assigned to the MICOS complex. None of these effects were seen in control mitochondria, suggesting that knockout of ATAD3a severely affected mitochondrial function (Peralta et al., 2018). In addition to changes in cristae, the same authors noticed that high-molecular weight MICOS complexes were destabilized in ATAD3a KO cells (Peralta et al., 2018), showing that ATAD3a performs some role by which it interacts with the MICOS system.

Other characteristics of ATAD3a mutants display similar phenotypes to MICOS mutants. Perturbation of ATAD3a interfered with the mitochondrial cholesterol metabolome, inhibiting proper import of cholesterol precursors and altering cholesterol distribution along the mitochondrial inner membrane (Issop et al., 2015; He et al., 2012). This observation led to the hypothesis that cholesterol scaffolds are somehow involved with nucleoid maintenance, and that ATAD3a knockdown led to changes in the mtDNA replication platform (Baudier, 2018). Finally, He et al. (2012) also showed that ATAD3a knockdown severely impacted the rate of mitochondrial protein synthesis, suggesting that ATAD3a has associations with not only mtDNA, but also with the mitochondrial protein synthesis machinery. Though the oligomeric state of ATAD3a was not assayed in many of the above publications, it does remain possible that

knockdown/mutation of ATAD3a and subsequent oligomeric defects may be responsible for loss of function.

1.6. Guiding questions and experimental rationale

Given the known information about ATAD3a and the homologous SBA proteins that the Vierling lab discovered interact with SHOT1/mTERF18, two main questions were formulated to guide the research throughout the rest of this work. The first was, "What is the oligomeric state of SBA proteins?" This question is addressed in Chapter III. In work discussed throughout the introduction, it is seen that the oligomeric state of ATAD3a impacts mitochondrial dynamics and influences multiple processes. Currently, the oligomeric state of the SBA proteins is unknown. It is also unknown if SBA oligomeric state impacts their function in plants, especially functions relating to the heat stress response. Additionally, there are four SBA proteins in *A. thaliana* as compared to only one ATAD3a found in most other model systems. The functional relationship between these four proteins remains unknown. It is plausible that either each SBA protein performs discrete functions, or that they are functionally redundant. One hypothesis is that they are each necessary to form hetero-oligomeric complexes, but lack of SBA protein data keeps this question unanswered.

The second question posed in this work was "Does *shot1-2* impact mitochondria-ER dynamics?" As described above, *shot1-2* restores heat tolerance independently of the HSP101 pathway, though this separate pathway has not been fully defined. Based on the observation that ER-mitochondria contact sites are a scaffold for processes to occur during stress conditions (Mueller and Reski, 2015), is it possible that *shot1-2* somehow promotes a process at this interface to restore thermotolerance in plants? For this reason, I decided to review the dynamics at the ER-mitochondria interface to determine what, if any, changes occur in the *shot1-2* mutant.

Chapter II contains all information relevant to the materials and methods used for all experimental and in silico work in this thesis. In chapters III and IV, experimental data addressing the aforementioned questions are presented, along with conclusions. Chapter V contains an in-depth overview of the ERMIONE system through the lens of plants. Known ERMIONE subsystems are defined and compared to observed ERMIONE components in plants.

CHAPTER 2: MATERIALS AND METHODS

2.1. Bacterial strains and plasmids

1) *Escherichia coli* Subcloning Efficiency DH5α, genotype F- 80dlacZ M15 (lacZYA-argF) U169 recA1 endA1hsdR17(rk-, mk+) phoAsupE44 -thi-1 gyrA96 relA1 (New England Biolabs) was used for plasmid transformation and storage for non-pCR8 based vectors.
2) *E. coli* OneShot TOP10 Chemically Competent cells, genotype F^- *mcr*A Δ(*mrr-hsd*RMS-*mcr*BC) φ80*lac*ZΔM15 Δ*lac*X74 *rec*A1 *ara*D139 Δ(*ara-leu*)7697 *gal*U *gal*K λ^- *rps*L(Str^R) *end*A1 *nup*G (ThermoFisher Scientific) was used for plasmid transformation and storage for pCR8-based vectors.
3) *E. coli* BL21 (λDE3) pLysS, genotype F^- *omp*T *hsd*S_B (r_B^-, m_B^-) *gal dcm* (DE3) pLysS(Cam^R)
4) *Agrobacterium tumefaciens* GV3101, genotype C58 (rif R) Ti pMP90 (pTiC58DT-DNA) (gentR) Nopaline

Plasmids used throughout this work are listed in Tables 2.1, 2.2, and 2.3 attached separately to this document.

2.2. Molecular cloning

2.2.1 Plasmid mini-prep

The following plasmid mini-prep procedure was used for all cloning procedures. One colony was scraped from the selective plate and inoculated in 5 mL of LB with corresponding antibiotics (100 μg mL^{-1} ampicillin/spectinomycin, 25 μg mL^{-1} kanamycin). Cells were cultured overnight at 37°C, followed by centrifugation to pellet cells. Plasmids were purified using the ThermoFisher GeneJet Plasmid Miniprep kit according to manufacturer protocols. Plasmid concentration was calculated automatically by the NanoDrop 2000 Spectrophotometer (ThermoFisher Scientific) using A260 readings.

2.2.2 Quick-change mutagenesis

Quick change mutagenesis was used in the creation of pSZ1 (His-SUMO-SBA1c; Table 2.2) and pSZ5 (SBA3 coding sequence in pCR8; Table 2.1). Both procedures used the two-step quick change mutagenesis protocol from Wang and Malcolm (1999). Primers for pSZ1 were designed to include an extra codon (ACC/GGT) to insert a glycine residue between the SUMO and SBA1c coding sequences of pMK159. Primers for pSZ5 were designed to omit the stop codon at the end of the SBA3 coding sequence in pMK176 (Table 2.1). Following the two stage PCR protocol, both plasmids were transformed into DH5α competent cells using the NEB transformation protocol. pSZ1-transformed cells were plated on LB agar/ampicillin (100 μg ml^{-1}) plates, and pSZ5-transformed cells were plated on LB agar/spectinomycin (100 μg ml^{-1}) plates.

2.2.3 TOPO cloning of complete SBA coding sequences

The SBA4 coding sequence was amplified using SBA4-specific primers (Table 2.1) on whole *A. thaliana* cDNA template (prepared from 10-day-old whole seedlings, gift of Dr. Minsoo

Kim). Polymerase chain reactions using Phusion polymerase were performed using NEB Phusion manufacturer protocols, which consisted of 98°C for 30 sec, followed by 35 cycles of 98°C for 10 sec, 68°C for 30 sec, and 72°C for 1 min. Cycling conditions were followed by one 72°C incubation for 10 min. PCR products were purified using Qiagen QiaSpin PCR Purification kits. Following purification, 1 µL of Taq polymerase and 0.1 mM dNTPs were added to PCR products in a final volume of 50 µL. The reaction was incubated at 72°C for 1 hr, and then cloned into pCR8 (ThermoFisher Scientific, catalog number 250020) using the ThermoFisher GW TOPOMan procedure. The TOPO reaction was used to transform DH5α cells using the NEB transformation protocol, followed by incubation and plasmid miniprep. Restriction enzyme digestion was used to verify insertion and orientation of the insert using DraI and PvuI (37°C overnight). Purified plasmids were sequenced to confirm proper cloning. Plasmids containing the SBA1, SBA2, and SBA3 coding sequences in pCR8 were previously prepared by Dr. Minsoo Kim (Table 2.1).

2.2.4 Generation of C-terminal and complete SBA expression vectors via Gibson assembly cloning

Gibson Assembly was used for cloning of pSZ3 and pSZ4 (Table 2.2), which first required plasmid mini-prep of pMK123, pSZ2, and pET23b-His-SUMO (Tables 2.1 and 2.2). Purified plasmids were amplified using Gibson-specific primers and Phusion polymerase according to the NEB Phusion manufacturer's protocol. A three-fold excess of entry vector was added to the pET23b-His-SUMO expression vector in a final volume of 5 µL. An equal volume of Gibson Assembly master mix was added (3.75% PEG-8000, 75 mM Tris-HCl pH 8.0, 7.5 mM $MgCl_2$, 0.15 mM each dATP, dCTP, dGTP, dTTP, 7.5 mM DTT, 0.75 mM NAD, 0.004 U/µL T5 Exonuclease, 0.0025 U μL^{-1} Phusion polymerase, 4 U μL^{-1} DNA ligase). Vectors and master mix

were incubated at 55°C for 4 hr, followed by transformation and plasmid miniprep. Proper insertion of the coding sequences was confirmed with restriction enzyme digestion.

To produce expression vectors containing the complete SBA coding sequences, the same procedure as described for pSZ3 and pSZ4 was used. pMK122, pMK123, pSZ5, and pSZ2 (Table 2.1; representing plasmids with the SBA1, 2, 3, and 4 coding sequences, respectively) were mini-prepped for Gibson assembly cloning. Additionally, the pET23b-His-SUMO destination vector (Table 2.2) was mini-prepped. The same PCR protocol was applied, followed by transformation, mini-prep, and restriction enzyme digestion.

2.2.5 Plasmid assembly with LR Clonase

LR Cloning (ThermoFisher Scientific), also known as Gateway cloning (Zhang et al., 2006; Nakagawa et al., 2008), was used for the assembly of vectors for bi-molecular fluorescence complementation (BiFC). pCR8-based entry vectors were diluted to 150 ng μL^{-1}. Destination clones pSPYCE and pSPYNE were diluted to the same concentration (Walter et al., 2004; plasmids were a gift of Dr. Klaus Harter, Tubingen University). A total of 1 µL of each entry and destination vector was mixed with 8 µL of TE buffer (10 mM Tris-HCl, 1 mM EDTA pH 8.0) followed by addition of 2 µL of LR Clonase II enzyme. The reaction was incubated overnight at room temperature (22° C). Following incubation, 2 µL of Proteinase K was added the reaction mixture, followed by incubation at 37°C for 10 min. Following Proteinase K reaction quenching, 1 µL of the reaction was used to transform 50 µL of DH5a *E. coli* cells using the New England Biolabs transformation protocol. Cells were plated on kanamycin (25 µg mL^{-1}) and gentamycin (50 µg mL^{-1}) LB-agar plates and incubated for 12-16 hr. Viable colonies were inoculated into 5 mL overnight cultures containing the same antibiotic concentrations as listed above and

miniprepped the following morning using the ThermoFisher GeneJet Plasmid Purification kit. Plasmids can be found in Table 2.3.

2.3. Large scale protein purification

2.3.1. Bacterial growth and protein expression

BL21 (λDE3) pLysS cells were transformed with either pSZ1 or pMK175 (Table 2.2) using the New England Biolabs transformation protocol. After growth on ampicillin plates, one colony from each plate was used to inoculate 25 mL of Luria-Bertani (LB) media containing ampicillin and chloramphenicol (100 μg/mL, 25 μg/mL) and left to shake at 200 RPM for 12-16 hours at 37°C. Based on previous assays, only freshly transformed colonies (< days old) were used for inoculation due to poor induction profiles from older transformants. Following incubation, the 25 mL culture was used to inoculate 1,000 mL of LB media containing ampicillin (100 μg/mL) and the culture was incubated at 37°C for 2 hours, followed by incubation at 16°C. Optical density at 595 nm was measured every 15 min until the culture reached an OD of 0.5-0.7. Protein expression was then induced with 0.1 mM isopropyl β-d-1-thiogalactopyranoside (IPTG) and the cultures incubated at 16°C with 200 RPM shaking overnight. Cells were grown until the OD600 of tenfold diluted culture measured approximately 0.25 (2.5 overall). Following incubation, the culture was centrifuged to pellet cells at 7,000 RPM for 15 min, followed by decanting the media and freezing the pellet at -20°C.

2.3.2. Cell lysis and supernatant preparation

Cell pellets were thawed on ice for 15-20 minutes, followed by resuspension in lysis buffer (25 mM Tris/HEPES, 300 mM NaCl, 10 mM imidazole, 0.2% IGEPAL Ca-630, 1 mM phenylmethylsulfonyl fluoride, added fresh) at a ratio of 30 mL buffer for every 1 liter of cell

culture pellet. HEPES-based buffers were used for purifying SBA1c and SBA3c for ATPase and crosslinking assays, while Tris-based buffers were used for other purifications. Cells were lysed on ice for 30 min using manual agitation, followed by sonication at 40% amplitude on a 3 sec on/6 sec off cycle for 10 cycles. Prior to microfluidization, the instrument was first packed with ice to keep the temperature of the cell lysate low to minimize proteolysis. The inner tubing was sanitized by running 2 tube volumes (~15 mL) of 70% isopropanol through the system, followed by a wash with an equivalent volume of water. The tubing was then equilibrated by running the same volume of lysis buffer through the system. The cell lysate sample was then applied to the microfluidizer and collected. This process was repeated an additional four times to ensure homogeneity of lysis. To minimize loss of cell lysate, an additional 15 mL of lysis buffer was applied through the apparatus and collected in addition to the rest of the microfluidized lysate. At this point, approximately 50 mL of cell lysate remained for purification. The lysate was centrifuged at 18,000 x g for 30 min, to separate the cleared lysate from the cell debris.

2.3.3. Gravity flow protein purification

Gravity flow was used for purification of SBA proteins using HEPES-based buffers. After centrifugation of the cell culture supernatant, 2 mL of His-Pur Ni-NTA resin was added to a 15 mL polypropylene column and equilibrated with 10 mL of lysis buffer. The resin was then transferred to a 50 mL falcon tube and incubated with the supernatant for 1 hr at 4°C on a rotating agitator. The supernatant and resin were added back to the polypropylene column, and flow through was collected. Resin was washed with 10 mL of wash buffer I (25 mM HEPES, 300 mM NaCl, 20 mM imidazole, 0.2% IGEPAL Ca-630), followed by 10 mL of wash buffer II (25 mM HEPES, 300 mM NaCl, 30 mM imidazole, 0.2% IGEPAL Ca-630), and 10 mL of wash buffer III (25 mM HEPES, 300 mM NaCl, 50 mM imidazole, 0.2% IGEPAL Ca-630). Following wash

steps, protein was eluted with 10 mL of elution buffer (25 mM HEPES, 300 mM NaCl, 250 mM imidazole, 0.2% IGEPAL Ca-630), and 1.0 mL fractions were collected.

2.3.4. Protein purification by fast protein liquid chromatography (FPLC)

An FPLC method was used for purification of SBA proteins in Tris-based buffers. For all steps, the AKTA Prime FPLC (GE Healthcare) was used on manual settings with 1 mL/min flow rates in a 4°C cold cabinet. Following centrifugation of cell culture supernatant, the FPLC was placed on the System Wash Method to rinse tubing with sterile MilliQ water. The His-Pur Ni-NTA 1 mL cartridge (ThermoFisher Scientific) was then attached to the FPLC and washed with 10 mL of lysis buffer. The centrifuged supernatant was applied to the column through input tubing, followed by the same washing and elution steps as described in gravity flow purification. For the wash fractions, the sample collector was programmed to collect the whole fraction in one container. For the elution fractions, the sample collector was set to collect 1 mL of eluate per tube, with each 1 mL being dispensed into a separate tube.

2.3.5. Sodium dodecyl-sulfate polyacrylamide gel electrophoresis

Following purification, 10 µL of each fraction were diluted 1:10 (total, supernatant, and pellet), 1:5 (wash buffer), and 1:2 (elutions) in 2X SDS sample buffer (50 mM Tris HCl, 2% SDS, 0.1% bromophenol blue, 10% glycerol, 2 mM DTT (added fresh)). The samples were boiled at 98°C for 5 min and briefly centrifuged. A total of 10 uL of each sample was loaded on a 5-16% gradient SDS-acrylamide gel, which was run for 1.5 hr at 30 mA in 1X running buffer (25 mM Tris, 192 mM glycine, 0.1% SDS). The gel stained using a homemade fast staining system (0.1% Coomassie Brilliant Blue G-250, 0.29M phosphoric acid, 16% ammonium sulfate), which first involved washing the gel. Upon removal from the running buffer, the gel was washed in

distilled water, then submerged in fresh distilled water, and microwaved for 1 min. The gel was then incubated on a rotating platform for 3 min, the water decanted, and the wash repeated two more times. Following the washes, the gel was covered in the fast staining solution and left on the rotating platform for 1 h. Finally, the gel was briefly rinsed in distilled water and imaged using a camera.

2.3.6. Protein dialysis and His-SUMO cleavage

The purest elution fractions (~5-10 mL) were pooled and transferred to dialysis tubing (SpectraPor, MWCO 30,000 Da) with 50 µL of Ulp1 SUMO protease (pHis6_Ulp1 was a gift from Dr. Indu Santhanagoplan, encodes 6X His tagged Ulp1. Purified by Dr. Patrick Treffon). The tubing was incubated in 2 L of dialysis buffer (25 mM Tris/HEPES, 300 mM NaCl, 0.2% IGEPAL Ca-630, 2 mM dithiothrietrol) overnight at 4°C. Following dialysis, the same Ni-NTA resin was equilibrated with 10 mL of dialysis buffer, followed by application of the dialyzed fraction. The column was washed with 10 mL of dialysis buffer, followed by 10 mL of wash buffer I and 10 mL of elution buffer.

Results were analyzed via SDS-PAGE, and the fractions containing pure protein without His-SUMO tags were set aside for concentration. These fractions were pooled into a 15 mL Amicon centrifugal concentrator (EMD Millipore, UFC903024) and spun at 7,000 x g for 5 min at a time until approximately 2 mL remained within the filter apparatus. The protein solution was then mixed by pipetting and aliquoted in 200 µL fractions into a 1.5 mL tube. Tubes were flash frozen and stored at -80°C until further use. Protein concentration was determined by Pierce Bicinchoninic Acid (BCA) assay (ThermoFisher Scientific) using manufacturer protocols.

2.4. Protein crosslinking assays

2.4.1. Formaldehyde crosslinking

A 16% fresh formaldehyde stock was diluted to 8% for crosslinking experiments. The working reagent was stored for up to 1 week based on manufacturer protocols. For each experiment, 5 µM SBA1c or SBA3c was added to a 1.5 mL tube on ice, followed by the appropriate volume of dialysis buffer. ATP, $MgCl_2$, and DTT were added to a final concentration of 1 mM, and formaldehyde was added to the desired final concentration (1%, 2%, or 4%) such that the final volume was 100 µL. Other trials were conducted with the omission of either ATP, $MgCl_2$, or both, to determine their effect on crosslinking. Following mixing of all reagents, 15 µL was removed and added to a separate tube with an equal volume of 2X SDS sample buffer to quench the reaction. The first tube represented the T0 sample. The rest of the samples were placed in a thermomixer at 22°C with 300 RPM shaking. At time points of 10, 20, and 30 min, a 15 µL aliquot was removed and added to an equal volume of 2X sample buffer. The 30 µL samples were then loaded on a 5-16% SDS acrylamide gel along with 10 µg of purified SBA1c or SBA3c for comparison, and run at 40 mA for 90 min. The gel was washed and stained with Coomassie Brilliant Blue G-250.

A separate experiment was conducted using the above protocol, but combining SBA1c and SBA3c. Molar ratios of the two proteins were varied (2:1, 1:2, 1:1) and the amount of dialysis buffer was adjusted for a final volume of 100 µL. For the SBA1c SBA3c combined experiments, SDS acrylamide gels were not stained. Gels were transferred to nitrocellulose membranes using the semi-dry blotting method and washed with Tris-buffered saline with 0.1% Tween 20 (TBS-T, 20 mM Tris-HCl, 150 mM NaCl) for 1 hr. The blot was blocked with a 5% milk powder in TBS-T for 1 hr, followed by addition of rabbit anti-SBA1c antibody (Agrisera) at a dilution of 1:4000

overnight at 4°C. The membrane was washed for 10 min with TBS-T, and this process was repeated twice. Following washing, the membrane was incubated with goat anti-rabbit horseradish peroxidase (HRP)-conjugated secondary antibody (GE Healthcare) at a dilution of 1:5000 for 90 min. The washing steps were repeated, and the membrane was incubated with 2 mL of ECL solution (95.5 mM Tris-HCl pH 8.5, 189 µM p-coumaric acid, 1.19 mM luminol, 0.008973% hydrogen peroxide [added fresh from 3% stock]) . The G-BOX imaging unit was used to expose the membrane and capture chemiluminescent signal.

2.4.2. Dithiobis (succinimidyl propionate) (DSP) crosslinking

Dry DSP powder (ThermoFisher Scientific) was equilibrated at room temperature and disolved in DMSO to a final concentration of 5 mM. As with formaldehyde crosslinking, SBA1c or SBA3c protein was diluted to a final reaction concentration of 5 µM and added to 1 mM each of ATP, $MgCl_2$, and DTT. Certain trials of DSP crosslinking omitted either ATP or $MgCl_2$, or both. DSP was added to a final concentration of either 0.5 mM, 1 mM, or 2 mM. An additional 15 µL was removed at T=30 min and 10 mM DTT added to assess crosslinking reversibility. The rest of the DSP crosslinking procedure and blotting was conducted identically to the formaldehyde procedure.

2.5. ATPase activity assays

ATPase activity assays were performed with the Malachite Green Phosphate Capture reagent (Sigma-Aldrich) using a modified version of the manufacturer's protocol in a 96-well clear bottom plate. The proteins SBA1c and SBA3c were plated at concentrations of 1 µM and 2 µM each in individual 80 µL reactions containing 0.1 mM ATP, as well as 0.1 mM $MgCl_2$ in HEPES dialysis buffer (25 mM HEPES, 300 mM NaCl, 0.2% Igepal CA-630). SBA1c and

SBA3c were separately diluted to 1 µM or 2 µM per well in buffer. This procedure was completed in quadruplicate for a total of 16 experimental wells . Additionally, separate wells contained 0.5 µM ClpX protein from *Caulobacter crescentus* (provided by Samar Mahmoud, Chien Lab UMass) as a positive control, also in quadruplicate. The ClpX protein reactions contained the same reagents as the SBA1c and SBA3c replicates. The Malachite Green reagent and phosphate standard were prepared according to the manufacturer's protocol. After plating serial dilutions of the phosphate standard, 20 µL of the Malachite Green reagent was added to each well, including the water alone and water plus ATP blanks. The plate was then placed in a plate reader (Synergy2, Biotek Instruments, Inc.) and set to read every 5 min at 620 nm. The water plus ATP absorbance values were subtracted from the experimental absorbance values for each time point, and a standard curve of free phosphate concentration was constructed using the absorbance values for the phosphate standard. The equation of the standard curve was used to calculate the free phosphate concentration in wells containing either SBA1c, SBA3c, or ClpX. An average value was used from the sum of each protein replicate, and a value was calculated for picomoles of phosphate per µM of protein. These results were plotted in GraphPadPrizm, which also calculated standard deviation based on the values of each well.

2.6. Plant screening and growth

In previous experiments, Dr. Minsoo Kim transformed *sba3-1* mutant plants with the pMK161 plasmid that encodes SBA1 antisense RNA, along with BASTA herbicide resistance. The T1 seeds from these T0 transformed plants were provided by Dr. Minsoo Kim. To screen for T1 transformants, approximately 1,000 seeds from each of the 19 T0 plants were placed in a 1.5 mL tube and sterilized in 70% ethanol with 0.05% Triton X-100. The seeds were vortexed every 2 min for approximately 15 sec at a time over 10 min. The ethanol was removed from each tube,

and 1 mL of 100% ethanol was added in a sterile biosafety cabinet. The seeds were left to sterilize for 10 min, and then removed from the tube and placed on sterile filter paper. Once the seeds were dry, they were plated on Murishage-Skoog/agar plates (0.5X MS, 0.05% MES hydrate, 0.5% sucrose, 0.8% agar). Plated seeds were transferred to a 4°C cold cabinet for 2 days, followed by incubation in the dark at 22 °C for 2 days. After the 4 day incubation, plates were placed horizontally in a growth chamber (light intensity 275 µmol m^{-2} s^{-1}) and allowed to grow for 7 days on a 16h light/8 hr dark schedule. Plates were removed and transformants were identified. For the T1 screen, all plants displaying BASTA resistance were removed and transplanted to soil. This process was then repeated for the T2 screen using approximately 50 seeds per line. However, only T2 lines segregating 3:1 for BASTA resistance were transplanted in order to obtain plants that were stably transformed with one insertion event. The T3 screening also tested 50 seeds per line using the above protocol. T3 seeds were scored for 100% transformation, indicating homozygosity for the transformed genes.

In addition to pMK161 transformed plants, Dr. Kim also provided plant lines that were transformed with pER-RB (Nelson et al., 2007). This plasmid contains the fluorophore mCherry conjugated to AtWAKII (wall-associated kinase II, AGI: AT1G21270) on the N-terminus of the fluorophore, and the ER retention sequence HDEL conjugated to its C-terminus (Nelson et al., 2007). pER-RB vector also contains the gene coding for BASTA resistance. Transformation using *A. tumefaciens* was performed on plants from Col-0, Mito-GFP, *shot1-2*, and *shot1-2* Mito-GFP lines. The same screening and growth protocol was used for the pER-RB transformants.

2.7. Heat stress assay

The protocol from Kim et al. (2017) was used for the hypocotyl elongation heat stress assay. Homozygous seeds from the following genotypes were used: *sba1, sba2, sba3, sba4, sba2*

sba4, *hot1-4*, and Col-0. Seeds were sterilized using the above protocol and plated according to directions from Kim et al. (2017). Three separate heat stress treatments were used, all with an identical protocol except for duration of 45°C heat stress. Heat stress times of 2.5, 3, and 3.5 hrs were used to determine heat stress vulnerability of *sba* mutants. Hypocotyl elongation prior to heat stress was measured by marking the plastic plate where the hypocotyl ended. Following heat stress and recovery, hypocotyl length was once again marked. ImageJ was used to measure growth prior to and after heat stress with the 1cm plate intervals as a length reference. The data were evaluated using Excel to calculate plant growth as a percentage of growth before heat stress, and standard error was calculated for each genotype using Excel macro functions.

2.8. Size exclusion chromatography (SEC)

All SEC experiments were conducted on a Varian ProStar 325 High Pressure Liquid Chromatography instrument with a Tosoh TSKGel G5000PWXL size exclusion column. SBA1c and SBA3c were adjusted to 10 µM, then diluted two-fold in HPLC running buffer (25 mM Tris, 300 mM NaCl, 0.2% Igepal CA-630). For each run, HPLC running conditions were set to a maximum 2 MPa pressure and 1 mL min^{-1} flow rate. The UV detector was set to a 280 nm/210 nm dual wavelength at a bunch rate of 4 (5GHz) with data acquisition set to 1 GHz. A total of 15 µL of protein solution was injected into the 5 µL loop manually after 30 min of flushing the column with running buffer. In addition to SBA1c and SBA3c samples, the Bio-Rad Gel Filtration protein standard was also analyzed using the same acquisition settings, with 15 µL of protein solution applied to the column. This protein standard was run in a modified running buffer without Igepal CA-630 due to signal interference (25 mM Tris, 300 mM NaCl).

Separate runs were conducted with ATP added to either SBA1c or SBA3c, but not to the running buffer. Following concentration adjustment of protein, ATP solution was added to a final

concentration of 1 mM with protein at 10 µM. Data acquisition, UV detector, and run settings were identical to other SEC trials.

2.9. Bimolecular fluorescence complementation

2.9.1. Agrobacterium transformation

Agrobacterium tumefaciens strain GV3101 was used for transient expression of BiFC constructs in *Nicotiana benthamiana* (tobacco) leaves from plants grown on soil. *A. tumefaciens* cells were transformed by first adding 1 µL of plasmid per 50 µL of cells and incubated on ice for 5 min. Cells were transferred to an electroporation cuvette and shocked at 1,250 V for 6-10 ms using an electroporator apparatus. Following shock, 1 mL of room temperature LB medium was added to the cuvette, and then transferred to a 1.5 mL tube. The cells were incubated at 28° C for two hr, and then briefly centrifuged to pellet cells. A total of 900 uL of cell-free media were removed and the cells were resuspended in the remaining medium. Following resuspension, 25 µL of cells were plated on LB/gentamycin (50 µg mL^{-1})/kanamycin (25 µg mL^{-1}) plates and incubated for 2 days at 28° C.

2.9.2. Preparation of cultures for tobacco leaf infiltration

The following procedure was adapted by Dr. Minsoo Kim from a previously established protocol (Walter et al., 2004). Two *A. tumefaciens* colonies were inoculated for each construct into separate tubes of 5 mL of LB with kanamycin and gentamycin at concentrations stated in the previous section. These were incubated at 28° C for 29 hr until OD600 had reached approximately 2.5. Cells were then pelleted by centrifugation (5000 *g*, 22° C, 15 min) and supernatant was discarded. The remaining cells were resuspended in 2 mL buffer (10 mM $MgCl_2$, 10 mM MES-KOH pH 5.7). A 100 µL aliquot of each strain containing the different constructs

was diluted in 900 µL of resuspension buffer and OD600 was measured. The total OD600 of each culture was calculated, and each culture was diluted to an OD600 of 0.5. Following this step, each pair of BiFC constructs was mixed in a separate tube so that the sum of the two OD600 values was 1.0. At this step, a fresh 100 mM stock of acetosyringone was prepared in DMSO. The stock solution was then added to the *A. tumefaciens* mixture to a final concentration of 200 µM acetosyringone. The cells were left to incubate at room temperature overnight.

2.9.3. Infiltration and transient expression

Wild-type *N. bethamiana* plants were grown for 3-5 weeks prior (until leaves were large enough for injection) to infiltration and transient expression. For each pair of BiFC constructs, one tobacco plant was used. The overnight incubation culture was loaded in a 5 mL syringe, which was then pressed against a leaf on the tobacco plants. Leaves higher on the main shaft of the plant were used for infiltration. The syringe was slowly depressed while counter pressure on the other side of the leaf was applied with a finger. A total of ~0.5 mL of the *Agrobacterium* mixture was applied until the leaf was saturated, and enough was reserved for application to a second leaf in the same manner. Plants were then grown for an additional 5 days until light microscopy.

2.9.4. Fluorescence light microscopy

Once leaves had grown for 5 days following infiltration, they were removed from the rest of the plant and sectioned into approximately 5 mm by 5 mm squares. These sections were placed on a glass slide and sealed with approximately 100 µL of MS liquid media and a coverslip. The microscope used for this experiment was a Nikon A1RMP Multiphoton Scanning Confocal Light microscope at 40X zoom magnification. The FITC channel (462 nm excitation, 525 nm emission

maximum) was used for excitation of the YFP-labelled constructs, and images were captured using Nikon NIS Elements software.

2.10. Imaging of fluorescently labelled organelles in *Arabidopsis thaliana*

2.10.1. Plant growth

Plants stably transformed with pER-RB (as described in section 2.5) were screened until T3 homozygotes were obtained. The full list of plant lines is available in the appendix. Two lines per transformation were chosen in addition to two independent lines of wild-type Col-0. These plants were used as a negative control, as they should exhibit no fluorescent emission in either the FITC or TRITC channels. A total of 15-20 seeds were sterilized per line according to section VI and plated according to the protocol in section VII. These seedlings were grown vertically for 10 days in 16 hr light/8 hr dark conditions.

2.10.2 Fluorescence microscopy

Seedlings were removed from MS agar medium and placed on a glass slide, then affixed to a coverslip with ~50 uL of liquid MS media. A Nikon A1SP Spectral Scanning microscope with NIS Elements was used for scanning fluorescence microscopy. The FITC channel (462 nm excitation, 525 nm emission maximum) was used for Mito-GFP excitation in addition to the TRITC channel (532 nm excitation, 576 nm emission maximum) for the mCherry-WakII (red fluorophore) excitation. Meristematic and differentiation zones were used for image capture in areas where bright fluorescence could be observed. Images were captured at 40X, 60X, and 100X optical zoom, and processed using NIS Elements and NIS Elements Viewer.

CHAPTER 3: INVESTIGATING THE OLIGOMERIC STATE OF THE SBA PROTEINS

3.1. Introduction

As described in Chapter 1, ATAD3a and its homologs belong to the AAA family of proteins. The oligomeric state of this family has been well-characterized and tends to follow discrete patterns. Most AAA proteins form either single- or double-ringed hexamers with ATPase regions localized in a stacked format (Vale, 2000; Lupas and Martin, 2002). The formation of most AAA oligomers is dependent upon the capacity of the monomer to bind nucleotides via the Walker A motif (Vale, 2000). Loss of ATP binding at this site has been shown to abrogate higher-order oligomerization in many AAA proteins.

In the case ATAD3a/SBA proteins, oligomerization state has never been studied in plants. However, previous data from human, mouse, and fly models support the importance of ATAD3a oligomerization. Firstly, it was shown that loss of ATP binding via Walker A mutation in ATAD3a did indeed cause loss of oligomerization. Effects of this change *in vivo* were observed to be a distinct increase in mitochondrial fission and loss of membranous contact sites with the ER (Gilquin et al., 2010). One interpretation of these data is that loss of ATAD3a oligomers directly caused loss of contact with the ER, which in turn activated ER stress response machinery (Gadir et al., 2011). In a separate study using human neuronal cells, loss of ATAD3a oligomerization was shown to recruit the DRP1 GTPase mitochondrial fission machinery (Zhao et al., 2019). Previous characterization of the DRP1 pathway showed that it was responsible for activating mitophagy during stress conditions via mitochondrial fission, suggesting that the loss of ATAD3a oligomers ultimately causes mitochondrial degradation (Zorov et al., 2019). Based on these data, ATAD3a oligomeric status is directly and intimately tied to overall mitochondrial health and maintenance.

Although ATAD3a oligomerization has been moderately characterized, there is nothing known about the oligomeric state of the *A. thaliana* SBA proteins. Their interactions are further complicated by the fact that there are four *A. thaliana* SBA homologs, suggesting that they could form hetero-oligomers. Additionally, defining SBA oligomerization in plants could lead to further understanding of mitochondrial dynamics *in vivo*, and perhaps provide context as to why SBA proteins were identified in co-IP experiments with SHOT1. It was therefore my aim to first identify the domains necessary for SBA oligomerization and compare these to known results from ATAD3a experiments. It was also my goal to assess which of these domains are related to the activity of the protein so as to understand the connection between oligomeric state and ATPase activity of SBA proteins. My final goal was to use fluorescent reporter assays to test the *in vivo* interaction between the four SBA proteins. Understanding the relationships of the proteins remains an unknown factor in their evolutionary history and identifying their roles *in vivo*.

3.2. Structure and phylogenetic relationship of the SBA proteins

A total of four SBA proteins were identified in *A. thaliana*; SBA1 (AGI number: At3g03060), SBA2 (At5g16930), SBA3 (At2g18330), and SBA4 (At4g36580). These genes are present on separate chromosomes. Protein sequence alignments showed that they are separated into two clades, one composed of SBAs 1 & 2, and the other of SBAs 3 & 4 (Figure 3.1, Figure S1). SBAs in the same clade have ~85% sequence identity, while between clades the proteins have ~60% identity (Figure S.1).

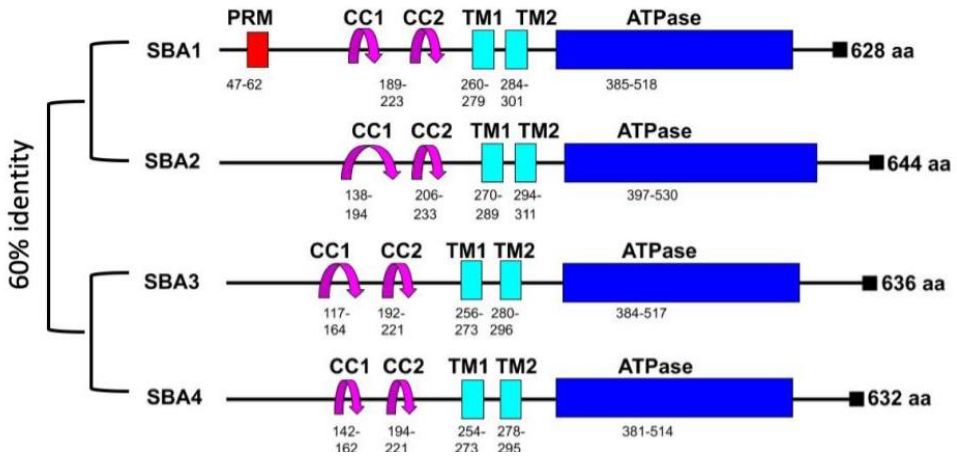

Figure 3.1: Linear representations of SBA proteins 1 to 4. Sequences were uploaded from UniProt and aligned using Clustal Omega (https://www.ebi.ac.uk/Tools/msa/clustalo/). Coiled coil domains (CC) were predicted using UniProt entries and ExPasy COILS (https://embnet.vital-it.ch/software/COILS_form.html), and transmembrane domains (TMS) were predicted using Expasy TMPRED (https://embnet.vital-it.ch/software/TMPRED_form.html) and WHAT (http://biotools.tcdb.org/barwhat.html).

Many features of human hsATAD3a (UniProtKB Q9NVI7-2, 586 amino acids) are seen in the four SBA homologues. All four proteins contain two coiled-coil domains, shown to promote N-terminal oligomerization of ATAD3a in experiments with homologues from *Drosophila* (Gilquin et al., 2010). To predict transmembrane domains (TM) in the *A. thaliana* proteins, HMMTOP (Tusnady and Simon, 1998, 2001) and TMpred (Hoffman and Stoffel, 1993; Ikeda et al., 2003) programs were used. TM domains that showed a consensus prediction between the two programs are included in Figure 3.1. Similar to the hsATAD3a shown in Figure 1.2, there are two TM domains located upstream of the ATPase domain. Additionally, the two TM domains in all four SBA proteins follow the same pattern as the TM domains in humans, wherein the first domain has a large helical moment (3.42 to 4.96), while the second does not (0.88 to 2.01). When searching for proline-enriched areas, only the SBA1 sequence was annotated with a PRM in the

N-terminus, while the three other proteins did not. The sequence alignment of the SBA proteins did show that the predicted PRM domain of SBA1 was highly similar to the corresponding regions in the remaining 3 SBA proteins, suggesting that they also contain the PRM domain that was not annotated by the sequence analysis tools used by UniProt (Figure S3). Finally, all four proteins contain the conserved ATPase domain, with characteristic Walker A and Walker B motifs.

To investigate the origins of the four distinct SBA proteins, a phylogenetic analysis using Phylogenes (Phoenix Bioinformatics Corporation, PANTHER at University of Southern California) was completed using SBA1 as the input (Figure 3.2). The resulting tree was then pruned to give one example organism per classification, in order to highlight the evolutionary origins of the four SBA proteins. The raw output using Phylogenes analyzed the phylogeny of 648 gene products, which included alternative splice variants. These genes, along with their respective organism and protein information can be found in Table S1. This analysis predicts that two duplications occurred from one ancestral gene to yield the four SBA proteins found in *A. thaliana*. Both of these duplications can be placed at some point after the development of flowering plants, as mosses and algae only have a single clade of SBA proteins. Organisms outside of plant lineages may have more than 1 SBA/ATAD3 protein, but these are only found in one clade as compared to the two higher plant clades. *Amborella trichopoda*, the sister group to all flowering plants, has an SBA homolog in both clades, indicating that the first SBA duplication predated the monocot-eudicot split (~120 MYA; Soltis and Soltis, 2013). The second duplication was more difficult to pin to a specific date, since the most closely related homologs to SBAs 1 to 4 tended to be in species that had recently been domesticated, such as cabbage. However, based on the presence of SBA1 to 4 homologs in both the *Malvales* and *Brassicales* orders, it is likely that the second SBA gene duplication event occurred at some point prior to the split of these two

orders (~103 MYA; Cardinal-McTeague et al., 2016; Sun et al., 2020). Given these data, I believe that the first duplication event created the two separate clades (SBA1/2 and SBA3/4), whereas the second duplication event created the intraclade homologues. Still, these observations do not explain if the four proteins serve unique or redundant functions.

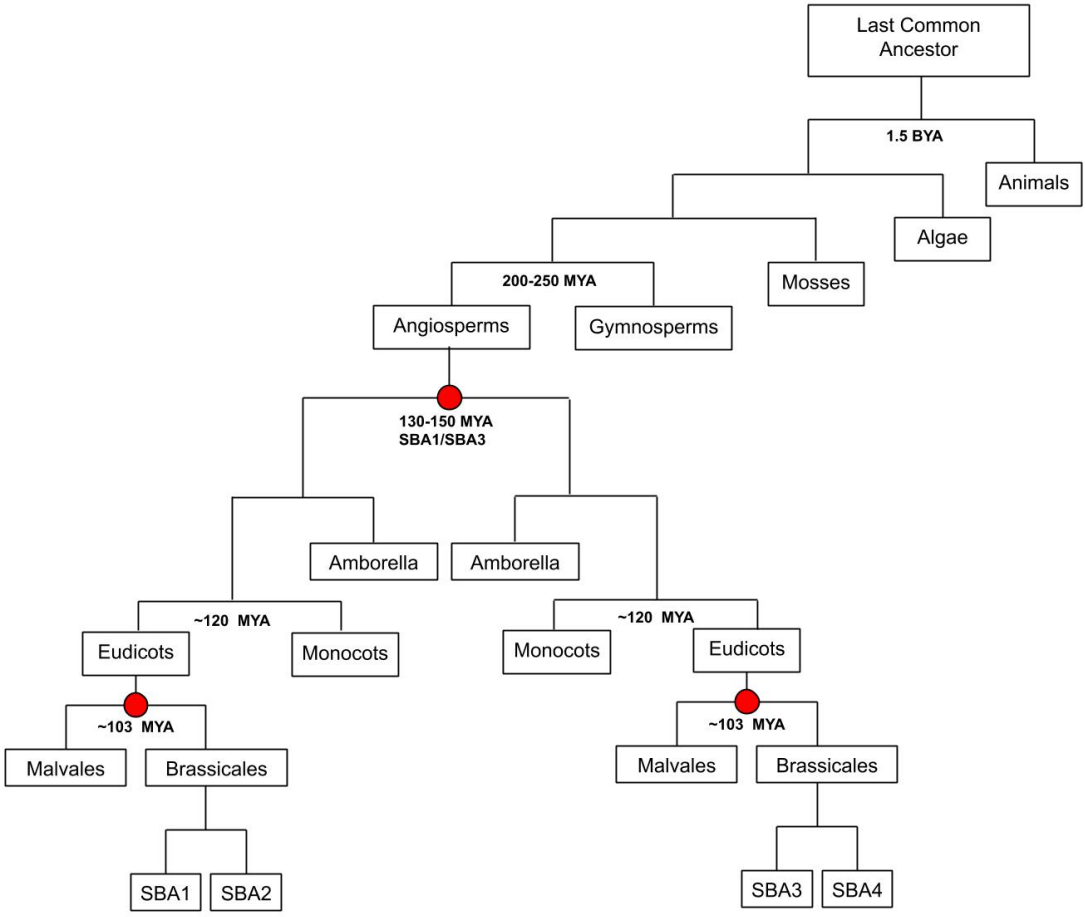

Figure 3.2: Phylogenetic analysis of SBA proteins and origin of the two clades with intraclade duplications. A phylogenetic analysis was performed on the sequence of SBA1 using PhyloTrees (http://www.phylogenes.org/tree/PTHR23075). The output was pruned to one gene entry per representative organism or plant group and illustrated as above. Red nodes signify the duplication event, the first of which occurred 130-150 MYA to produce the SBA1/2 and SBA3/4 clades. The second duplication, which produced the four distinct SBA proteins, occurred prior to the differentiation of the order Brassicales approximately 103 MYA. Other key dates indicating divergence of major groups are demarcated at their respective junctions. BYA: billion years ago; MYA: million years ago.

3.3. Genetic analysis of SBA mutants

T-DNA insertion mutants were obtained for all four *A. thaliana* SBA proteins, and the single mutants were all found to be viable through work completed by Dr. Minsoo Kim (Table 3.1). This indicates that the SBA proteins may perform redundant functions. To test if these proteins might contribute to stress tolerance, I performed a hypocotyl elongation assay of heat tolerance on the single mutants. The data (Figure S2) demonstrate that heat stress tolerance of single *sba* mutants was the same as seen in wild-type plants. To investigate further any redundancy in SBA gene function, Dr. Minsoo Kim made all pairwise combinations of the mutant genes by crossing, in order to observe viability of double mutant plants. The two intraclade double mutants were embryonic lethal (*sba1sba2* and *sba3sba4*), suggesting that at least one SBA protein per clade is necessary for survival. Additionally, all interclade double mutants were lethal except the *sba1sba4* and *sba2sba4* double mutants. I performed a hypocotyl elongation assay (Figure S2) on the *sba2sba4* double mutant and found it showed no significant loss in thermotolerance. The *sba1sba4* double mutant was not available for analysis at the time this assay was performed, but based on heat tolerance of the single mutants, and viability of *sba1sba4*, it would appear likely that this double mutant would also show wild-type heat tolerance. Together, these data suggest that *in vivo* interactions between SBA proteins of the two clades may be necessary for growth and development. Furthermore, it is possible that SBA1 and SBA3 are the more significant proteins for these interactions since double mutants involving either of these proteins are shown to be lethal.

Table 3.1: Lethality of single and double mutant SBA proteins

	Lethal Mutants	Viable Mutants
Single mutants	All single mutants are viable	*sba1*
		sba2
		sba3
		sba4
Double mutants: intraclade	*sba1 sba2*	All intraclade double mutants are lethal
	sba3 sba4	
Double mutants: interclade	*sba1 sba3*	*sba2 sba4*
	sba1 sba4	-
	sba2 sba3	-

3.4. Biochemical analysis of SBA function and interaction

3.4.1. Vectors for expression of SBA full length proteins or the C-terminal ATPase domain

To assess directly the interactions of SBA proteins, multiple cloning projects were completed (Figure 3.3). As mentioned previously, the C-terminal portion of all four SBA proteins contains the catalytic ATPase domain (Figure S1). Though data indicate that the activity of this domain can affect oligomerization and *in vivo* organellar contact sites, the overall importance of this domain to SBA function remains unclear. To this end, it was decided that cloning, expression, and purification of the C-terminal SBA domains could define which domains are necessary for oligomerization and activity. Dr. Minsoo Kim initiated this project by cloning the C-terminal AAA+ domain of SBA1 (amino acids 302-628) and SBA3 (amino acids 297-636) into the pET23b His-SUMO vector for affinity purification. The expressed fragments will be referred

to as SBA1c and SBA3c. Sequencing results showed that the vector containing SBA1c (pMK159, Table 2.2) was missing a glycine residue in the linker region between the SBA1c coding sequence and the His-SUMO tag. The missing residue is encoded in the His-SUMO tag as part of a double glycine motif, so it is not a part of the SBA1c coding sequence. Recognition of a double glycine residue is necessary for Ulp1-mediated cleavage of the His-SUMO tag (Mossessova and Lima, 2000). Consequently, quick change mutagenesis was used to insert an additional GGT codon into the vector. Once this was confirmed by sequencing, the vector was ready to use for expression and purification of SBA1c.

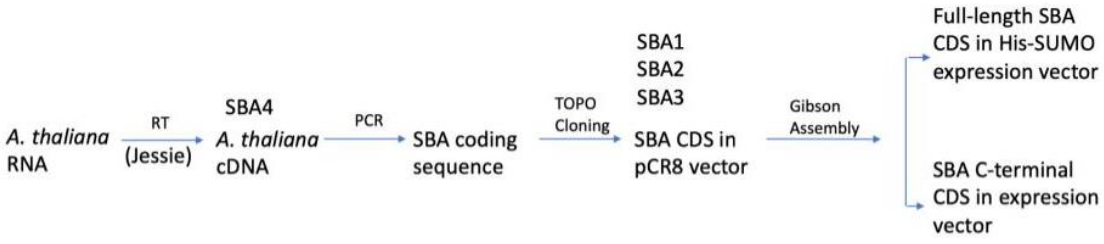

Figure 3.3: Workflow for cloning SBA full-length and C-terminal expression vectors. SBA genes were converted to cDNA by amplification from *A. thaliana* mRNA using reverse transcriptase, and then amplified using gene-specific primers for cloning. These amplicons were cloned into the pCR8 entry vector, and this was previously performed on SBAs 1, 2, and 3. Coding sequences were then cloned into a pET23b-His-SUMO expression vector using Gibson assembly, and this same procedure was performed on the C-terminal fragments of SBA proteins as well.

In addition to vectors produced by Dr. Minsoo Kim, it was also important to clone the C-termini of SBA2c (amino acids 312-644) and SBA4c (amino acids 296-632) for the same purposes as the other two ATPase domains. Though SBA proteins fall into two distinct clades, it remains unclear if the four proteins have distinct characteristics in terms of activity and oligomerization, i.e. perhaps SBA2c requires two CC domains for oligomerization while SBA1c requires none. To be able to test all four SBA proteins, SBA2c and SBA4c were cloned into the

pET23b His-SUMO expression vectors. Primers for these clones (pSZ3 and pSZ4) can be found in Table 2.2.

Using the vectors for expression of the C-terminal ATPase domains does not address the role of the N-terminal TM and CC domains in oligomerization and ATPase activity. To this end, I utilized the same cloning scheme to generate vectors pSZ6 through pSZ9. These plasmids, like pSZ1 (SBA1c), pSZ3 (SBA2c), pMK176 (SBA3c), and pSZ4 (SBA4c) contain the full coding sequence of each SBA protein fused to a His-SUMO tag for affinity purification. Gibson assembly was used to generate these vectors, which have been transformed into *E. coli* expression strains. While the C-terminal domains of SBA proteins are soluble in the mitochondrial matrix, the full length SBA proteins are typically membrane embedded through their TM domains. This may present a significant challenge in purification, since the expressed proteins may have a tendency to become insoluble. Furthermore, sequence analysis through Benchling (https://www.benchling.com) suggests that all four full-length SBA proteins will be unstable in solution. However, it may be possible to express these proteins and purify them in the presence of a lipid bilayer, allowing for extraction in subsequent steps. Purifying full-length SBA proteins may provide a deeper understanding of the oligomeric state of the SBAs.

3.4.2. Purification of SBA1c and SBA3c yields stable protein

SBA1c and SBA3c were chosen to be purified first, as they are representative of the two SBA clades and contained the conserved ATPase domain, which resides in the mitochondrial matrix and therefore could be expected to be soluble. The first step was optimizing buffer composition. Initially, standard affinity purification buffers were employed, using Tris as the buffering agent, sodium chloride to promote solubility, and imidazole as a histidine analog to wash and elute proteins from the nickel affinity column. After multiple trials, it was observed that

SBA1c had a propensity to precipitate following elution. Subsequently, Igepal CA-630, a non-ionic detergent, was included in all buffers at a concentration of 0.2% (v/v) to promote solubility. With the detergent there were fewer instances of SBA1c precipitation, so Igepal was included in all buffers (lysis, wash, elution, and dialysis) in subsequent purification.

Protein induction and expression were accomplished in BL21 *E. coli* cells, producing His-SUMO-tagged SBA1 and SBA3 C-terminal domains. As described in the Methods in Chapter 2, these proteins were purified using nickel affinity chromatography and then dialyzed in the presence of *ULP1* SUMO protease to cleave the His-SUMO tag. Purification of both SBA1c and SBA3c was repeated for a total of two replicates for each protein. After purification, the proteins were resolved by SDS-PAGE to assess purity (Figure 3.4). SBA1c has a calculated mass of 36.4 kDa, and SBA3c has a calculated mass of 38 kDa. Coomassie staining showed that protein from all four purifications migrated as expected. It was later realized that the Tris buffer was not compatible with other planned assays, such as crosslinking and ATPase activity assays. Due to its reactive amine groups, Tris is a natural quencher for chemical crosslinkers such as formaldehyde and DSP (dithiobis(succinimidyl propionate)). As a result, purification of both SBA1c and SBA3c were repeated with a HEPES-buffering system. A key difference in the results of Tris versus HEPES based systems was total protein yield. For SBA1c purifications, total protein yields from one liter of culture using a Tris-based buffer were 1.257 mg and 0.243 mg of total protein for each separate purification. In contrast, the HEPES-based purification yielded a total of 2.9 mg from the same starting culture, nearly doubling yield. Although the cause for this increase in yield was not clear, it was evident through the course of purification that the wash buffers were much more effective at clearing non-target proteins when buffered with HEPES instead of Tris. A similar result for SBA3c was also observed, with yields of 1.001 mg and 0.243 mg in Tris-buffered systems compared to 4.01 mg in HEPES-based buffer. In all cases, the

protein appeared to be >90% pure based on gel images (Figure 3.4C; Figures 3.5 and 3.6), and relatively free of apparent degradation products.

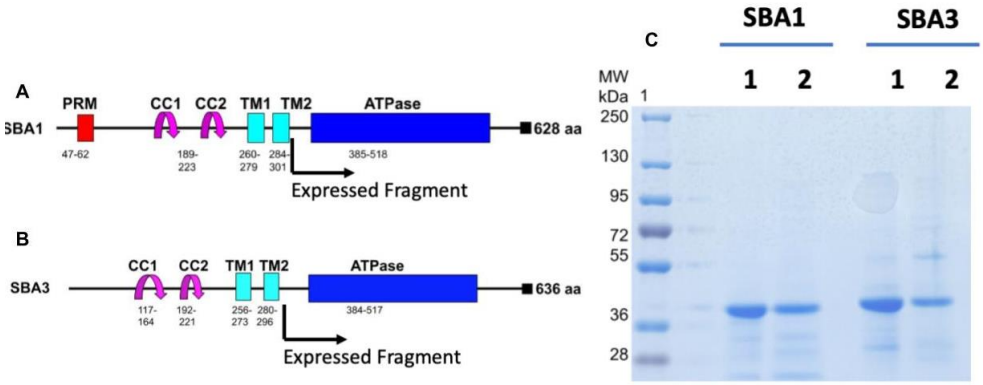

Figure 3.4: Expression and Purification of SBA1c and SBA3c ATPase domains. (A and B) Schematic representation of cloned fragments. C-terminal fragments as described in Chapter 3 were cloned into pET23b His-SUMO expression vectors using PCR primers that amplified from the end of the second transmembrane domain to the end of the coding sequence, and cloned into the destination vector using Gibson Assembly. The same cloning scheme was used for both SBA1 and SBA3. **(C)** SDS-PAGE analysis of purified recombinant SBA ATPase domains**.** SBA1c and SBA3c were purified using IMAC, and the His-SUMO tag was cleaved using ULP1 protease during dialysis. Protein was then reapplied to the nickel column and eluted using Wash I buffer (25 mM Tris-HCl, 300 mM NaCl, 20 mM imidazole, 0.2% Igepal CA-630, pH 7.4). Elution samples were separated on a 5-16% polyacrylamide gel and visualized using Coomassie Brilliant Blue G250 stain. A total of 5 µg of protein was loaded in each well.

3.4.3. Chemical crosslinking shows evidence of moderate SBA C-terminal domain oligomerization

Based on previous work, it had been shown that the C-termini of AAA proteins were insufficient for full oligomerization (Gilquin et al., 2010; Mogk et al., 2003). To test this observation, chemical crosslinking was used with purified *A. thaliana* SBA1c and SBA3c proteins. Two crosslinkers were employed: formaldehyde and DSP (dithiobis(succinimidyl propionate)). Both crosslinking reagents are amine-reactive, meaning that they are compatible with a wide variety of proteins and *in vitro* assays. Specifically, formaldehyde was chosen due to its previous use in crosslinking AAA proteins, its short spacer (2.3 angstroms), and fast reaction

rate. DSP was also included due to a few key features. It is homobifunctional, reversible via reducing agents, and possesses a relatively short 8-Å spacer arm. The minor differences in crosslinker characteristics provided the possibility to validate results from one crosslinker by comparison to the other. Previous work had shown that ATP is necessary for AAA protein oligomerization, so it was added to all experiments. Mg^{+2} is a cofactor for ATPases as it stabilizes anionic intermediates and primes ATP for nucleophilic attack (Zimmerman et al., 1998; Mogk et al., 2003).

Previous work with DSP-mediated ATAD3a crosslinking was completed *in vivo*, but not *in vitro* (Li et al., 2019). To fully understand the effects of DSP on recombinant SBA protein *in vitro*, multiple crosslinker concentrations were employed. DSP-mediated crosslinking of SBA1c (Figure 3.5A) showed little evidence of formation of high molecular weight complexes other than a possible hazy dimer. In contrast, regardless of the DSP concentration a species migrating faster than the untreated monomer was observed, which suggests internal crosslinking of the SBA1c protein. On the other hand, DSP-mediated SBA3c crosslinking showed some evidence of high molecular weight (HMW) complexes, mostly in dimeric and tetrameric states (Figure 3.5B), in addition to the species migrating faster than the monomer. In both SBA1c and SBA3c, crosslinking effects were dependent upon DSP concentration, as the presence of monomeric protein decreased for both proteins. Though HMW complexes were observed in SBA3c, neither protein showed evidence of a hexameric complex, which is considered to be the native oligomeric state of ATAD3a (Baudier, 2018). One confounding factor for the interpreting the data in Figure 3.5 is the resolution of the gels. In these two panels, the regular running buffer for the SDS-PAGE was replaced with Fisher Scientific FastRun Tris buffer. Though this allowed for completion of the run within 30 min, it came at the cost of resolution. It can be clearly seen that the sharpness and uniformity of bands in Figure 3.5 is much poorer than the corresponding bands in Figure 3.6,

in which SDS-PAGE was performed using the standard SDS running buffer. This loss of resolution impacted the ability to interpret results from the DSP crosslinking assay.

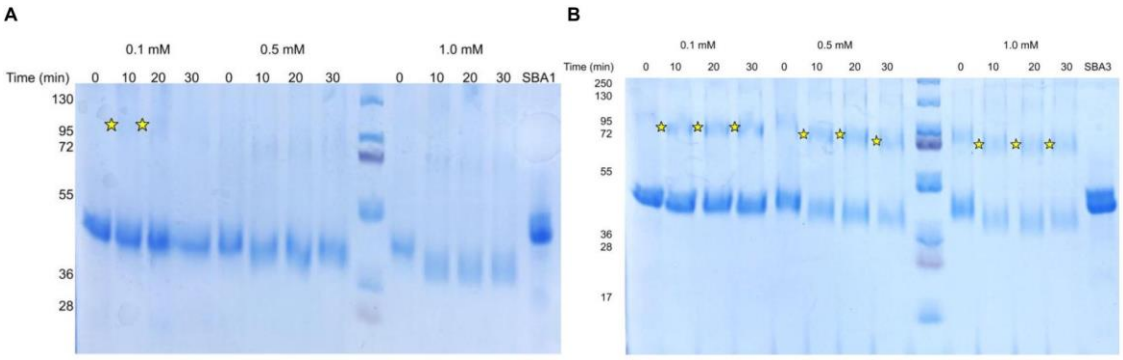

Figure 3.5: SDS-PAGE analysis of SBA1c and SBA3c chemical crosslinking using DSP. In both panels, 5 uM SBA1c **(A)** or SBA3c **(B)** was incubated in reaction buffer with DSP crosslinker, 1 mM ATP, and 1 mM magnesium chloride. DSP was added at 0.1, 0.5, and 1 mM as indicated. Samples were incubated at room temperature until indicated time and quenched using SDS sample buffer with Tris-HCl. Purified recombinant protein is loaded in the rightmost lane as a control. SDS-PAGE results visualized using via FastRun SDS-PAGE and Coomassie Brilliant Blue G-250 staining. Molecular weights in kilodaltons (kDa) listed on the left side of each figure. Stars represent putative oligomeric species. Expected sizes: SBA1c: 36.4 kDa (monomer), 72.8 kDa (dimer), 109.2 (trimer), 145.6 kDa (tetramer), and 218.4 kDa (hexamer). SBA3c: 38 kDa (monomer), 76 kDa (dimer), 152 kDa (tetramer), and 228 kDa (hexamer)

Formaldehyde crosslinking was employed to as an alternative approach to determine the oligomeric state of SBA C-termini. Previous work with AAA protein crosslinking indicated that 1% was a sufficient concentration, but a range of 1% to 4% was used in SBAc crosslinking to

ensure finding an optimal concentration (Mogk et al., 2003). Results showed that there was no clear difference in crosslinking over the same 30 min time span between any concentrations, so 1% was chosen for future assays. Crosslinking of both SBA1c and SBA3c with formaldehyde was consistent with the results seen with DSP (Figure 3.5). A lower molecular weight species was observed for SBA1c (Figure 3.6A), suggesting that internal crosslinking of this protein was not specific to DSP. Similarly, HMW complexes were observed for SBA3c (Figure 3.6B), showing that the C-terminal fragment of SBA3 is more prone to oligomerization while lacking the CC domains compared to SBA1c. In both SBA1c and SBA3c, removal of magnesium chloride from the buffer did not significantly impact oligomerization.

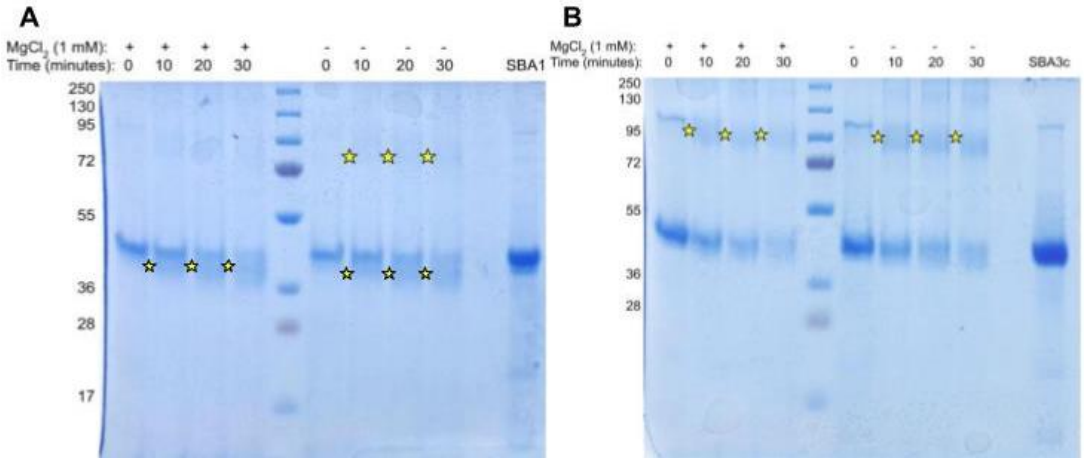

Figure 3.6: SDS-PAGE analysis of SBA1c or SBA3c chemical crosslinking using formaldehyde. In both panels, 5 uM SBA1c **(A)** or SBA3c **(B)** were incubated in reaction buffer with 1% formaldehyde, 1 mM ATP, and 1 mM magnesium chloride where indicated. Samples were incubated at room temperature until indicated time and quenched using SDS sample buffer with Tris-HCl. Purified recombinant protein is loaded in the rightmost lane as a control. SDS-PAGE results visualized using Coomassie Brilliant Blue G-250 staining. Molecular weights in kilodaltons (kDa) listed on the left side of each figure. Expected sizes: SBA1c: 36.4 kDa (monomer), 72.8 kDa (dimer), 109.2 (trimer), 145.6 kDa (tetramer), and 218.4 kDa (hexamer). SBA3c: 38 kDa (monomer), 76 kDa (dimer), 152 kDa (tetramer), and 228 kDa (hexamer). Putative oligomeric species and internal crosslinking products denoted with a star.

It is interesting that these two proteins showed a different apparent propensity to oligomerize, considering that the sequence identity of the SBA1c and SBA3c protein products is greater than 80%. In fact, these domains are so similar that the SBA1c-specific antibody was shown to react with SBA3c (Figure S.3). However, it was determined that the antibody had at least a 20-fold higher affinity for SBA1c than for SBA3c. Sequence alignment showed that overall, SBA1 shares a similar percent of identity with SBA3 as it does with SBA4 (~60%). Additionally, SBA1 and SBA2 are highly identical (85%). Combined with the results from immunoblotting, it appears that the SBA1c antibody would also react with SBA2c and SBA4c, making it more difficult to plan and execute effective immunoblotting procedures. This remains to be tested.

In addition to SDS-PAGE analysis, immunoblotting was used to see if the increased assay sensitivity would detect additional HMW complexes (Figure 3.7). Due to the availability of an antibody against SBA1c, only SBA1c oligomerization was assessed by this method. The SBA1c antibody does react with SBA3c (Figure S3), but this was not evaluated until after the crosslinking experiments. For SBA1c immunoblotting, standard concentrations of formaldehyde (1%) and DSP (1 mM) were selected, and the crosslinking assay was repeated with SBA1c. In addition, a separate aliquot of the 30 min timepoint sample was removed and treated with 10 mM DTT prior to gel loading to determine if the chemical crosslinking of SBA1c was reversible. A total of 100 ng of SBA1c was analyzed for each timepoint of the crosslinking, and then separated by SDS-PAGE. The immunoblot was processed with anti-SBA1c primary antibody (1:2,000) and goat HRP-conjugated anti-rabbit secondary antibody (1:5,000) to detect SBA1c. With both formaldehyde and DSP crosslinking, there is evidence of intra-molecular crosslinking of SBA1c (Figure 3.7), though the effect is more prominent in the DSP samples. However, there are bands at approximately 72 and 100 kDa in the formaldehyde samples, which are sizes consistent with

the molecular weights for SBA1c dimers and trimers (72.8 and 109.2 kDa, respectively). Bands consistent with SBA1c dimers can also be observed in the DSP samples. Overall, these data suggest that there is partial oligomerization of SBA1c and SBA3c, but that these C-terminal fragments are insufficient for stable hexamerization of the protein or that buffer or other conditions do not favor oligomerization.

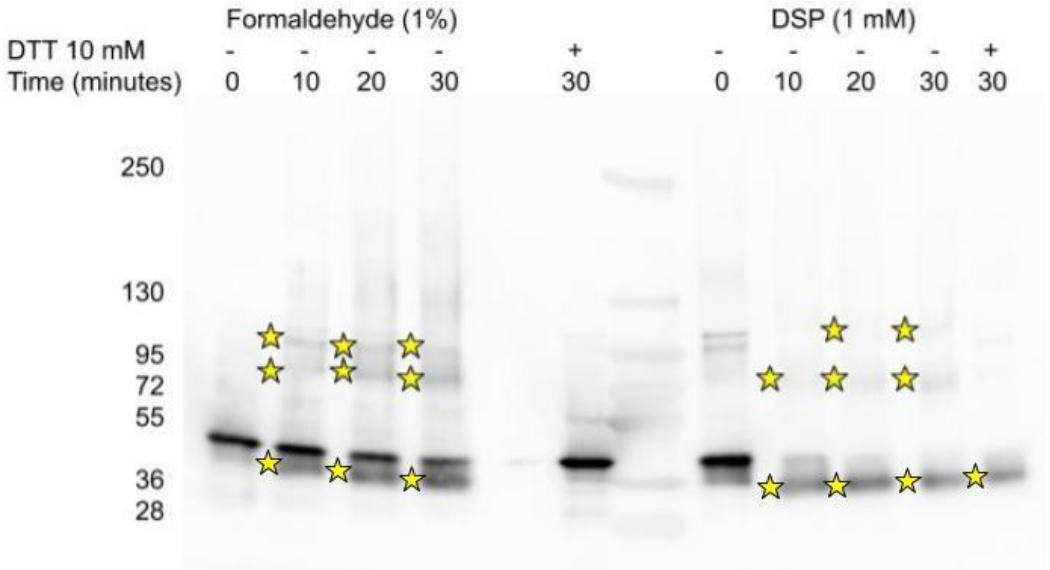

Figure 3.7: Immunoblot analysis of SBA1c crosslinking. Aliquots were taken from crosslinking samples in Figures 3.5 and 3.6 to load 100 ng of SBA1c per lane. The reducing agent DTT was added to an additional aliquot of the 30 min samples to test reversibility of formaldehyde and DSP crosslinking. Samples were separated via SDS-PAGE, transferred onto nitrocellulose membrane, and probed with anti-SBA1c primary antibody (1:2,000) and goat anti-rabbit HRP conjugated secondary antibody (1:5,000). ECL chemiluminescent signal was captured using a GBOX imager. Expected sizes for SBA1c: 36.4 kDa (monomer), 72.8 kDa (dimer), 109.2 (trimer), 145.6 kDa (tetramer), and 218.4 kDa (hexamer). Putative oligomeric species and internal crosslinking products denoted with a star.

3.4.4 Size exclusion chromatography validates moderate SBA C-terminal domain oligomerization

As an alternative approach to assess the oligomeric states of SBA1c and SBA3c, I used size exclusion chromatography (SEC) with a high-performance liquid chromatography (HPLC) system. Protein was monitored with an ultra-violet detector set to 280 nm and 210 nm to measure

absorbance of residues and peptide bonds, respectively. To keep SBA1c and SBA3c in solution, a mobile phase was selected that closely resembled the storage buffer of these proteins (25 mM HEPES, 300 mM NaCl, 0.2% IGEPAL CA-630). A problem arose, pertaining to the gel filtration standard used in these assays. The Bio-Rad protein standard containing thyroglobulin (bovine, 680,000 kDa), γ-globulin (bovine, 158,000 kDa), ovalbumin (chicken, 44,000 kDa), myoglobin (horse, 17,000 kDa), and Vitamin B12 (1,350 kDa) was used to determine the relative masses of species based on retention time. However, the first trials using the aforementioned mobile phase showed no readable signal for any of the standard proteins. The standard was applied in the running buffer (25 mM HEPES, 300 mM sodium chloride, 0.2% Igepal CA-630), as well as the same buffer without Igepal CA-630. Based on these results, it was determined that the standard proteins were incompatible with Igepal CA-630, as discreet peaks were only observed in mobile phases lacking this component (Figure 3.8A).

Both SBA1c and SBA3c were diluted to a concentration of 10 μM and analyzed separately in the mobile phase containing Igepal CA-630. The absorption maximum of both samples at 210 nm occurred at 14.1 min, consistent with the minor difference in molecular weights of the two proteins (Figure 3.8, B and C). Upon the addition of 2 mM ATP and 2 mM Mg^{+2}, a second peak was seen in both samples at 10.8 min (Figure 3.8, D and E). This reduction in retention time indicated there was a higher molecular weight species in both samples, suggesting some degree of oligomerization had occurred. Both samples also showed the later eluting peaks at 14.1 min, but this peak was noticeably lower in the SBA3c samples with ATP and Mg^{+2}. This result paralleled the observations that SBA3c oligomerized to a greater extent than SBA1c with chemical crosslinking. The results also demonstrated that both proteins are capable of oligomerization to a limited extent, as monomeric species were still observed in samples containing ATP and magnesium cofactors. However, interpreting these data was

challenging. The Vitamin B12 from the Bio-Rad standard was only retained for approximately 8 min, shorter than the retention time for any of the SBA1c or SBA3c samples (Figure 3.8A). Because gel filtration/size exclusion chromatography is not a primary measure of molecular mass, I was not able to make any decisive conclusions on the relative mass of the peaks at 14.1 or 10.8 min. It does remain possible that SBA C-terminal oligomerization was promoted via ATP binding, but the exact extent of oligomerization remains unclear.

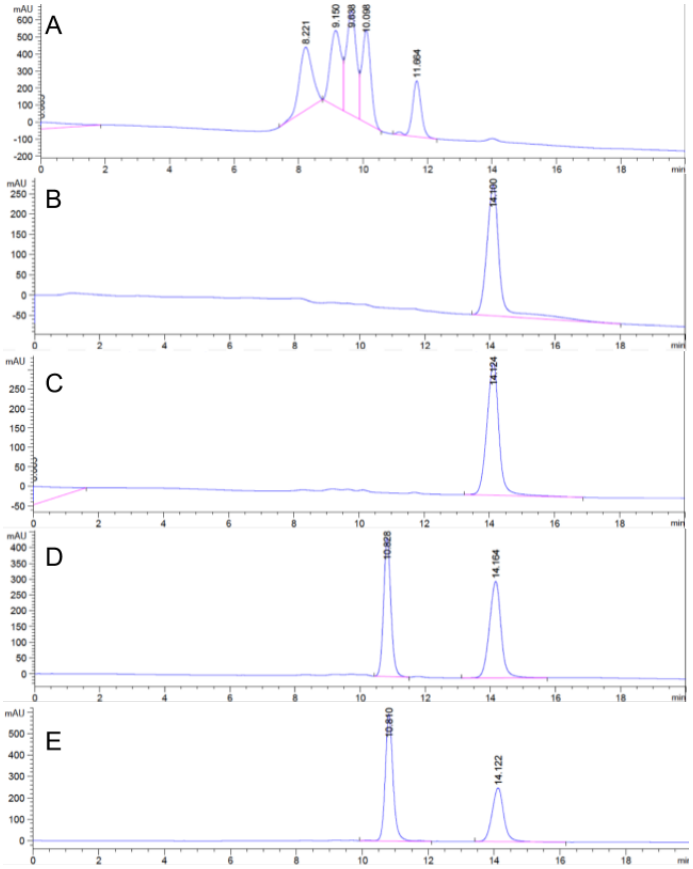

Figure 3.8: Size exclusion chromatograms of SBA1c and SBA3c. Purified recombinant SBA1c and SBA3c were analyzed via HPLC-based SEC using a gel filtration column. Samples were mixed to 10 uM in buffer and separated using a 20 min run. UV spectroscopy used to measure sample absorbance at 210 nm, with absolute absorbance shown on y-axis. Mobile phase retention time (min) is indicated on the x-axis. **(A)** BioRad protein standard chromatogram. Protein was applied in running buffer without Igepal CA-630. **(B)** SBA1c absorbance at 210 nm following SEC without ATP or Mg^{+2}. Protein samples were diluted to 10 uM and loaded immediately. Peak appears at 14.1 min for SBA1c. **(C)** SBA3c absorbance without ATP or Mg^{+2}. Peak appears at 14.1 min. **(D)** SBA1c 210 nm absorbance following SEC and incubation with ATP and Mg^{+2} (2 mM each) for 5 min at room temperature prior to sample application. Dual peaks occurred at 10.8 and 14.1 minutes. **(E)** SBA3c 210 nm absorbance following SEC with ATP and Mg^{+2} at above concentrations. Dual peaks occur at 10.8 and 14.1 min. All chromatograms generated using Agilent Chemstation software.

3.4.5. SBA C-termini may not be sufficient for ATP hydrolysis

Previous data have shown two key characteristics of ATAD3a: oligomerization is regulated by ATP binding (Gilquin et al., 2010) and the oligomeric state of ATAD3a is regulated by interaction with the mitochondrial fission machinery (Li et al., 2019). Based on these observations, I set out to test the ATPase activity of SBA1c and SBA3c to determine if these domains were sufficient for activity. Malachite Green was used as a reporter, as it reacts with free Pi cleaved from ATP to produce a signal that is measurable at 620 nm (Zhou et al., 2019). ClpX, the ATPase domain of the *Caulobacter crescentus* ClpXP machinery, was used as a positive control for ATPase activity (LaBreck et al., 2017). Both SBA1c and SBA3c assayed in 96-well plates at two separate concentrations to ensure that no one concentration was high enough to cause Malachite Green precipitation. ClpX control was only assayed at one concentration due to material limitations. Empty wells containing only buffer and ATP were used as a control for background, as it was possible that ATP could have degraded to ADP and Pi during the assay set up. The average fluorescence of the ATP-only wells was subtracted from the fluorescence produced in experimental wells to eliminate background Pi signal. This assay showed that after adjusting to pmols Pi per µM ATPase in solution, both SBA1c and SBA3c are deficient in

ATPase activity (Figure 3.9). SBA1c and SBA3c not only produced less free Pi, but were also incapable of sustained ATPase activity after approximately 10 min of incubation. Conversely, ClpX showed increased Pi formation per µM of protein, and also a larger amount of Pi formed over time. Based on these results, it was concluded that the C-terminal fragments of SBA proteins are insufficient for ATPase activity.

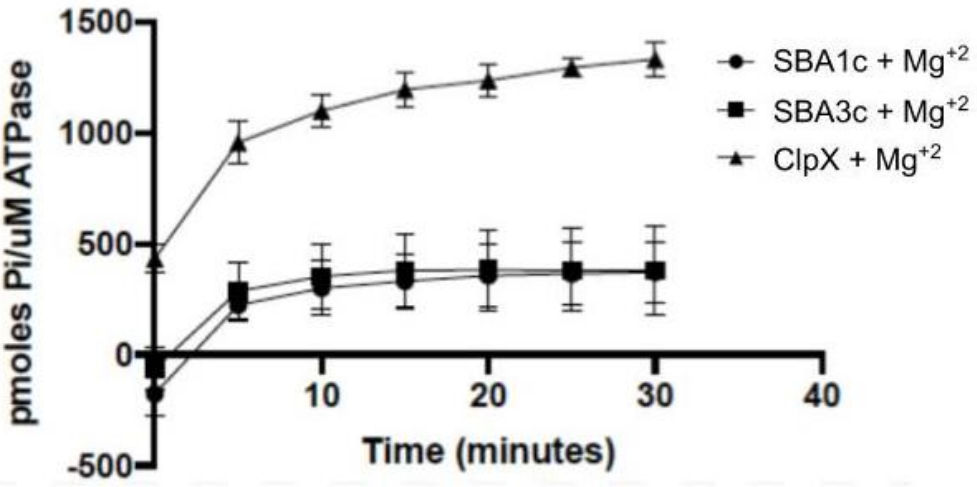

Figure 3.9: Rate of ATP hydrolysis by SBA1c, SBA3c, and ClpX. Previously purified SBA1c and SBA3c were used in addition to recombinant ClpX ATPase (courtesy of the Dr. Peter Chien lab). ATP hydrolysis rate in buffer solution plus magnesium chloride was measured using a Malachite Green solution. Reaction was incubated in the dark at 22 ºC for 30 min, with spectrophotometric measurements at 620 nm recorded every 5 min.

One key deviation from the manufacturer's protocol was related to incubation time. Previous assays using ClpB, a AAA protein, showed that mutant proteins deficient in oligomerization (similar to coiled-coil mutation in SBA proteins) had a five-fold reduction in ATPase activity, with some oligomerization-defective mutants having no measurable ATPase activity (Mogk et al., 2003). The goal of this assay was to generate a time-dependent curve in order to understand the rate of SBA1c and SBA3c hydrolysis rather than just their overall

capacity to hydrolyze ATP. In order to achieve this, a variation was made: the manufacturer's protocol stated that protein and buffer must be incubated for 30 minutes with the Malachite Green reagent. However, I set up the assay with the protein, buffer (including cofactors) and Malachite Green, and then immediately inserted the plate into the spectrophotometer. This allowed data to be captured from the onset of ATPase activity. The alternative approach would have been to incubate for 30 minutes and then measure the time course for an additional 30 minutes, but this method would not have allowed me to measure ATPase activity at the onset of protein being added to substrate. Employing this strategy would have been disadvantageous because it was possible that the SBA1c and SBA3c fragments would not have been able to sustain ATPase activity past the initial 30 minute incubation.

3.4.6. *In vivo* assessment of SBA homo- and hetero-oligomerization using Bimolecular Fluorescence Complementation (BiFC)

As mentioned previously, the human ATAD3a has been the most widely characterized homologue of the plant SBA proteins. Previous studies have shown that although humans also have ATAD3b and ATAD3c, it is ATAD3a that is the most highly expressed (Baudier, 2018). Furthermore, *in* vitro crosslinking showed that it is possible for ATAD3a to form hetero-oligomers with ATAD3b, though this is much less likely than the formation of an ATAD3a homohexamer. In the case of the plant SBA proteins, it is known that SBA1, SBA2, and SBA3 are expressed at relatively similar levels throughout different tissues, though SBA4 expression is lower (Heazlewood et al., 2004; Tanz et al., 2005). Genetic analyses also showed that at least one protein per clade was necessary for growth and development, but further interactions had not been assessed. Because of these two observations, I hypothesized that the reason for SBA double mutant lethality was due to the need for multiple SBA proteins to form a hetero-oligomer.

To assess SBA protein interactions *in vivo*, vectors for bimolecular fluorescence complementation (BiFC) assays were developed. BiFC allows visualization of proteins *in vivo* using two non-fluorescent halves of a fluorescent protein separately conjugated to two proteins of interest (Kerppola, 2008). If the two proteins of interest are brought into close proximity, the conjugated protein fragments form a fully fluorescent protein. Consequently, the fluorophore can be observed using confocal microscopy. This system presented a relatively easy way to gauge which, if any, SBA proteins interacted *in vivo*.

Previous work in the Vierling Lab made use of BiFC technology to show that SBA1 interacts with itself *in vivo* (Figure 3.10). A vector containing SBA1 conjugated to either the N- and C-terminal halves of YFP was transiently expressed in tobacco leaf epidermal cells and produced fluorescent signal localized to mitochondria, while controls expressing unconjugated fluorescent protein did not fluoresce. To test interactions of other SBA proteins, each SBA protein was cloned into the pSPYNE (nYFP) and pSPYCE (cYFP) vectors to create separate N and C-terminal YFP fusions for each protein (Table 2.3). This cloning scheme also allows testing all possible combinations of SBA proteins with each other. Proper in-frame insertion of the coding sequences was confirmed by both restriction enzyme digestion and sequencing. These expression clones are now available to test a total of 25 vector combinations to assess SBA *in vivo* interactions (Table 3.2). In addition to each SBA nYFP/cYFP combination, empty vectors containing non-conjugated nYFP or cYFP (pSPYCE and pSPYNE) are also available as negative controls, as they are not expected to produce fluorescent signal when transiently expressed in tobacco leaf cells.

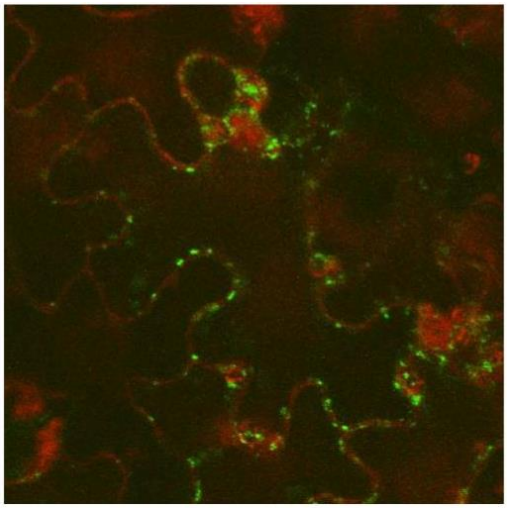

Figure 3.10: SBA1-nYFP SBA1-cYFP produces fluorescent signals in tobacco leaf epidermal cells. Data courtesy of Dr. Minsoo Kim. Infiltration of tobacco leaves with pMK179 (SBA1-nYFP and SBA1-cYFP independently included on the same vector) showed fluorescent signal in confocal microscopy using the FITC green channel. TRITC channel also shown (red) to identify chloroplasts. Green punctae are mitochondria, localized in the cytoplasm pressed up against the cell periphery by the central vacuole.

Table 3.2: BiFC vector cotransformation combinations and controls

	SBA1 C-YFP pSZ14	SBA2 C-YFP pMK130	SBA3 C-YFP pSZ16	SBA4 C-YFP pSZ17	Empty C-YFP pSPYCE
SBA1 N-YFP pSZ10	(+) Control	?	?	?	(-) Control
SBA2 N-YFP pSZ11	?	?	?	?	(-) Control
SBA3 N-YFP pSZ12	?	?	?	?	(-) Control
SBA4 N-YFP pSZ13	?	?	?	?	(-) Control
Empty N-YFP pSPYNE	(-) Control	(-) Control	(-) Control	(-) Control	(-) Control

3.5. Discussion and outlook on further work

Previous data on AAA+ proteins shows that an overwhelming majority of these proteins are functionally active as hexamers and that their activity depends on this oligomerization (Vale, 2000; Lupas and Martin, 2002; Mogk et al., 2003). Furthermore, previous data show that the human SBA homolog ATAD3a hexamerizes as well (Gilquin et al., 2010; Baudier, 2018), though some data from human neuronal cells suggests a dimeric form (Zhao et al., 2019). Overall, the consensus is that the oligomerization of ATAD3a has direct effects on mitochondrial morphology and health. Considering the importance of the ATAD3a oligomeric state, and the fact that it has not been defined in plants, it was my aim to investigate the basics of SBA oligomerization. This aim brought me to question which domains are necessary for oligomerization, and if hetero-oligomerization of SBA proteins is possible or necessary. The assays conducted in this chapter have laid a foundation of data and research materials, including purified proteins and plasmid vectors, that will allow for other researchers in the Vierling Lab to continue addressing this important question.

Based on the data acquired through chemical crosslinking, the C-terminal fragments of SBA proteins are insufficient for hexamerization. Bands suggesting partial oligomerization of both SBA1c and SBA3c were observed using both formaldehyde and DSP, but these were insufficient to demonstrate the exact oligomeric state of the C-terminal fragments. Further steps would involve repeating the crosslinking experiments to validate earlier findings, and to obtain higher resolution separation of bands by SDS-PAGE than were achieved with the fast running buffer. Subsequently, it will be of interest to determine if the full length SBA proteins can be purified as well, and to subject them to the same assays. Understanding the oligomerization patterns of the full length SBA proteins will allow us to more fully understand the data acquired from crosslinking of C-termini. It may be possible that the full length proteins will show a

propensity to form poorly resolved dimers, similar to their C-terminal counterparts; conversely, it is possible that the full length proteins will show vastly different oligomerization patterns.

SEC assays provided qualitative evidence of SBA C-terminal oligomerization through the clear peak shift. However, these data are still incomplete. Due to the fact that SBA C-terminal truncation proteins were subject to precipitation in solution, they require addition of surfactants such as IGEPAL CA-630 in order to remain soluble during assays like SEC. However, it was also determined that the molecular weight standard is not compatible with the addition of this surfactant. Therefore, the standard was applied in a mobile phase that did not contain Igepal CA-630, which in turn altered the retention times of the standard proteins. As the SBA proteins were insoluble without Igepal, but standard proteins were not resolved in SEC with Igepal, the apparent molecular weight of the SBA proteins in Figure 3.7A-D cannot be determined based on the chromatogram of the Bio-Rad standards. Though SEC is not a primary method of determining molecular weight, results would have provided context as to the extent of oligomerization of the SBA1c and SBA3c proteins. Without these data, the assessment of SBA1c and SBA3c oligomerization via SEC remains incomplete. Still, the shortened retention time upon addition of ATP and Mg^{+2} cofactors suggests that a larger protein complex is present upon addition of these components.

Further SEC experiments would depend on the identification and production of a buffering system that is compatible with both the Bio-Rad protein standard as well as the SBA C-terminal proteins. Upon completion of this step, repeating the same assay with and without ATP and Mg^{+2} cofactors would allow for interpolation of molecular weight as a function of retention time. This would provide preliminary data on the extent of SBA C-terminal oligomerization and open pathways to other assays such as mass spectrometry or SEC-MALS to accurately determine

molecular weights of possible SBA C-terminal oligomers. As mentioned above, purification of SBA full length proteins for the purposes of SEC applications is an important next step.

ATPase assays also indicated that the SBA C-terminal fragments are insufficient for activity on their own. A limitation in this assay is that the positive control used was ClpX. A better positive control would have been using a recombinant full length SBA protein, provided they could be purified. This would allow us to normalize the rate of ATP hydrolysis of each SBA C-terminal peptide to its respective full length cognate. Instead of dealing with data relating to the absolute ATP hydrolysis rate, using the relative rate would highlight exactly how detrimental the loss of CC oligomerization domains can be to SBA activity.

Another issue to address in future studies involving the ATPase assay is the variation from the manufacturer's protocol. As stated in the results, SBA1c and SBA3c stopped producing Pi after approximately 10 minutes, meaning that a time course using the manufacturer's protocol (30 minute incubation, then the 30 minute time course) would have shown no differences from T=30 to T=60. This means that it may not be feasible to conduct a time course assay using this kit. An alternative approach would be to repeat this ATPase assay but with measurements at the start and end of this assay. Although this would not provide data on the production of Pi over time, it would at least provide data on the overall ability of SBA1c and SBA3c to catalyze ATP hydrolysis.

In addition to repeating and optimizing the above-described assays, additional steps involving protein purification are necessary to fully address the questions posed in this chapter. First, full-length SBA proteins were cloned into expression vectors, but have not yet been purified or even tested for expression level and solubility. Purification of these full-length SBA proteins will prove challenging due to their membrane localization. In previous work on SBA

homologues, it was shown that the C-terminal ends of the ATAD3a protein localizes within the mitochondrial matrix, where it does not interact with membranes (Gilquin et al., 2010). However, TM and CC domains are known to be membrane-interacting domains, suggesting that keeping them in solution will prove challenging.

Another important undertaking in protein purification is the production of recombinant SBA2c and SBA4c. The coding sequences for both of these C-terminal domains have been cloned into pET23b His-SUMO expression vectors (Table 2.2), but these proteins have not yet been purified. As mentioned in the introduction to this chapter, the four SBA proteins are highly similar in terms of their domain organizations. However, most other non-plant organisms have only one ATAD3 protein that is actually expressed and active. Purification of SBA2c and SBA4c will allow us to interrogate the differences in functionality between all four SBA C-terminal domains. This may lead to relevant data, such as possible differences in ATPase activity or oligomerization between the four C-terminal domains. Combining the purified SBA2c and SBA4c proteins in the previously established assays, as well as all four full-length SBA proteins will allow us to start assessing the functional similarities and differences between the four proteins. These observations will be key in understanding the discrete roles of the four SBA proteins in *A. thaliana* and higher plants in general.

An exciting open path towards understanding the functional relationships of the four SBA proteins is through the use of BiFC. Previous results (Figure 3.8) demonstrate that this is a viable technology for establishing interactions between SBA proteins. Additionally, all 10 BiFC constructs have been cloned and transformed into electrocompetent cells for tobacco infiltration. This library of 10 constructs will allow us to test the interaction of each SBA protein with every other SBA protein, for a total of 25 different vector combinations. The availability of empty pSPYNE (unconjugated N-terminal half of YFP) and pSPYCE (unconjugated C-terminal half of

YFP) vectors provides a built-in control to easily discern between a true SBA-SBA interaction and the random association between an unconjugated YFP fragment and an SBA-YFP fusion. Additionally, all the reciprocal approaches are available as well; for example, one combination of SBA1-nYFP/SBA3-cYFP and a separate BiFC combination of SBA3-nYFP/SBA1-cYFP. The availability of this *in vivo* system allows for validation, easy recognition of interaction, and highly specific controls.

CHAPTER 4 : DOES THE *SHOT1-2* MUTANT IMPACT ER-MITOCHONDRIA CONTACT SITE DYNAMICS?

4.1. Introduction

As described in Chapter 1, a mutant allele of SHOT1/mTERF18, *shot1-2*, restores heat stress tolerance to HSP101-deficient plants (Kim et al., 2012). Though *shot1-2* plants have a retarded growth phenotype, they are able to rescue *hot1-4* heat sensitivity in an HSP101-independent manner, and they are more heat tolerant than wildtype plants. In studies designed to better understand the molecular function of SHOT1/mTERF18, co-immunoprecipitation and mass spectrometry using SHOT1 as the bait protein discovered that SHOT1/mTERF18 interacts with SBA proteins (Kim et al., 2012). As described in Chapters 1 and 3, the SBA homolog ATAD3a has been shown to regulate the dynamics of ER-mitochondria contact sites (ERMCS) *in vivo* in animals. Specifically, dysfunction of the ATAD3a oligomer in human neuronal cells through loss of ATP hydrolysis or loss of hexamerization has been shown to activate DRP1 fission machinery (Zhao et al., 2019). This pathway has also been characterized as part of a broader activation of mitophagy, ultimately leading to mitochondrial destruction due to stress conditions (Zorov et al., 2019). Although the same mitophagic pathway has not been demonstrated in plants, two *A. thaliana* DRP1 homologues (DRP3a and DRP3b) have been identified. Considering that ATAD3a homologs SBA1, SBA2, and SBA3 were all identified through Co-IP with SHOT1, it raises the question of whether or not SHOT1 could somehow function within the same ERMCS regulatory pathway.

The same crosslinking and Co-IP approach was also applied to identify any possible nucleotide binding capacity of SHOT1. These experiments showed that SHOT1 binds *A. thaliana* mtDNA at specific locations along the genome, putatively suggesting that SHOT1 is somehow

responsible for nucleoid maintenance (Kim et al., 2012). This hypothesis is based in part on the characterization of other mTERF family proteins in animals, which have been known to bind and maintain mitochondrial DNA via transcriptional regulation (Kleine, 2012).

The above two observations about SHOT1- functional association with SBA proteins and mtDNA binding were of immediate interest. The regulation of ERMCS by ATAD3a is a well-known and well-characterized function of the ERMIONE complex. Additionally, the MICOS and ERMES subcomplexes are known to regulate tethering and functional association of these two organelles (Friedman et al., 2018; Kundu et al., 2020). It has also been reported that both subcomplexes are involved in the regulation and maintenance of mtDNA (Kozjak-Pavlovic, 2016; Peralta et al., 2018; Kundu et al., 2020). Considering the similarities in function between SBA, SHOT1 and ERMIONE proteins, I considered that SHOT1 may affect contact site dynamics via SBA proteins and the putative DRP3a-mediated fission/mitophagy pathway. To this end, the primary aim was to first visually identify if the *shot1-2* allele affected the ERMCS via confocal microscopy.

Previous work has established multiple strategies for *in vivo* visualization of organelles/organellar contact sites using confocal microscopy. In yeast and mammalian systems, confocal microscopy has been used in conjunction with BiFC (described in Chapter 3) to establish protein-protein interactions at the ER-mitochondria interface (Kakimoto et al., 2018). Similarly, a large amount of research has used fluorescently labelled proteins to observe organellar dynamics in plants- specifically in both the mitochondria and the ER. To form my experimental approach, I focused on understanding both ER and mitochondrial fluorescent visualization separately, in addition to simultaneous ER-mitochondria imaging (Nebenfuehr et al., 2006; Gotté et al., 2016).

The simplest method of visualizing plant organelles is through transformation with localized fluorophores. In the case of the ER, a short KDEL or HDEL ER retention motif conjugated to a fluorophore is sufficient for localization (Matsushima et al., 2003). Using this system, multiple different research groups visualized the ER in plants, and found that the fluorophores tended to localize to what are now known as ER bodies (Hayashi et al., 2001). ER bodies have been found in many species of the order *Brassicales*, but most investigations have focused on *A. thaliana* specifically (Nakano et al., 2014). These structures are about 10 μm long by 1 μm wide and tend to be surrounded by ribosomes (Matsushima et al., 2003). Though they are contiguous with the ER membrane, previous characterization shows that they tend to fuse with vacuoles during stress. Understanding this morphology is key to interpreting results from confocal microscopy images.

One other important factor in understanding the ER body is to take into account the localization of its fluorescent signal in the root. Because plant roots lack chloroplasts, they present a much easier tissue for fluorescent visualization due to the lack of background signal from chlorophyll. The cells of the root also divide faster than most other regions of the plant, which promotes expression of stably transformed constructs (Dolan et al., 1993). The overall structure of the plant root involves four discreet zones: differentiation, elongation, meristematic, and root cap zones. As shown in Figure 4.1, each of these zones produces a different type of ER body fluorescence, a feature that has to be considered during microscopy.

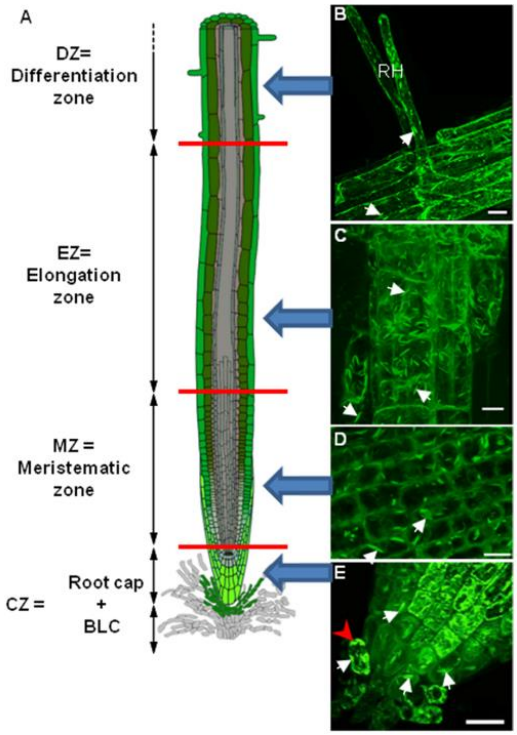

Figure 4.1: Differential fluorescent signals from ER bodies are dependent upon location in the plant root. GFP fused to the HDEL ER-retention signal viewed in stably transformed *A. thaliana* seedlings. Confocal microscopy was used to observe GFP fluorescence representing ER bodies in seedling roots, which could be found in all four zones of the root. Red bars represent microdissection sites. Scale bar equals 10 μm. Image adapted from Gotté et al., 2016.

To visualize ER-Mitochondria interaction, in addition to fluorescently labelled ER, it was obviously necessary to include fluorescently labelled mitochondria. Mitochondrial labelling has been extensively characterized in plants. The most common method is transformation of plants with Mito-GFP, a construct expressing GFP conjugated to a mitochondrial targeting peptide. Transformation with this construct creates fluorescent signal from within the mitochondrial matrix, allowing visualization of mitochondria in microscopy images. Fluorescent punctae from the mitochondrion are about 0.5 μm to 1.5 μm in diameter, but vary depending on stress or light

stimulation (Jaipargas et al., 2015). In contrast to the varied nature of ER body signals, fluorescently labelled mitochondria tend to produce similarly-sized signals throughout the plant.

My goal for these experiments was to produce homozygous Col-0 and *shot1-2* plant lines stably transformed with both ER- and mitochondria-targeted fluorophores. By simultaneously imaging both these labelled organelles, I aimed to identify differences in mitochondrial or ER morphology to gauge the effects of the *shot1-2* mutation. A secondary goal was to identify perturbations in typical ERMCS dynamics such as loss of contact, or conversely, increased contact between the organelles. Previous reports have shown that mitochondrial fission/fusion are dependent upon these contact sites, so understanding if they are affected by *shot1-2* is key in understanding the underlying molecular phenotype of this mutation (Anderson et al., 2019).

4.2. Plant lines were produced with fluorescently labelled mitochondria and ER

To address the goals defined above, the construct pRTdsGFP was transformed into the lines Col-0 and *shot1-2* by Dr. Minsoo Kim. This construct contains the GFP coding sequence fused to a mitochondrial targeting peptide. Henceforth, these lines will be referred to as Mito-GFP and *shot1-2* Mito-GFP, respectively. These lines were also screened by Dr. Minsoo Kim, who identified homozygous insertion of the Mito-GFP gene. Subsequently, the ER-rb was stably transformed into the homozygous Mito-GFP and *shot1-2* Mito-GFP lines, as well as Col-0 and *shot1-2*. Th ER-rb plasmid, courtesy of Dr. Andreas Nebenfuehr, contains mCherry, a red fluorescent protein, conjugated to an ER-anchoring HDEL motif (Nelson et al., 2007). Additionally, it also encodes the BASTA herbicide resistance gene used to screen for transformed plants. Seeds from the four transformed plant lines (courtesy of Dr. Minsoo Kim) were screened using the BASTA selective marker until homozygotic lines of each construct were obtained. To obtain homozygous transformed lines, T2 seeds were screened using BASTA resistance. For this

screen, any plants showing 3:1 growth ratio of resistance/non-resistance to BASTA were transplanted to soil and grown for additional screening. This strategy was used to ensure that there is only one insertion site of the transgene into the genome, allowing for simple identification of homozygotes. Finally, the T3 screen was conducted by plating seeds from all T2 plants that were cultivated from the T1 screen. The offspring of these plants were screened for 100% growth on BASTA, indicating that they were homozygous for the ER-rb insertion. To obtain a substantial seed stock, 4 plants from each homozygous parent were grown on soil and harvested. A total of 3 independent lines were established for Col-0, 1 for Mito-GFP, 1 for *shot1-2*, and 2 for *shot1-2* Mito-GFP. A summary of all plant lines and parental lineages can be found in Table 4.1.

4.2.1. Expression and localization of fluorophores were confirmed in all lines

Herbicide resistance alone is insufficient to know that lines carrying the ER-rb or Mito-GFP transgene are properly expressing the RFP and GFP fluorescent proteins. To test transgene expression by confocal microscopy, non-transformed Col-0 was included alongside Col-0 ER-rb to confirm that RFP signals were present and properly localized within root cells. Even though all plants used in this assay were homozygous, they were grown on BASTA-containing medium to ensure that seedlings contained the transgene. After approximately seven days of growth (depending on genotype), plants were mounted on glass slides and imaged using confocal microscopy. To observe fluorescent signals, the meristematic and differentiation zones of the roots were used, as these lack chlorophyll and widely express transformed fluorophores (Gotté et al., 2016). For the Col-0 and Col-0 lines, only the TRITC (red fluorescence) channel was used for image capture as there was no fluorescence from the FITC (green fluorescence) channel.

To examine expression and localization of ER-rb, I chose the Col-0 line 12.7.1, based on its robust growth during the T2 screen, in addition to untransformed Col-0 (courtesy of Dr. Minsoo

Kim). Images showed that Col-0 produced minimal background signal as compared to Col-0 ER-rb (Figure 4.2). The Col-0 ER-rb line produced multiple bright punctae of varying size, mostly dispersed throughout the middle of the imaged cells. Interestingly, not all cells produced fluorescent signal. However, based on the signals that were present, they appear to be consistent with the observed patterns of ER body fluorescence.

In the Col-0 ER-rb images, it was also observed that many of these ER bodies varied in size. Those in the upper-left side of the image produced large, disperse signals, while those in the bottom right showed a much smaller and more discrete set of fluorescent signals (Figure 4.2). Overall, imaging of the Col-0 and Col-0 ER-rb lines confirmed expression of the ER-rb transgene. Additionally, the localization and shape of the mCherry signal also confirms properly labelled ER bodies based on the similarity to previously characterized ER body fluorescence (Gotté et al., 2016). In addition to their importance in confirming expression and localization, these lines also provided a frame of reference for mCherry signals for additional experiments. In addition to mCherry, it was also important to provide relevant controls for Mito-GFP fluorescence. Capturing images of Mito-GFP lines transformed with ER-rb for the purposes of fluorescent microscopy allowed for the imaging of wild-type ER and mitochondria. Obtaining these images was key, as any differences in organellar dynamics in the *shot1-2* background will be based on the context provided by Mito-GFP ER-rb plants.

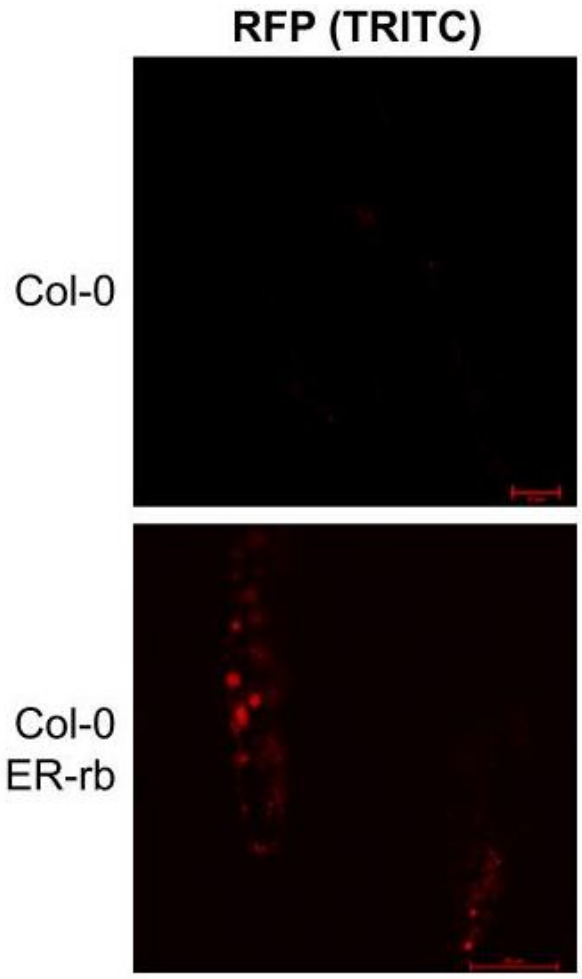

Figure 4.2: Confocal microscopy images of Col-0 and Col-0 ER-rb roots. Seedling roots were imaged using the Nikon A1SP confocal microscope following 10 days of growth. The TRITC channel was used to observe red fluorescence of the ER-localized mCherry fluorophore, expressed via the ER-rb construct.Col-0 ER-rb lines 12.7.1 was used in fluorescence microscopy, and Col-0 controls were obtained from Dr. Patrick Treffon.

Images of Mito-GFP ER-rb plant roots from line 3.3.10 (Figure 4.3) were captured through the FITC and TRITC channels and by differential interference contrast (DIC). The images confirmed that the plants were stably transformed with both Mito-GFP and ER-rb. The latter produced similarly sized punctae as compared to Col-0 ER-rb, with comparable localization patterns (Figure 4.3). Merging the two fluorescent channels showed some contact and overlap

between GFP and mCherry signals. Most of these fluorescent punctae appear to be in the same general vicinity, but it is difficult to prove co-localization due to the insufficient resolution at the given magnification. However, it has been previously defined that many mitochondrial dynamic processes are dependent upon ER-mitochondria contact sites, making it plausible that these organelles are in close proximity (Baudier, 2018; Wideman and Munoz-Gomez, 2016).

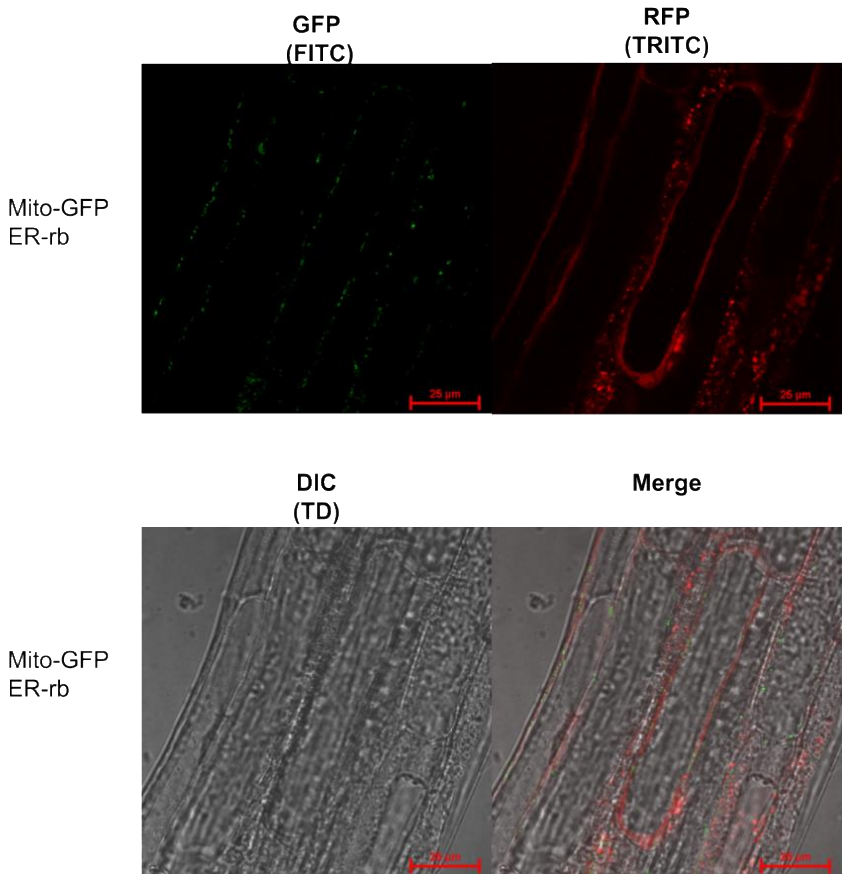

Figure 4.3: Confocal microscopy images of Mito-GFP/ER-rb-transformed plants. Seedlings previously transformed with both Mito-GFP and ER-rb were grown, and roots were imaged after 10 days. Images were captured for green (FITC), red (TRITC), and differential interference contrast (TD) channels and overlaid in one merged image. The elongation zone of the root was used for image capture via the Nikon A1SP confocal microscope. All four images are from the Mito-GFP ER-rb line 3.3.10. Scale bars represent 25 µm.

4.3. *shot1-2*-background plants exhibit altered fluorescent signals

In addition to the validation of ER-rb fluorescence in Col-0 and Mito-GFP backgrounds, a *shot1-2* ER-rb line was imaged in addition to two independent lines of *shot1-2* Mito-GFP ER-rb. Previous microscopy work involving *shot1* mutants (*shot1-1* and *shot1-2*) showed presence of many enlarged mitochondria in excess of 3 um in diameter (Kim et al., 2020), a marked increase from the typical 1 um diameter seen for plant mitochondria (Alberts et al., 2002). A similar phenotype was observed with the mitochondria of *shot1-2* mutants in my experiments (Figure 4.4). Visually, there appear to be more fluorescent mitochondrial signals in the *shot1-2*-background plants, especially in line 4.6.2. This is possible evidence of upregulated mitochondrial fission, a phenomenon that occurs in dysregulated mitochondria. Prior data demonstrated that *shot1-2* mutants did have mitochondrial dysfunction as evidenced via OXPHOS complex assembly defects (Kim et al., 2020). The results from confocal microscopy show that these OXPHOS complex assembly defects may be correlated with mitochondrial fission.

In both the *shot1-2* ER-rb and *shot1-2* Mito-GFP ER-rb images, there are marked differences in mCherry punctae as compared to those seen in Col-0 backgrounds. First, fluorescent signals in these lines (Figure 4.4) appear to be clustered together and interspersed throughout the cytosol. This pattern is different than that of Col-0 or Mito-GFP lines (Figures 4.2 and 4.3), where mCherry signal is more discretely bundled. However, this may have been due to the plane of view in the microscopy experiments, as the vacuole can impact the distribution of other organelles in the cell. The punctae in the *shot1-2* background plants also appear to be larger on average than those of Col-0 or Mito-GFP lines. Finally, GFP and mCherry signals in the merged images (Figure 4.4D) do not appear to colocalize in any discrete pattern. Though there is

some overlap between the two, GFP signal mainly appears to localize in separate areas of the cell as compared to mCherry signals.

4.4. Discussion and outlook on further work

Overall, work has been completed to establish independent lines of both Col-0 and *shot1-2* plants transformed with the ER-rb and Mito-GFP constructs for fluorescent labelling of organelles. Initial data confirm that all lines have been successfully transformed with ER-rb based on localization and intensity of the mCherry fluorophore on putative ER bodies. These lines can be used for further confocal microscopy studies to gain more understanding of the dynamics of the mitochondrion and ER in a plant system. Further assays can also be leveraged to understand the potential effects of the mutation in SHOT1/mTERF18, and possibly connect these effects back to the *shot1-2* thermotolerant phenotype.

As mentioned above, *shot1-2* plants tend to show enlarged signals for both GFP and mCherry. Though it was expected that the GFP signal would be enlarged due to the effect of *shot1* on mitochondrial size and morphology, changes in mCherry signal were not anticipated. Previous data have shown that plant mitochondria are reliant upon ER-mediated import for certain proteins via the TOM and TIM complex pathways (Belluci et al., 2017; Wehrhahn et al., 2003). Since the two organelles are so inherently dependent upon each other for normal function, it may be that ER dysfunction also occurs in the retarded growth phenotype of *shot1-2*.

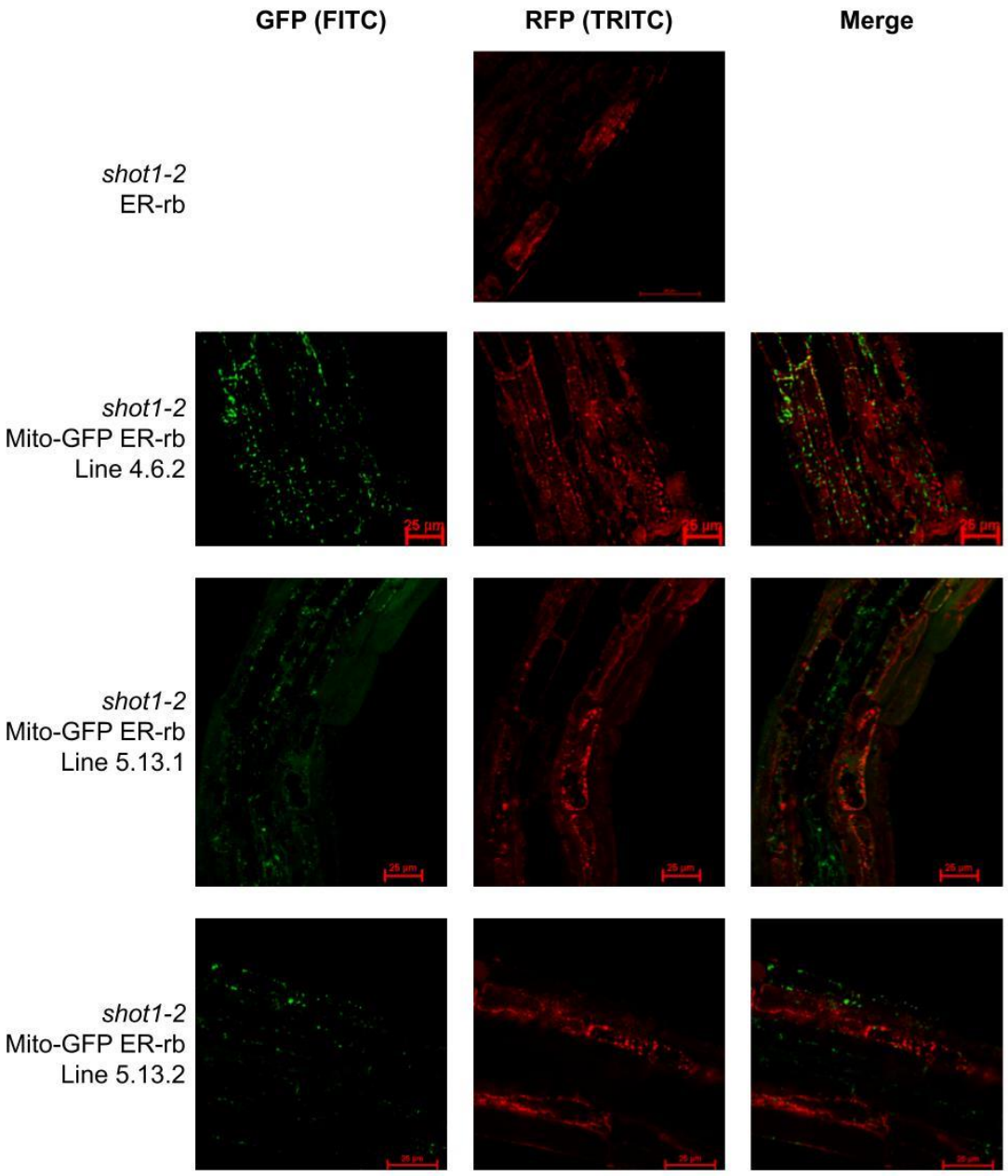

Figure 4.4: Confocal microscopy images of *shot1-2* plants. A single line of *shot1-2*-background plants transformed with ER-rb (1.5.1) was grown for 10 days prior to imaging. Additionally, two separate lines of *shot1-2*-background plants transformed with both Mito-GFP and ER-rb were imaged. Lines indicated at left along with the plant line genotype. Green (FITC) and red (TRITC) channels were used for excitation of fluorescently labelled mitochondria and ER, respectively. All images were captured at 60X zoom in the differentiation zone of the root using the Nikon A1SP confocal microscope. All scale bars represent 25 µm.

In addition to altered mitochondrial puncta size, *shot1-2* plants present a lower rate of signal colocalization as compared to Col-0 plants, which may be indicative of a loss of contact sites. Loss of these contact sites can result in impairment of cholesterol import (Issop et al., 2015; Gerhold et al., 2015), lipid precursor import (Michaud et al., 2016), and failure to correctly localize the mitochondrial fission/fusion machinery (Csordas et al., 2018). Though the available data do not directly detect contact sites, it is reasonable to hypothesize that the *shot1-2* growth phenotype may result in part from impairment of these processes if contact site dynamics are impacted. This lingering question leaves a large avenue of scientific inquiry open for experimentation to further understand the role of *shot1-2* at the mitochondria-ER interface. Future experiments require further examination of the established plant lines, along with computer analysis of microscopy images. Re-imaging these lines and analysis with powerful software tools such as Nikon Elements and ImageJ would allow for the quantification of fluorescent punctae and physical distance between signals. Adding these two sources of data would allow for the analysis of organellar dynamics in the *shot1-2* mutant, which may lead to discoveries in the effects of SHOT1 on contact sites. An important first step will be to repeat imaging of the available lines. Collecting more image data is a key step to defining actual ERMCS changes.

Another approach to understanding mitochondria-ER dynamics in the *shot1-2* mutant would be to assess its effects on mitochondrial and perhaps ER motility. Previous studies with fluorescently labelled organelles in plants, also using confocal microscopy, have shown that mitochondria are dependent upon ER tubules for fission/fusion processes, in addition to motility (Jaipargas et al., 2015). By adding time lapse imaging techniques in addition to video capture, the established lines can also be used to observe real-time fission, fusion, and motility of the

mitochondrion. Expanding this assay to include these additional aspects can also be used as a method of gauging the phenotypic effects of the *shot1-2* mutants.

Further questions also remain, especially regarding mitochondrial dynamics in the *shot1-2* genotype. Colocalization of discrete domains in the mitochondrial inner and outer membranes are known modulate the association of the mitochondrion and the ER. These domains, known as MAMs, are necessary for ER-mitochondria crosstalk. Previous studies have shown that perturbation of the MICOS complex leads to loss of cristae, and therefore loss of inner and outer membrane contact sites within the mitochondrion (Friedman et al., 2018; Peralta et al., 2018). Considering that SHOT1/mTERF18 may interact with the putative plant MICOS complex, it is important to understand how the *shot1-2* mutation affects the distribution of the MIM, which in turn regulates the association with the MOM and formation of MAMs. Theoretically, the phenotypic changes observed in *shot1* mutants may be dependent upon changes in the MAM and MOM/MIM tethering. This question would require use of technologies such as electron microscopy, as confocal microscopy does not have the resolution required to image these membranes with sufficient detail.

CHAPTER 5 : THE ARABIDOPSIS ERMIONE SYSTEM: A REVIEW

5.1. Introduction

As the techniques and technologies that molecular biologists become more advanced, the questions being posed have evolved to focus on interactions on a molecular level. While it was only 75 years ago that organelles like the ER were discovered, today's advances allow for the dissection of the minutiae that define organelles and their interactions within the eukaryotic cell. One of the earliest discovered contact sites localized to the ER-mitochondria junction, but at the time it was disregarded due to a perceived lack of physiological importance (Scorrano et al., 2019). In the time since, contacts between the plasma membrane-ER, ER-Golgi, and nucleus-vacuole (NVJ) have been observed and noted for their roles in autophagy, calcium and lipid transfer, and cell cycle progression (Scorrano et al., 2019).

The mitochondria-ER contact site is of particular interest due to its multiple and varied functions. Processes that localize to ERMCS (ER-mitochondria contact sites) include lipid precursor import, protein import, calcium diffusion/regulation, and mitochondrial fission/fusion (Wideman and Munoz-Gomez, 2015). To regulate all of these dynamic processes, multiple protein complexes and supercomplexes assemble, the most important of which is the ERMIONE (endoplasmic reticulum-mitochondria organizing network). The definition of the ERMIONE complex is somewhat variable, as it refers to a handful of discreet complexes that cooperate to maintain mitochondrial homeostasis and essential functions. The ERMIONE is composed of two major complexes: i) MICOS (mitochondrial inner cristae organizing system) and ii) ERMES (ER-mitochondria encounter structure). These complexes operate separately and discretely, as they localize to different mitochondrial membranes as suggested by their names. Together, they form a robust ERMIONE complex that mediates interconnected functions from the outer mitochondrial

membrane through to the inner mitochondrial matrix. The ERMIONE and its constituents and role have been well-defined in mammals and fungi. However, there has been little effort to define the plant ERMIONE. As mentioned in Chapter 1, a number of studies show that the SBA protein homolog ATAD3a performs multiple MICOS-like functions and may also be involved in tethering of the ER to the mitochondrion (Csordas et al., 2018). To understand more about the possible role of SBA proteins in a putative plant ERMIONE, it is important to define the context of what is already known about known ERMIONE subcomplexes in plants. The following review aimed to summarize what is known about ERMIONE components and their functions in plants, as well as to discover previously unidentified homologues of mammalian or fungal ERMIONE components through sequence analysis or indications of functional conservation.

5.2. The ERMES complex

The first subcomplex of the ERMIONE is known as the ERMES (ER-mitochondria encounter structure). As its name suggests, it is responsible for contacts between the mitochondrial outer membrane and the ER membrane - a region also known as the MAM (mitochondria associated membrane). The ERMES complex has so far only been found in *Saccharomyces cerevisiae*, in which it consists of four known subunits: Mmm1 (maintenance of mitochondrial morphology), Mdm10 (mitochondrial distribution and morphology), Mdm12, and Mdm34 (Table 5.2; Kundu and Pasrija., 2020). Phylogenetic analyses of these ERMES subunits showed no direct homologs or paralogs for these subunits in plants (Wideman and Munoz-Gomez, 2015).

Studies in yeast have identified many different functions of the ERMES complex. The first is lipid transport. Since the mitochondrion is alphaproteobacterial in origin, there are certain lipid precursors needed for mature lipid product formation in the mitochondrion. One example is

the import of phosphatidylserine (PS), which is then converted to phosphatidylethanolamine (PE) (Michaud et al., 2016). Mutations in the ERMES complex in yeast alter lipid composition of the mitochondrion, showing that ERMES is indeed partially responsible for lipid import into mitochondria (Tan et al., 2013). Interestingly, ERMES subunits all contain a synaptotgamin-like, mitochondrial and lipid-binding protein (SMP) domain, which is thought to mediate lipid trafficking by ERMES subunits (AhYoung et al., 2015). Other SMP proteins in yeast that are not ERMES subunits also support lipid trafficking (Kundu and Pasrija, 2020), which opens the possibility that SMP-containing proteins in plants are a "missing link" of ERMES-like function. Though there are SMP-like protein homologues in plants, none have been specifically identified as performing ERMES functions, leaving open an interesting question as to the existence of ERMES in plants (Wong and Levine, 2017).

The main purpose of the ERMES complex is to tether the ER to the mitochondrion at contact sites. Tethering not only holds the organelles together for other processes (lipid trafficking, Ca^{+2} influx), but also marks the areas where mitochondria undergo fission and fusion. In previous studies conducted with yeast, mutants missing one or more of the core ERMES subunits did not divide properly, and puncta where fusion would normally occur were not observed (Smethurst and Cooper, 2017). Given the indispensable roles of yeast ERMES core subunits in tethering and lipid metabolism, it would appear strange that there are no direct orthologs outside of a few non-fungal lineages (Wideman et al., 2013). This begs the question of whether there are compensatory protein complexes in plants that perform these functions in the place of ERMES. So far, only one plant protein has been identified as a possible ERMES replacement: mitochondria/ER-localized LEA-related lysM domain protein 1 (MELL1, Pp3c22_5700V3.1). This protein, identified in the moss *Physcomitrella patens*, appears to colocalize to both the ER membrane and mitochondrial outer membrane. In the only publication

on this topic, researchers overexpressed MELL1 in *P. patens* and observed changes in mitochondrial morphology (Mueller and Reski, 2015). This was accomplished via the mtEOS fluorophore, which typically fluoresces in the green range until excited with ultraviolet light (Mathur et al., 2010). This system provided a framework for a FRAP (fluorescence recovery after photobleaching)-like assay where MELL1 could be tracked throughout subcellular compartments. MELL1 was observed to localize to ERMCS through the use of fluorescently labelled ER membrane proteins and confocal microscopy. It was noted that MELL1 overexpression increased the sphericity of mitochondria, while mitochondrial number and surface area decreased. Additionally, MELL1-overexpression lines showed increased contact sites between the mitochondria and ER (Mueller and Reski, 2015). This phenotype appears similar to those seen in Mmm1, Mdm10, Mdm12, and Mdm34 mutants in yeast, which further demonstrates that there is at least some similarity or overlap between MELL1 and ERMES subunits. Though the authors demonstrated that MELL1 performs ER-mitochondria tethering in *P. patens*, sequence alignment does not show any relevant homologs in *A. thaliana*. With all things considered, it does not appear likely that an ERMES system with components directly homologous to those in yeast exists in *A. thaliana*. Sequence analysis shows no homologues to core yeast ERMES proteins or MELL1. However, the lack of an ERMES system does pose an interesting thought: ER-mitochondria tethering is considered essential in multiple inter-organellar processes, leaving the question of which *A. thaliana* proteins are left to perform these key functions. The structure of human ATAD3a, as well as its ability to contact both the ER membrane and MOM (Csordas et al., 2019), suggests that SBA proteins may be responsible for ERMES-like functions in plants.

5.3. The MICOS complex

The second half of the canonical ERMIONE system is the mitochondrial inner cristae organizing system, the MICOS (or sometimes MINOS) complex. Although ERMES is considered more ancient than MICOS, phylogenetic analyses show that it is in fact the MICOS system that is more well-conserved. At least one subunit of the MICOS complex has been found in all eukaryotes with mitochondrial cristae, a conservation not seen with the ERMES system (Wideman and Munoz-Gomez, 2015). As the name implies, the MICOS complex resides on the mitochondrial inner membrane and is comprised of various subunits (Figure 5.1). In yeast MICOS is composed of Mic10, Mic12, Mic19, Mic26, Mic28, and Mic60 subunits (Wideman and Munoz Gomez, 2015), whereas the human MICOS system contains Mic10, Mic13, Mic14, Mic19, Mic23, Mic25, Mic27, and Mic60 (Kozjak-Pavlovic, 2017). The most conserved subunits are Mic60, Mic19, and Mic10, with others varying based on organism. Together, these subunits are responsible for three main functions: marking crista junctions, tethering the mitochondrial inner and outer membranes, and maintaining the nucleoid of the mitochondrion. Based on previous studies, it is considered that there are two distinct MICOS subcomplexes: the first comprised of Mic60 and Mic19, and the second comprised of Mic10, Mic12, and homologs of Mic26 and Mic28.

5.3.1. The Mic60 subcomplex

Mic60 has a special distinction in that it has so far been identified in the most organisms when compared with other MICOS subunits. In addition to vertebrates and fungi, Mic60 has been identified in alphaproteobacterial species as well as plants, suggesting that it is the most ancient MICOS complex subunit. Sequence analysis via multiple alignment of Mic60 in humans, fruit flies, yeast, and plants show little sequence identity (Figure 5.2A). Human and *Drosophila*

sequences have the highest (29%) identity, though the *A. thaliana* sequence did not show more than 21% identity with any of the other sequences. The alignment itself showed that there were no regions of significant homology. The C-terminal region did show some areas of similarity, as it contains the conserved mitofilin domain (Figure 5.2B; Wollweber et al., 2017).

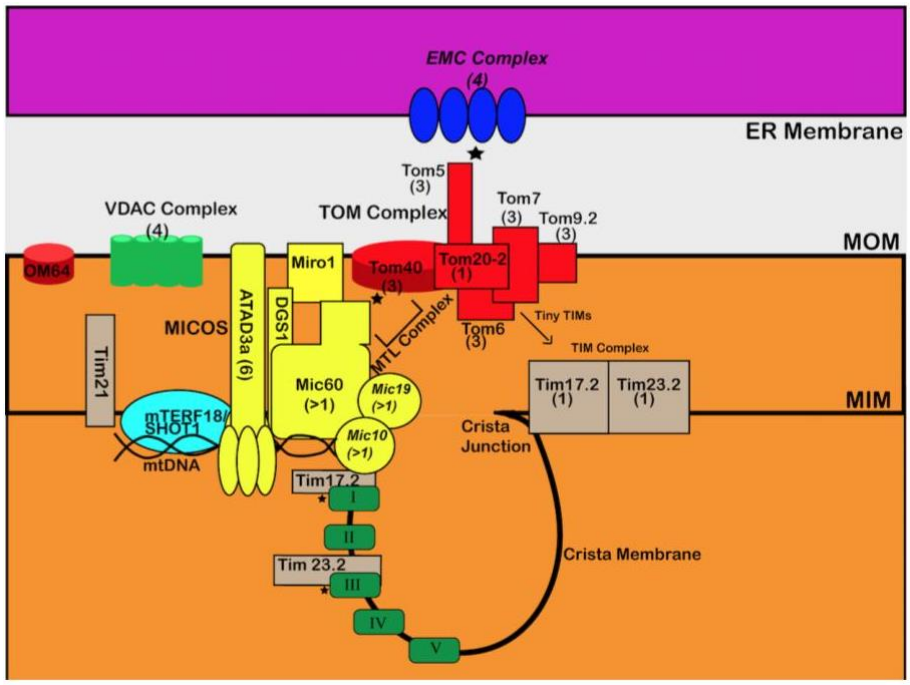

Figure 5.1. Illustration of the known plant ERMIONE system and constituent complexes. ERMIONE proteins were identified through a literature search and illustrated above. Yellow: known MICOS/MICOS-like proteins, red: TOM complex, brown: TIM complex, green: OXPHOS complexes, blue: EMC complex. Subunits that are predicted by sequence homology but not experimentally found *in-vivo* are demarcated with italicized text. Stars indicate known contact sites and interactions between different proteins. Abbreviations: MOM: mitochondrial outer membrane, MIM: mitochondrial inner membrane, MICOS: mitochondrial inner cristae organizing system, MTL: mitochondrial transmembrane lipoprotein complex, EMC: ER membrane complex, TOM: translocase of the outer mitochondrial membrane, TIM: translocase of the mitochondrial inner membrane, VDAC: voltage dependent anion channel, SHOT1: suppressor of *hot1-4*, OM: outer membrane protein

In previous work in yeast, it was found that deletion of Mic60 caused numerous effects, such as loss of foci for other MICOS subunits, as well as loss of cristae junctions. Conversely, retaining Mic60, but mutating other MICOS subunits still led to proper Mic60 localization (Friedman et al., 2018). Other work reported that Mic60 mutation also led to destabilization of the entirety of the mitochondrial inner membrane, as well as loss of anchoring to the outer membrane (Wollweber et al., 2017). In cross-linking experiments using human cardiac mitochondria, it was shown that Mic60 not only interacted with proteins from the Mic10 subcomplex, but also with proteins in the TOM (translocase of the outer membrane) and SAM (sorting and assembly machinery) complexes of the mitochondria. Interestingly, the association of the Mic60 subcomplex with TOM remained stable even in the absence of the Mic10 subcomplex (Wollweber et al., 2017). These data suggest that Mic60 functions both on its own and in concert with other MICOS subunits.

In addition to contacts with the TOM and SAM complexes in yeast, Mic60 facilitates the recruitment of the MIA (mitochondrial intermembrane space assembly) complex to the TOM complex to efficiently import preproteins. This process is mediated via the recruitment of the MIA40 subunit to TOM40, where preproteins can then form disulfide bonds for an exchange from the OMM to the IMS (Bohnert et al., 2012).

In terms of the complex as a whole, it is believed that Mic60 demarcates emerging crista junctions. In genetic ablation models of yeast Mic60, cristae fail to form, and overexpression of Mic60 causes the formation of multiple branched cristae (Rabl et al., 2009). Similarly, deletion of Mic19 also causes loss of cristae junctions, but not as severely as with loss of Mic60 (Wollweber et al., 2017). Mic19 serves a unique purpose, as it interacts with Mic27 in the yeast model and serves as a bridging scaffold between the Mic60 and Mic10 complexes (Friedman et al., 2018).

Even with the wealth of knowledge gathered on the MICOS complex in recent years, information on the presence or function of a plant MICOS system remains scant. However, a recent publication focusing on plant lipidomics identified Mic60 in *A. thaliana*, making it the first known MICOS subunit in plants (Michaud et al., 2016). These authors describe a mitochondrial transmembrane lipoprotein complex that they discovered using radiolabeled digalactosyldiacylglycerol (DGDG). This lipid is typically produced in the chloroplast and imported into mitochondrion under phosphate starvation conditions. *A. thaliana* mitochondria were isolated from plant cell cultures grown under both (+) and (-) P_i conditions and then separated using clear-native PAGE. Using anti-DGDG antibodies, it was found that Mic60 colocalized with a majority of the radiolabeled DGDG, as well as other plant mitochondrial proteins (Michaud et al., 2016).

A

	P36112 MIC60 Yeast	Q9ASV5 MIC60 Arabidopsis	Q16891 MIC60 Human	P91928 MIC60 Drosophila
P36112 MIC60 Yeast	100.00	18.58	15.66	16.97
Q9ASV5 MIC60 Arabidopsis	18.58	100.00	21.16	20.18
Q16891 MIC60 Human	15.66	21.16	100.00	29.10
P91928 MIC60 Drosophila	16.97	20.18	29.10	100.00

B

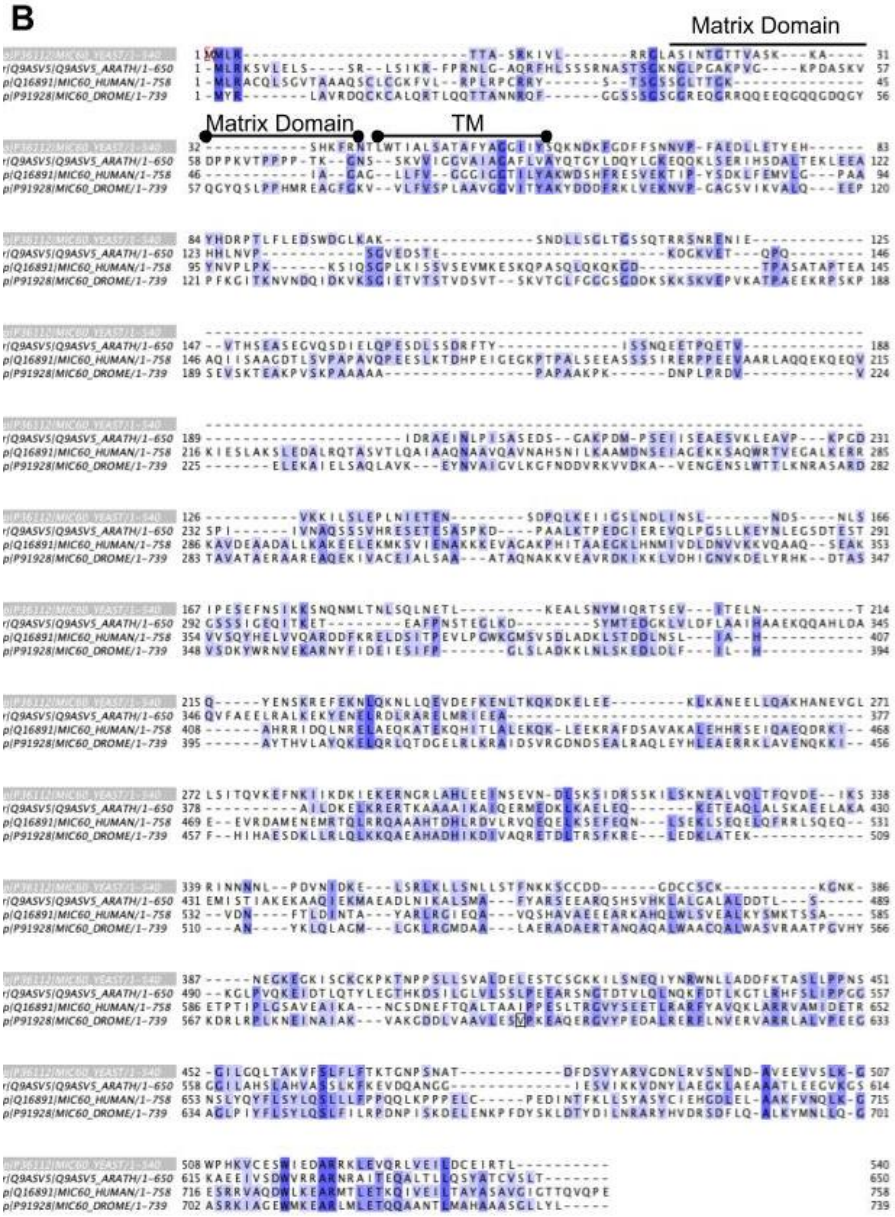

Figure 5.2: Sequence alignment of Mic60 in humans, plants, yeast, and fruit flies. (A) Sequence identity matrix of Mic60 amino acid transcripts. Sequences from each species (with UniProt accession numbers shown) were aligned using Clustal Omega (https://www.ebi.ac.uk/Tools/msa/clustalo/) multiple sequence alignment. Sequence identity was automatically calculated by the program. Matrix shows identity of each sequence to itself and the three other queries. **(B)** Multiple sequence alignment of Mic60 proteins. Raw data from Clustal Omega was processed using JalView. Amino acid residues were shaded based on identity and similarity score, with differing regions left unshaded. Matrix localized and transmembrane domains demarcated above. The remainder of the Mic60 protein is considered to be the conserved intermembrane space/mitofilin domain.

Additionally, multiple subunits of the TOM complex were found within this fraction as well, which demonstrates a dedicated subcomplex responsible for the import and localization of lipids through the MICOS complex. This is of particular interest, since lipid transport has remained a poorly defined area of MICOS research. Further experiments also showed that Mic60 co-immunoprecipitates with TOM40, and that it is also able to bind lipids directly (Michaud et al., 2016). Similar to what is observed in *mic60* mutants in yeast (Friedman et al., 2018), T-DNA knockout lines of AtMic60 showed that mitochondria were enlarged, with poorly formed cristae. These data demonstrate that Mic60 exists in plants, and that its role is important for both lipid import and cristae formation.

5.3.2. The Mic10 subcomplex

The second half of the canonical MICOS complex is the Mic10 subcomplex. Based on previous work in yeast, this subcomplex contains Mic10, Mic12 (Mic13/QIL1 in humans), Mic26, and Mic27 (Wollweber et al. 2017). *A. thaliana* genomic and transcriptomic analyses have so far provided evidence for only one subunit of the MIC10 subcomplex- a Mic10 homolog (Table 5.2). However, this protein has not been verified through *in vivo* research (Wollweber et al., 2017, Wideman and Munoz-Gomez 2015). Sequence alignment of *A. thaliana* Mic10 to

homologs from humans, fruit flies, and yeast shows that there is some sequence identity, with 31% identity between *A. thaliana* and humans (Figure 5.3A). The same analysis also shows that the *A. thaliana* Mic10 protein only shares 22% sequence identity with yeast Mic10, the most well-characterized homolog from the analysis (Figure 5.3A). In the alignment itself, there are a few regions of significant homology between the different sequences, namely in the transmembrane domain. The Mic10 subunit requires oligomerization through conserved glycine residues in the coiled-coil domain, without which it is unable to perform membrane shaping activities both *in vivo* and *in vitro* (Bohnert et al., 2015). Within the coiled-coil domain, it does appear that only one out of two glycine residues are conserved in *A. thaliana s* (G35), which may have effects on the ability of Mic10 to oligomerize *in vivo* (Figure 5.3B).

In addition to membrane shaping, the Mic10 oligomeric complex has been shown to interact with the ATP synthase complex and promote its dimerization for proper function, a function that is not seen in the Mic60 subcomplex (Rampelt et al. 2017). The components of the yeast Mic10 subcomplex (Mic10, Mic12, Mic26, and Mic27), are predicted to reside on established crista junctions in close proximity to respiratory complexes, especially ATP synthase (Figure 5.1, Table 5.1, 5.2). In terms of mutant phenotypes, ablation of Mic60 or Mic10 has been observed to cause the most drastic changes in cellular respiration and mitochondrial membrane topology in yeast (Wollweber et al. 2017), but ablation of Mic12 also causes destabilization of the entire complex (Guarani et al., 2015).

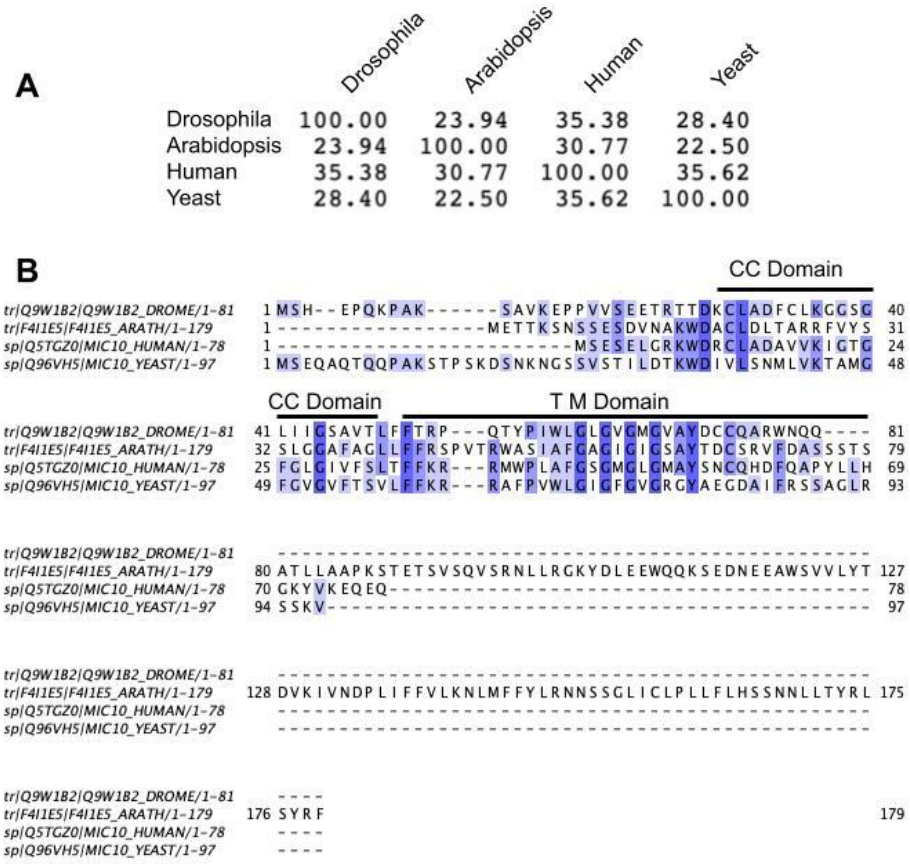

Figure 5.3: Sequence alignment of Mic10 in humans, plants, yeast, and fruit flies. (A) Sequence identity matrix of Mic10 amino acid transcripts. Sequences from each species (with UniProt accession numbers shown) were aligned using Clustal Omega (https://www.ebi.ac.uk/Tools/msa/clustalo/) multiple sequence alignment. Sequence identity was automatically calculated by the program. Matrix shows identity of each sequence to itself and the three other queries. **(B)** Visualized multiple sequence alignment of Mic10 proteins. Raw data from Clustal Omega was processed using JalView. Amino acid residues were shaded based on identity and similarity score, with differing regions left unshaded. The yeast coiled-coil (CC) and transmembrane (T M) domains are demarcated above the alignment (amino acids 36-58 and 59-97, respectively).

Interestingly, Mic12 has not been identified in any transcriptomics or genome sequencing experiments in *A. thaliana*, which conflicts with the proposal that it is an integral MICOS complex protein. Sequence analysis did identify a predicted Mic19 subunit in plants (AGI:

AT4G12340), but with only 15.5% identity and 25% similarity between this sequence and the canonical yeast Mic19 (Figure 5.4), it is hard to say with certainty that the sequence codes for a Mic19 homologues (Wideman and Munoz-Gomez, 2015).

5.3.3. Other MICOS-associated proteins in plants

Apart from the canonical Mic10 and Mic60 subcomplexes, other proteins in plants have been implicated as being involved in the MICOS complex. Chief among these is digalactosyldiacylglycerol-synthase suppressor 1 (DGS1; AGI: AT5G12290). During phosphate limiting conditions, monogalactosyldiacylglycerol (MGDG) is imported from the extraplastidic membrane of the chloroplast into the mitochondrion, where it is converted into digalactosyldiacylglycerol (DGDG) using the DGD synthase enzymes such as DGD1 (Li et al., 2019). To identify proteins involved in this pathway, researchers used a genetic suppressor screen in the background of *dgd1* plants to identify what mutations could restore constitutively active DGDG synthesis independent of DGD1, leading to the discovery of DGS1 (Xu et al., 2008). The first assays to show that DGS1 is a part of the MICOS complex was chemical crosslinking, BN-PAGE, and immunoblotting for DGS1 in crude mitochondrial extracts from *A. thaliana.* This experiment showed that WT DGS1 could be found in crosslinked complexes with Mic60, Tom40, Cyt BC_1, and Tom20-2. Two alleles of *dgs1* were characterized: *dgs1-1* (D457N) and *dgs1-2* (T-DNA insertion, exon 3). Phenotypic analysis of these alleles also showed that Mic60 was more protease accessible in the *dgs1-1* mutant line, even with WT levels of *dgs1-1* expression. This evidence, in addition to the crosslinking results, showed that DGS1 was in contact with Mic60, the key subunit of the entire MICOS system. Additionally, EM images of *dgs1-1* mitochondria showed similar patterns of membrane perturbation to the *mic60* mutants seen by Michaud et al. (2016), implicating DGS1 as a key regulator of mitochondrial membrane morphology (Li et al.,

2019). Furthermore, import of key nuclear-encoded mitochondrial proteins, AOX (alternative oxidase) and ANT (adenine nucleotide carrier), was impaired in *dgs1* mutant lines, indicating impairment of plant mitochondria due to this mutation. Still, the exact function of DGS1 in relation to the MICOS system remains elusive due to lack of additional studies on the MICOS complex in plants.

Apart from DGS1, other MICOS-like proteins have been identified in plants - namely, Miro1 (Table 5.2). This family of GTPases is distinguished by its calcium binding EF-hand motifs and role in the microtubule-dependent transport of mitochondria (MacAskill et al., 2009). The Miro family of proteins in *A. thaliana* contains both Miro1 and Miro2, which share 36% and 38% identity with human Miro1/Miro2 (Yamaoka et al., 2008). Both Miro1 and Miro2 have been well-defined in human systems using neuronal and HeLa cells. In these experiments, a few key characteristics of MICOS dysfunction were observed in *miro1 miro2* double knockout models (DKO). Firstly, electron microscopy of DKO cells showed that mitochondria were swollen, elongated, and had poor distribution of cristae. Furthermore, this was shown to be a MICOS-independent phenomenon as expression of MICOS subunits remained constant between WT and DKO cells (Modi et al., 2019). In addition to dysregulation of mitochondrial and cristae morphology, DKO mitochondria were found to be significantly delayed in uptake of calcium via the inositol 1, 4, 5-triphosphate receptor (IP3R)- voltage dependent anion channel (VDAC) axis, a key regulator of calcium transport between the ER and mitochondrion (Decuypere et al., 2011; Modi et al., 2019). These data suggest that Miro1 and Miro2 in human cells are responsible for not only mitochondrial cristae maintenance and biogenesis, but also for mediating interorganellar functions at the ERMCS interface.

Using chemical crosslinking and immunoprecipitation in mammalian cells, the Modi et al. group also showed that Miro1 and Miro2 associated with Mic60 and Mic19, two subunits of

the MICOS complex. Both of these proteins are members of the Mic60 subcomplex, known to associate with TOM40 at the MOM. However, the same immunoprecipitation analyses did not show any evidence of interaction with TOM40. Additionally, no association between Miro1/Miro2 and subunits of the Mic10 subcomplex were seen. Since Mic60 demarcates *de novo* sites of crista junctions, it is therefore believed that Miro1/Miro2 act as adaptors between the MOM and cristae biogenesis machinery (Mic60 subcomplex) of the MIM (Modi et al., 2019). This hypothesis is also supported by the observation that Miro1/Miro2 localize to discreet domains of the MOM where they are in close proximity to the Mic60 subcomplex (Figure 5.1).

From a plant perspective, relatively little has been published about the role of Miro1/Miro2. Previous studies have shown that only Miro1 mutants cause an obvious impact on plant development, specifically in embryonic development (Yamaoka et al., 2008, 2011). To ascertain the phenotype of Miro1 mutants, heterozygous *miro1* plants harboring a T-DNA insertion between the 12^{th} intron and 13^{th} exon were obtained. This line (EMB2473) also contained a homozygous *quartet1* mutation that causes mature pollen grains to remain attached to each other (Yamaoka et al., 2008). To examine the embryonic effects of Miro1 mutation, a construct was transformed into both *miro1* and WT lines wherein mito-GFP was expressed under the DD45 (embryo-specific gene) promoter (Yamaoka et al., 2011). This allowed visualization of mitochondrial dynamics in the context of Miro1. Microscopy using this fluorescent system showed a lowered number of mitochondria per egg cell in the *miro1* plants, many of which were enlarged as compared to WT (Yamaoka et al., 2011). These data, though incomplete, show that Miro1 is responsible for mitochondrial morphology in plants. It also shows that *miro1* mitochondria display similar phenotypes to other MICOS-subunit mutants from humans, plants, and fungi, suggesting that Miro1 is a member of the plant MICOS system.

5.4. The TOM complex

Though the ERMES and MICOS systems serve different purposes, they are inherently connected through the TOM complex. TOM, or translocase of the outer membrane complex, consists of multiple subunits, many of which have defined plant homologs. The *A. thaliana* TOM complex contains the known proteins TOM5, TOM6, TOM7.1, TOM7.2, TOM9, and TOM40 (Werhahn et al., 2003). Additionally, there are four TOM20 proteins in plants (TOM20-1 to TOM20-4), but experimental evidence shows that only TOM20-2 to TOM20-4 are expressed in *A. thaliana* (Lister et al., 2007). Studies with yeast were the first to investigate the biogenesis of the TOM complex within the mitochondrial intermembrane space. In these assays, TOM40 associates with the SAM (sorting and assembly machinery) complex following mitochondrial import, at which point subunits TOM5 and TOM6 associate with the larger TOM40 protein. Following this first assembly step, TOM7 and three subunits of TOM22 coordinate with the TOM5-6-40 complex to form the mature protein import machinery. The additional component, TOM20, resides on the outer mitochondrial membrane, where it loosely associates with the mature TOM complex for proper functioning (Shiota et al., 2015).

Plant TOM maturation is similar to the process in yeast. Though there are four isoforms of plant TOM20, only three of these are documented to be expressed and present in the TOM complex (Werhahn et al., 2003). Another key point is that there is no TOM22 protein in plants; instead, the isoform TOM9.2 replaces many of the key functions of TOM22, though this protein is truncated compared to its yeast homolog (Parvin et al., 2017).

The largest protein in the plant TOM complex is TOM40, a ß-barrel protein mostly implicated in chaperoning mitochondrial protein import (Hu et al., 2019). TOM40 in yeast and plants are highly related, and many of the key functions are conserved. One of these features is the recognition of cleavable mitochondrial import presequences, which are recognized by TOM40

during the import of applicable proteins. AtTOM40 has been implicated in a few developmental roles in *A. thaliana*, specifically in embryonic development. Mutations within the AtTOM40 gene caused irregular embryo development and disrupted mitochondrial biogenesis in multiple plant tissues (Hu et al., 2019). Additionally, knockout of the AtTOM40 gene caused issues with seed development; seed abortion rates were highly elevated in the *tom40* mutant plants (Hu et al., 2019).

An additional interesting feature of the *tom40* mutant is its effect on relative expression of other TOM complex subunits. In a qRT-PCR experiment, researchers found significant upregulation of transcripts coding for TOM5, TOM6, TOM7.2, and all three TOM20 isoforms (Hu et al., 2019) in *tom40-1* ovules. These data support previous hypotheses that TOM40 is the keystone subunit of the TOM complex, and upregulation of other components could compensate for the loss of TOM40. Interestingly, the same qRT-PCR experiments on other mitochondrial outer membrane protein transcripts showed a drastic decrease in PHB (AGI: AT2G34710), coding for the mitochondrial prohibitin/phabulosa protein. The prohibitin complex functions in mitochondrial morphogenesis and cristae formation (Merkwirth and Langer, 2009), though it had not been tied to either the TOM or MICOS complexes previously. These observations connect the TOM complex to PHB and its interaction with the OPA1 GTPase, a core component of the mitochondrial fusion process (Merkwirth and Langer, 2009).

The other characterized protein of the plant TOM system is TOM9.2. Although there are two different isoforms, TOM9.2 is the only one that is expressed (Parvin, 2017). Previous studies have shown that TOM22 (yeast) does not have an applicable plant homolog (Wehrhahn et al., 2003), but there is some sequence similarity between TOM9.2 (plant) and TOM22 (yeast). The TOM9.2 protein is smaller than its yeast homolog, but it is able to bind the cytosolic domain of plant TOM20, mirroring a known function of yeast TOM22 (Rimmer et al., 2011). TOM9.2 also

shares a conserved 16 amino acid transmembrane domain with TOM22 (Macasev et al., 2004). In yeast studies, this TOM22 transmembrane domain was found essential for coordinating TOM40 molecules in the assembly of the TOM holo-complex (Shiota et al., 2015). Plant data also showed that TOM9.2 knockdown via RNAi methods did not impact the levels of TOM40 protein nor the association between TOM40 and TOM20. It did, however, show that the import of TOM40 was severely impacted in the TOM9.2 mutant, showing that plant homolog TOM9.2 may have some of the conserved function of yeast TOM22 (Parvin et al., 2017).

Though not much is known about many of the other TOM complex subunits in plants, a few key characteristics of TOM5 from yeast data are re-defining what is known about the plant ERMIONE system. In yeast experiments focusing on the trafficking of phospholipids from the ER to the mitochondria, it was seen that the EMC (ER membrane complex) was essential for these lipid import mechanisms (Lahiri et al., 2014). Furthermore, cells lacking components of either the EMC or ERMES complex were unable to support lipid homeostasis and ER-mitochondria tethering, which in most cases caused cell death. Further, both of these functions were restored in an ERMES-mutant background through the use of a chimeric tethering protein, showing that many of the key biological processes between the ER and mitochondria are highly dependent upon tethering in close proximity (Lahiri et al., 2014).

In addition to investigating EMC-ERMES interactions, the authors also tested the interactions between TOM5 (for which there is a plant homolog) and EMC. In all cases, they saw that TOM5 not only interacted with all six of the EMC proteins, but that the interaction persisted *in-vivo* when the transmembrane segment of TOM5 was mutated. Since TOM5 is a membrane-anchored protein, it is hypothesized that their interaction depends on sequence motifs that allow TOM5 to localize to its interacting partners (Lahiri et al., 2014). Finally, the authors also showed that TOM5 colocalized to discrete puncta of fluorescently-labelled EMC and ERMES proteins,

showing that it is an integral member of the ER-mitochondria tethering complex. Though TOM5 has been identified and studied in *A. thaliana,* the EMC complex has not. Sequencing experiments show that there are four EMC complex subunits in *A. thaliana* (Table 5.2), but the protein products of these genes have not been identified or studied. Still, the defined interplay between TOM5 and the EMC complex presents an exciting avenue of research that could lead to the discovery and finer definition of ER-mitochondria tethering in plants.

5.5. Conclusions and further work on the plant ERMIONE system

The ERMIONE system is a complex assortment of mitochondrial and ER-related proteins that spans three different membranes and that is not fully defined in plants. The MICOS system is currently being discovered in plants, and data from other model organisms are available to guide the search for more components. Though no ERMES system proteins homologous to those found in yeast are present in plants, compensatory proteins may perform the functions of tethering and lipid trafficking, such as MELL1 (Mueller and Reski, 2015). The additional discovery of SBA proteins in *A. thaliana* can also lead to further discoveries in the ERMIONE system, especially considering the MICOS-like function of the SBA-homolog ATAD3a.

There are a number of approaches to identifying and characterizing ERMIONE proteins in plants. First, previously performed genome sequencing can be used to identify ERMIONE protein homologues. This can be followed up with generating knock-down or knock-out mutants, in tandem with electron microscopy of crude mitochondria from the mutant plants. Since cristae morphology is a hallmark of viable/mutant MICOS subunits, EM could possibly show which subunits are actively involved in cristae maintenance in plants. EM could also help to differentiate the importance of MICOS homologs that are actively involved in plant mitochondrial maintenance and health.

An additional avenue of research would be to use known plant MICOS subunits such as Mic60 as the input for immunoprecipitation, coupled with mass spectrometry to identify immunoprecipitated proteins. Since this type of assay has not yet been performed in plants, it presents an opportunity to probe which plant proteins are associated with the MICOS complex.

Probing the existence of an ERMES-like system in plants is slightly more complicated. Genetic analyses have previously shown that ERMES was lost during evolution at some point before the differentiation of the plant kingdom (Wideman and Munoz-Gomez, 2015), which means that there are no known homologs in plants to compare with yeast. Therefore, it may be prudent to probe the mitochondrial-ER phospholipid exchange pathway, a known process in which tethering is necessary. Generating plants deficient in the ability to perform lipid transfer through perturbation of MTL (mitochondrial transmembrane lipoprotein) complex subunits such as Mic60 or TOM40 could be a possible avenue of investigation, as mitochondria from these and WT plants can be used for proteomics to determine which proteins are necessary for tethering between the plant ER and mitochondria. Once potential homologs are identified, FRET assays can be used to determine tethering interactions. The EMC complex, which resides on the ER side of the MCS, is predicted to exist in plants based on transcriptomics, and could be used as one half of the FRET pair. Using potential candidates from proteomics screening could supply a long list of possible EMC FRET partners, which could help to identify how exactly the process of tethering occurs between the plant ER and mitochondrion.

APPENDIX

A. Glossary of abbreviations

AAA proteins, ATPases associated with diverse cellular activities;

ANT, adenine nucleotide carrier;

AOX, alternative oxidase;

BiFC; bimolecular fluorescence complementation;

BME, ß-mercaptoethanol;

CC, coiled coil;

Col-0, Columbia-0 ecotype (wild-type);

DGD1, DGDG synthase 1

DGDG, digalactosyldiacylglycerol;

DGDS1, digalactosyldiacylglycerol-synthase suppressor 1;

DRP3a, dynamin-related protein 3a;

DSP, (dithiobis(succinimidyl propionate));

DTSSP, (3,3'-dithiobis(sulfosuccinimidyl propionate));

EMC, ER-membrane complex;

EMS, ethane methyl sulfonate

ERMCS, ER-mitochondria contact site;

ERMES, ER-mitochondria encounter structure;

ERMIONE, ER-mitochondria organizing network;

FRAP, fluorescence recovery after photobleaching;

HSP101, heat shock protein 101;

IMS, intermembrane space;

MAM, mitochondria-associated membrane;

MCS, mitochondrial contact sites;

MDM, mitochondrial distribution and morphology;

MGDG, monogalactosyldiacylglycerol;

MERC, mitochondria-ER contact site;

MELL1, mitochondria/ER-localized LEA-related lysM domain protein 1;

MICOS, mitochondrial inner cristae organizing system;

MIM, mitochondrial inner membrane;

MMM, maintenance of mitochondrial morphology;

MOM, mitochondrial outer membrane;

mTERF, mitochondrial transcription termination factor;

MTL, mitochondrial transmembrane lipoprotein complex;

NVJ, nucleus-vacuole junction;

OXPHOS, oxidative phosphorylation;

PE, phosphatidylethanolamine;

PHB; prohibitin/phabulosa;

PRM, proline-rich motif;

PS, phosphatidylserine;

SAM, sorting and assembly machinery complex;

SBA, SHOT1-binding ATPase;

SHOT1, suppressor of *hot1*;

SMP, synaptotgamin-like, mitochondrial and lipid-binding proteins;

SRH, second region of homology;

SUMO, small ubiquitin-like modifier;

TM, transmembrane;

TIM, translocase of the inner mitochondrial membrane complex;

TOM, translocase of the outer mitochondrial membrane complex;

VDAC, voltage-dependent anion channel;

B. Supplementary information

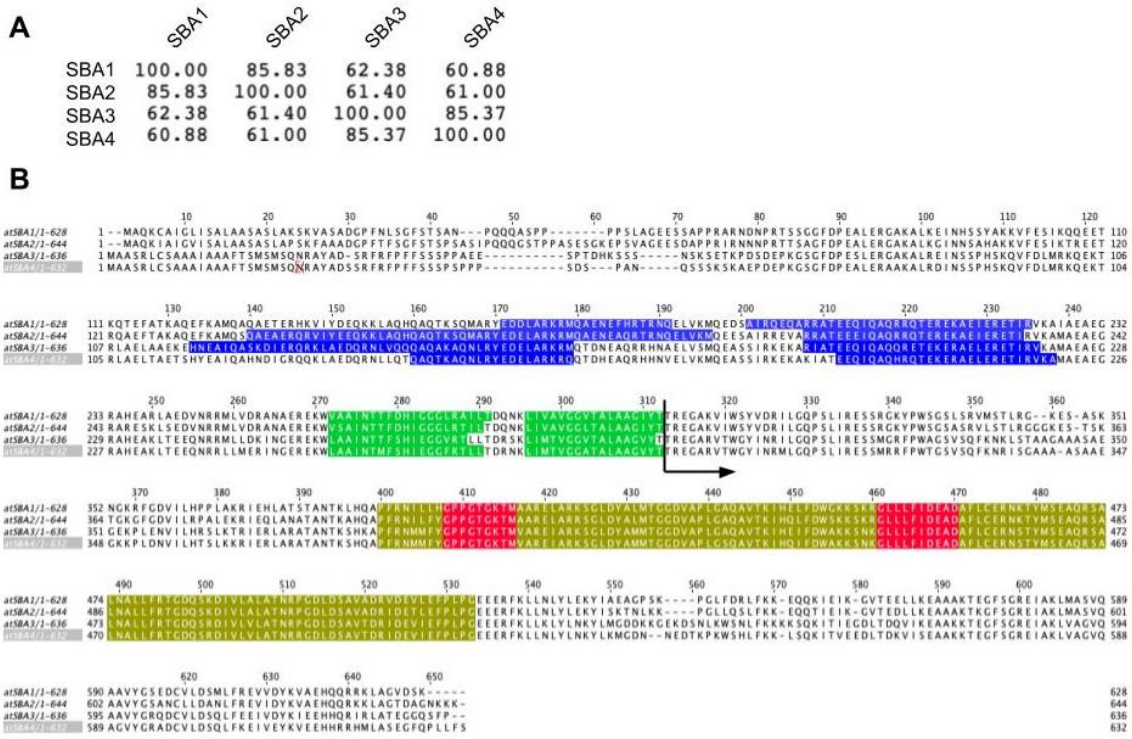

Figure S1: Sequence alignment of *Arabidopsis* SBA proteins. (A) Sequence identity matrix of the four SBA proteins. Percent identity was calculated using the alignment software ClustalOmega ((https://www.ebi.ac.uk/Tools/msa/clustalo/) and shows the sequence identity of each protein transcript in respect to every other sequence input. **(B)** Visualized sequence alignment of SBA1 through SBA4 amino acid transcript. Amino acid sequences of all four SBA proteins were aligned using ClustalOmega software and visualized using JalView (Waterhouse et al., 2009). Blue regions represent coiled-coil domains and green regions show the transmembrane domains as defined in Chapters 1 and 3. The ATPase domain is highlighted in yellow, with consensus Walker A and B motifs demarcated in red. The beginning of the C-terminal fragments that were expressed and purified are shown using the black arrow.

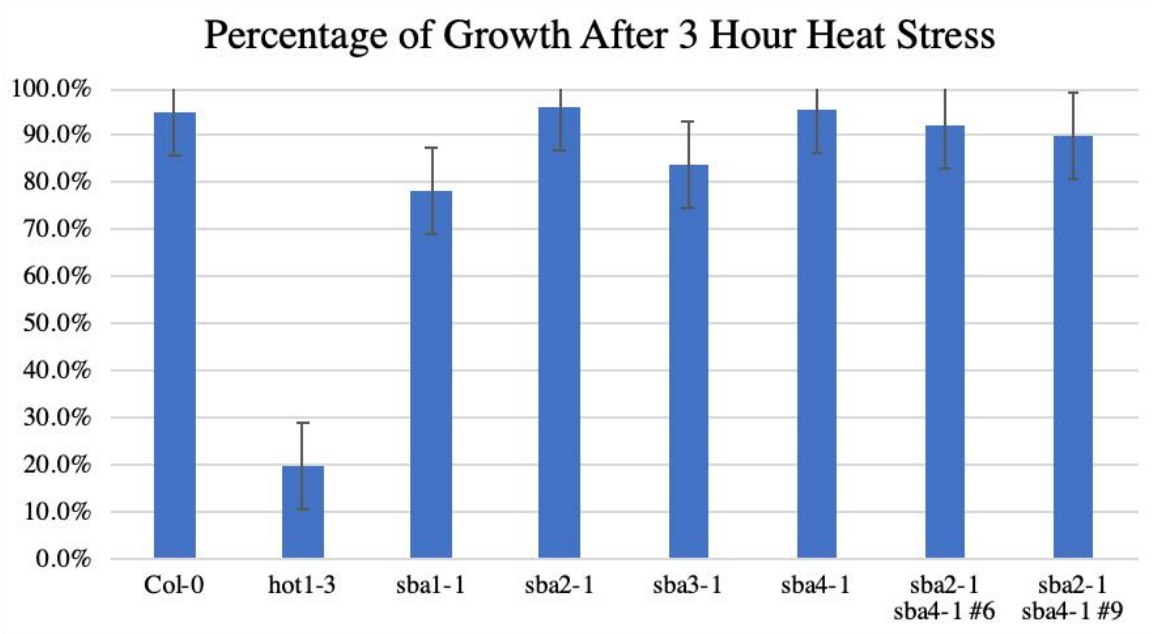

Figure S.2: Thermotolerance assessment of SBA mutant plants via hypocotyl elongation assay. The indicated mutant lines, which include all four SBA single mutants and two lines of *sba2 sba4* double mutants were plated on 1/2X MS media and grown upright for three days, following which they were acclimated to heat at 38°C for 1.5 hours and then subjected to heat stress for 3 hours at 42°C. Plants were then allowed to recover at 22°C in the dark for an additional 3 days. Hypocotyl growth was measured before and after stress conditions using ImageJ, and the ratio of growth before to growth after was calculated. Each bar is an average of between 10-12 individual plants, with standard error displayed.

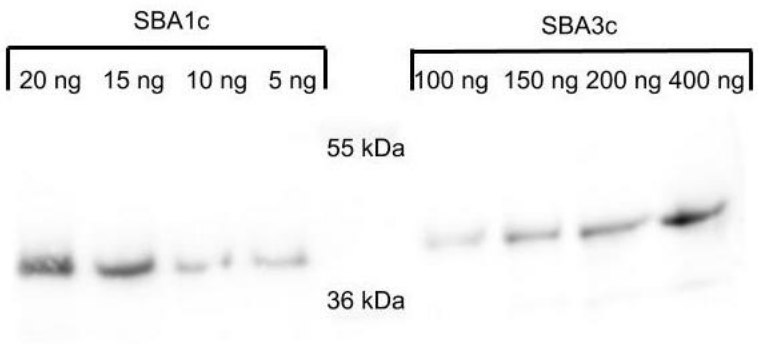

Figure S.3: Immunoblot analysis of anti-SBA1c cross-reactivity. Purified SBA1c and SBA3c were loaded at the specified amounts and run through SDS-PAGE. Following membrane transfer, SBA1c antibody was used as the primary probe. HRP-conjugated secondary antibody and chemiluminescent photo capture were used to visualize results.

REFERENCES

AhYoung, A.P., Jiang, J., Zhang, J., Khoi Dang, X., Loo, J.A., Zhou, Z.H., and Egea, P.F. (2015). Conserved SMP domains of the ERMES complex bind phospholipids and mediate tether assembly. Proc. Natl. Acad. Sci. USA *112*, E3179.

Anderson, A.J., Jackson, T.D., Stroud, D.A., and Stojanovski, D. (2019). Mitochondria-hubs for regulating cellular biochemistry: emerging concepts and networks. Open Biol. *9*, 190126–190126.

Baudier, J. (2018). ATAD3 proteins: brokers of a mitochondria–endoplasmic reticulum connection in mammalian cells. Biol. Rev. *93*, 827–844.

Bellucci, M., De Marchis, F., and Pompa, A. (2017). The endoplasmic reticulum is a hub to sort proteins toward unconventional traffic pathways and endosymbiotic organelles. J. Exp. Bot. *69*, 7–20.

Bohnert, M., Wenz, L.-S., Zerbes, R.M., Horvath, S.E., Stroud, D.A., von der Malsburg, K., Müller, J.M., Oeljeklaus, S., Perschil, I., Warscheid, B., et al. (2012). Role of mitochondrial inner membrane organizing system in protein biogenesis of the mitochondrial outer membrane. Mol. Biol. Cell *23*, 3948–3956.

Bohnert, M., Zerbes, R.M., Davies, K.M., Mühleip, A.W., Rampelt, H., Horvath, S.E., Boenke, T., Kram, A., Perschil, I., Veenhuis, M., et al. (2015). Central Role of Mic10 in the Mitochondrial Contact Site and Cristae Organizing System. Cell Metab. *21*, 747–755.

Cardinal-McTeague, W.M., Sytsma, K.J., and Hall, J.C. (2016). Biogeography and diversification of Brassicales: A 103 million year tale. Mol. Phylogenet. Evol. *99*, 204–224.

Cho, Y., and Kanehara, K. (2017). Endoplasmic Reticulum Stress Response in Arabidopsis Roots. Front. Plant Sci. *8*, 144–144.

Cooper, H.M., Yang, Y., Ylikallio, E., Khairullin, R., Woldegebriel, R., Lin, K.-L., Euro, L., Palin, E., Wolf, A., Trokovic, R., et al. (2017). ATPase-deficient mitochondrial inner membrane protein ATAD3A disturbs mitochondrial dynamics in dominant hereditary spastic paraplegia. Hum. Mol. Genet. *26*, 1432–1443.

Csordás, G., Weaver, D., and Hajnóczky, G. (2018). Endoplasmic Reticulum–Mitochondrial Contactology: Structure and Signaling Functions. Trends Cell Biol. *28*, 523–540.

Decuypere, J.-P., Monaco, G., Missiaen, L., De Smedt, H., Parys, J.B., and Bultynck, G. (2011). IP(3) Receptors, Mitochondria, and Ca Signaling: Implications for Aging. J. Aging Res. *2011*, 920178–920178.

DeSantis, M.E., and Shorter, J. (2012). The elusive middle domain of Hsp104 and ClpB: Location and function. BBA- Mol. Cell Res. *1823*, 29–39.

Dolan, L., Janmaat, K., Willemsen, V., Linstead, P., Poethig, S., Roberts, K., and Scheres, B. (1993). Cellular organisation of the Arabidopsis thaliana root. Development *119*, 71–84.

Duncan, O., Taylor, N.L., Carrie, C., Eubel, H., Kubiszewski-Jakubiak, S., Zhang, B., Narsai, R., Millar, A.H., and Whelan, J. (2011). Multiple lines of evidence localize signaling, morphology, and lipid biosynthesis machinery to the mitochondrial outer membrane of Arabidopsis. Plant. Physiol. *157*, 1093–1113.

Flinner, N., Ellenrieder, L., Stiller, S.B., Becker, T., Schleiff, E., and Mirus, O. (2013). Mdm10 is an ancient eukaryotic porin co-occurring with the ERMES complex. BBA- Mol. Cell Res. *1833*, 3314–3325.

Friedman, J.R., Mourier, A., Yamada, J., McCaffery, J.M., and Nunnari, J. (2015). MICOS coordinates with respiratory complexes and lipids to establish mitochondrial inner membrane architecture. ELife *4*, e07739.

Gerhold, J.M., Cansiz-Arda, Ş., Lõhmus, M., Engberg, O., Reyes, A., van Rennes, H., Sanz, A., Holt, I.J., Cooper, H.M., and Spelbrink, J.N. (2015). Human Mitochondrial DNA-Protein Complexes Attach to a Cholesterol-Rich Membrane Structure. Sci. Rep. *5*, 15292.

Ghifari, A.S., Gill-Hille, M., and Murcha, M.W. (2018). Plant mitochondrial protein import: the ins and outs. Biochem. J. *475*, 2191.

Gilquin, B., Taillebourg, E., Cherradi, N., Hubstenberger, A., Gay, O., Merle, N., Assard, N., Fauvarque, M.-O., Tomohiro, S., Kuge, O., et al. (2010). The AAA^+ ATPase ATAD3A Controls Mitochondrial Dynamics at the Interface of the Inner and Outer Membranes. Mol. Cell. Biol. *30*, 1984.

Gotté, M., Bénard, M., Kiefer-Meyer, M.-C., Jaber, R., Moore, J.P., Vicré-Gibouin, M., and Driouich, A. (2016). Endoplasmic Reticulum Body-Related Gene Expression in Different Root Zones of Arabidopsis Isolated by Laser-Assisted Microdissection. Plant Genome *9*, 1-13.

Guarani, V., McNeill, E.M., Paulo, J.A., Huttlin, E.L., Fröhlich, F., Gygi, S.P., Van Vactor, D., and Harper, J.W. (2015). QIL1 is a novel mitochondrial protein required for MICOS complex stability and cristae morphology. ELife *4*, e06265.

Hayashi, Y., Yamada, K., Shimada, T., Matsushima, R., Nishizawa, N.K., Nishimura, M., and Hara-Nishimura, I. (2001). A proteinase-storing body that prepares for cell death or stresses in the epidermal cells of Arabidopsis. Plant Cell Physiol. *42*, 894–899.

He, J., Cooper, H.M., Reyes, A., Di Re, M., Sembongi, H., Litwin, T.R., Gao, J., Neuman, K.C., Fearnley, I.M., Spinazzola, A., et al. (2012). Mitochondrial nucleoid interacting proteins support mitochondrial protein synthesis. Nucleic Acids Res. *40*, 6109–6121.

Heazlewood, J.L., Tonti-Filippini, J.S., Gout, A.M., Day, D.A., Whelan, J., and Millar, A.H. (2004). Experimental analysis of the Arabidopsis mitochondrial proteome highlights signaling and regulatory components, provides assessment of targeting prediction programs, and indicates plant-specific mitochondrial proteins. Plant Cell *16*, 241–256.

Hoffman, K., and Stoffel, W. TMbase-a database of membrane spanning proteins segments. Biol. Chem. *374*.

Hong, S.W., and Vierling, E. (2000). Mutants of Arabidopsis thaliana defective in the acquisition of tolerance to high temperature stress. Proc. Natl. Acad. Sci. USA *97*, 4392–4397.

Hong, S.W., and Vierling, E. (2001). Hsp101 is necessary for heat tolerance but dispensable for development and germination in the absence of stress. Plant J. *27*, 25–35.

Hong, S.-W., Lee, U., and Vierling, E. (2003). Arabidopsis *hot* Mutants Define Multiple Functions Required for Acclimation to High Temperatures. Plant Physiol. *132*, 757.

Hu, Y., Zou, W., Wang, Z., Zhang, Y., Hu, Y., Qian, J., Wu, X., Ren, Y., and Zhao, J. (2019). Translocase of the Outer Mitochondrial Membrane 40 Is Required for Mitochondrial Biogenesis and Embryo Development in Arabidopsis. Front. Plant Sci. *10*, 389–389.

Huynen, M.A., Mühlmeister, M., Gotthardt, K., Guerrero-Castillo, S., and Brandt, U. (2016). Evolution and structural organization of the mitochondrial contact site (MICOS) complex and the mitochondrial intermembrane space bridging (MIB) complex. BBA- Mol. Cell Res. *1863*, 91–101.

Ikeda, M., Arai, M., Okuno, T., and Shimizu, T. (2003). TMPDB: a database of experimentally-characterized transmembrane topologies. Nucleic Acids Res *31*, 406–409.

Issop, L., Fan, J., Lee, S., Rone, M.B., Basu, K., Mui, J., and Papadopoulos, V. (2015). Mitochondria-Associated Membrane Formation in Hormone-Stimulated Leydig Cell Steroidogenesis: Role of ATAD3. Endocrinology *156*, 334–345.

Jaipargas, E.-A., Barton, K., Mathur, N., and Mathur, J. (2015). Mitochondrial pleomorphy in plant cells is driven by contiguous ER dynamics. Front. Plant Sci. *6*, 783.

Jeong, H., Park, J., Jun, Y., and Lee, C. (2017). Crystal structures of Mmm1 and Mdm12–Mmm1 reveal mechanistic insight into phospholipid trafficking at ER-mitochondria contact sites. Proc. Natl. Acad. Sci. USA *114*, E9502.

Kakimoto, Y., Tashiro, S., Kojima, R., Morozumi, Y., Endo, T., and Tamura, Y. (2018). Visualizing multiple inter-organelle contact sites using the organelle-targeted split-GFP system. Sci. Rep. *8*, 6175.

Kerppola, T.K. (2008). Bimolecular fluorescence complementation (BiFC) analysis as a probe of protein interactions in living cells. Annu. Rev. Biophys. *37*, 465–487.

Kim, M., Lee, U., Small, I., Colas des Francs-Small, C., and Vierling, E. (2012). Mutations in an Arabidopsis Mitochondrial Transcription Termination Factor–Related Protein Enhance Thermotolerance in the Absence of the Major Molecular Chaperone HSP101W. Plant Cell *24*, 3349–3365.

Kim, M., McLoughlin, F., Basha, E., and Vierling, E. (2017). Assessing Plant Tolerance to Acute Heat Stress. Bio-Protocol *7*, e2405.

Kim, M., Schulz, V., Brings, L., Schoeller, T., Kühn, K., and Vierling, E. (2020). Mitochondrial nucleoid organization and biogenesis of complex I require mTERF18/SHOT1 and ATAD3 in *Arabidopsis thaliana*. BioRxiv 2020.05.11.088575.

Kleine, T. (2012). Arabidopsis thaliana mTERF proteins: evolution and functional classification. Front. Plant. Sci. *3*, 233–233.

Kolli, R., Soll, J., and Carrie, C. (2018). Plant Mitochondrial Inner Membrane Protein Insertion. Int. J. Mol. Sci. *19*, 641.

Kozjak-Pavlovic, V. (2017). The MICOS complex of human mitochondria. Cell Tissue Res. *367*, 83–93.

Kruse, B., Narasimhan, N., and Attardi, G. (1989). Termination of transcription in human mitochondria: identification and purification of a DNA binding protein factor that promotes termination. Cell *58*, 391–397.

Kundu, D., and Pasrija, R. (2020). The ERMES (Endoplasmic Reticulum and Mitochondria Encounter Structures) mediated functions in fungi. Mitochondrion *52*, 89–99.

Lahiri, S., Chao, J.T., Tavassoli, S., Wong, A.K.O., Choudhary, V., Young, B.P., Loewen, C.J.R., and Prinz, W.A. (2014). A conserved endoplasmic reticulum membrane protein complex (EMC) facilitates phospholipid transfer from the ER to mitochondria. PLoS Biol. *12*, e1001969–e1001969.

Lee, U., Wie, C., Escobar, M., Williams, B., Hong, S.-W., and Vierling, E. (2005). Genetic Analysis Reveals Domain Interactions of Arabidopsis Hsp100/ClpB and Cooperation with the Small Heat Shock Protein Chaperone System. Plant Cell *17*, 559.

Li, L., Lavell, A., Meng, X., Berkowitz, O., Selinski, J., van de Meene, A., Carrie, C., Benning, C., Whelan, J., De Clercq, I., et al. (2019). Arabidopsis DGD1 SUPPRESSOR1 Is a Subunit of the Mitochondrial Contact Site and Cristae Organizing System and Affects Mitochondrial Biogenesis. Plant Cell *31*, 1856.

Lister, R., Carrie, C., Duncan, O., Ho, L.H.M., Howell, K.A., Murcha, M.W., and Whelan, J. (2007). Functional Definition of Outer Membrane Proteins Involved in Preprotein Import into Mitochondria. Plant Cell *19*, 3739.

Lupas, A.N., and Martin, J. (2002). AAA proteins. Curr. Opin. Struc. Biol. *12*, 746–753.

Macasev, D., Newbigin, E., Whelan, J., and Lithgow, T. (2000). How Do Plant Mitochondria Avoid Importing Chloroplast Proteins? Components of the Import Apparatus Tom20 and Tom22 from Arabidopsis Differ from Their Fungal Counterparts. Plant Physiol. *123*, 811.

Macaskill, A.F., Rinholm, J.E., Twelvetrees, A.E., Arancibia-Carcamo, I.L., Muir, J., Fransson, A., Aspenstrom, P., Attwell, D., and Kittler, J.T. (2009). Miro1 is a calcium sensor for glutamate receptor-dependent localization of mitochondria at synapses. Neuron *61*, 541–555.

Mathur, J., Radhamony, R., Sinclair, A.M., Donoso, A., Dunn, N., Roach, E., Radford, D., Mohaghegh, P.S.M., Logan, D.C., Kokolic, K., et al. (2010). mEosFP-based green-to-red photoconvertible subcellular probes for plants. Plant Physiol. *154*, 1573–1587.

Matsushima, R., Hayashi, Y., Yamada, K., Shimada, T., Nishimura, M., and Hara-Nishimura, I. (2003). The ER Body, a Novel Endoplasmic Reticulum-Derived Structure in Arabidopsis. Plant Cell Physiol. *44*, 661–666.

Merkwirth, C., and Langer, T. (2009). Prohibitin function within mitochondria: Essential roles for cell proliferation and cristae morphogenesis. BBA- Mol. Cell Res. *1793*, 27–32.

Merle, N., Féraud, O., Gilquin, B., Hubstenberger, A., Kieffer-Jacquinot, S., Assard, N., Bennaceur-Griscelli, A., Honnorat, J., and Baudier, J. (2012). ATAD3B is a human embryonic stem cell specific mitochondrial protein, re-expressed in cancer cells, that functions as dominant negative for the ubiquitous ATAD3A. Mitochondrion *12*, 441–448.

Michaud, M., and Jouhet, J. (2019). Lipid Trafficking at Membrane Contact Sites During Plant Development and Stress Response. Front. Plant Sci. *10*, 2–2.

Michaud, M., Gros, V., Tardif, M., Brugière, S., Ferro, M., Prinz, W.A., Toulmay, A., Mathur, J., Wozny, M., Falconet, D., et al. (2016). AtMic60 Is Involved in Plant Mitochondria Lipid Trafficking and Is Part of a Large Complex. Curr. Biol. *26*, 627–639.

Modi, S., López-Doménech, G., Halff, E.F., Covill-Cooke, C., Ivankovic, D., Melandri, D., Arancibia-Cárcamo, I.L., Burden, J.J., Lowe, A.R., and Kittler, J.T. (2019). Miro clusters regulate ER-mitochondria contact sites and link cristae organization to the mitochondrial transport machinery. Nat. Commun. *10*, 4399.

Mogk, A., Schlieker, C., Strub, C., Rist, W., Weibezahn, J., and Bukau, B. (2003). Roles of Individual Domains and Conserved Motifs of the AAA+ Chaperone ClpB in Oligomerization, ATP Hydrolysis, and Chaperone Activity. J. Biol. Chem. *278*, 17615–17624.

Mueller, S.J., and Reski, R. (2015). Mitochondrial Dynamics and the ER: The Plant Perspective. Front. Cell Dev. Biol. *3*, 78.

Murcha, M.W., Elhafez, D., Millar, A.H., and Whelan, J. (2005). The C-terminal region of TIM17 links the outer and inner mitochondrial membranes in Arabidopsis and is essential for protein import. J. Biol. Chem. *280*, 16476–16483.

Murcha, M.W., Kubiszewski-Jakubiak, S., Wang, Y., and Whelan, J. (2014). Evidence for interactions between the mitochondrial import apparatus and respiratory chain complexes via Tim21-like proteins in Arabidopsis. Front. Plant. Sci. *5*, 82–82.

Nakagawa, T., Nakamura, S., Tanaka, K., Kawamukai, M., Suzuki, T., Nakamura, K., Kimura, T., and Ishiguro, S. (2008). Development of R4 gateway binary vectors (R4pGWB) enabling high-throughput promoter swapping for plant research. Biosci. Biotechnol. Biochem. *72*, 624–629.

Nakano, R.T., Yamada, K., Bednarek, P., Nishimura, M., and Hara-Nishimura, I. (2014). ER bodies in plants of the Brassicales order: biogenesis and association with innate immunity. Front. Plant. Sci. *5*, 73–73.

Nelson, B.K., Cai, X., and Nebenführ, A. (2007). A multicolored set of in vivo organelle markers for co-localization studies in Arabidopsis and other plants. Plant J. *51*, 1126–1136.

Parsell, D.A., and Lindquist, S. (1993). The function of heat-shock proteins in stress tolerance: degradation and reactivation of damaged proteins. Annu. Rev. Genet. *27*, 437–496.

Parvin, N., Carrie, C., Pabst, I., Läßer, A., Laha, D., Paul, M.V., Geigenberger, P., Heermann, R., Jung, K., Vothknecht, U.C., et al. (2017). TOM9.2 Is a Calmodulin-Binding Protein Critical for TOM Complex Assembly but Not for Mitochondrial Protein Import in Arabidopsis thaliana. Mol. Plant *10*, 575–589.

Peralta, S., Goffart, S., Williams, S.L., Diaz, F., Garcia, S., Nissanka, N., Area-Gomez, E., Pohjoismäki, J., and Moraes, C.T. (2018). ATAD3 controls mitochondrial cristae structure in mouse muscle, influencing mtDNA replication and cholesterol levels. J. Cell Sci. *131*.

Queitsch, C., Hong, S.W., Vierling, E., and Lindquist, S. (2000). Heat shock protein 101 plays a crucial role in thermotolerance in Arabidopsis. Plant Cell *12*, 479–492.

Rabl, R., Soubannier, V., Scholz, R., Vogel, F., Mendl, N., Vasiljev-Neumeyer, A., Körner, C., Jagasia, R., Keil, T., Baumeister, W., et al. (2009). Formation of cristae and crista junctions in mitochondria depends on antagonism between Fcj1 and Su *e/g*. J. Cell Biol. *185*, 1047–1063.

Rampelt, H., Wollweber, F., Gerke, C., de Boer, R., van der Klei, I.J., Bohnert, M., Pfanner, N., and van der Laan, M. (2018). Assembly of the Mitochondrial Cristae Organizer Mic10 Is Regulated by Mic26–Mic27 Antagonism and Cardiolipin. J. Mol. Biol. *430*, 1883–1890.

Ren, X., and Hurley, J.H. (2011). Proline-rich regions and motifs in trafficking: from ESCRT interaction to viral exploitation. Traffic *12*, 1282–1290.

Rimmer, K.A., Foo, J.H., Ng, A., Petrie, E.J., Shilling, P.J., Perry, A.J., Mertens, H.D.T., Lithgow, T., Mulhern, T.D., and Gooley, P.R. (2011). Recognition of Mitochondrial Targeting Sequences by the Import Receptors Tom20 and Tom22. J. Mol. Biol. *405*, 804–818.

Schwarzländer, M., and Fuchs, P. (2017). Plant mitochondrial membranes: adding structure and new functions to respiratory physiology. Curr. Opin. Plant Biol. *40*, 147–157.

Scorrano, L., De Matteis, M.A., Emr, S., Giordano, F., Hajnóczky, G., Kornmann, B., Lackner, L.L., Levine, T.P., Pellegrini, L., Reinisch, K., et al. (2019). Coming together to define membrane contact sites. Nat. Commun. *10*, 1287.

Shiota, T., Imai, K., Qiu, J., Hewitt, V.L., Tan, K., Shen, H.-H., Sakiyama, N., Fukasawa, Y., Hayat, S., Kamiya, M., et al. (2015). Molecular architecture of the active mitochondrial protein gate. Science *349*, 1544.

Smethurst, D.G.J., and Cooper, K.F. (2017). ER fatalities-The role of ER-mitochondrial contact sites in yeast life and death decisions. Mech. Ageing Dev. *161*, 225–233.

Sun, M., Folk, R.A., Gitzendanner, M.A., Soltis, P.S., Chen, Z., Soltis, D.E., and Guralnick, R.P. (2020). Recent accelerated diversification in rosids occurred outside the tropics. Nat. Commun. *11*, 3333.

Tan, T., Özbalci, C., Brügger, B., Rapaport, D., and Dimmer, K.S. (2013). Mcp1 and Mcp2, two novel proteins involved in mitochondrial lipid homeostasis. J. Cell Sci. *126*, 3563.

Theologis, A., Ecker, J.R., Palm, C.J., Federspiel, N.A., Kaul, S., White, O., Alonso, J., Altafi, H., Araujo, R., Bowman, C.L., et al. (2000). Sequence and analysis of chromosome 1 of the plant Arabidopsis thaliana. Nature *408*, 816–820.

Tusnády, G.E., and Simon, I. (1998). Principles governing amino acid composition of integral membrane proteins: application to topology prediction11Edited by J. Thornton. J. Mol. Biol. *283*, 489–506.

Tusnády, G.E., and Simon, I. (2001). The HMMTOP transmembrane topology prediction server. Bioinformatics *17*, 849–850.

Vale, R.D. (2000). AAA proteins. Lords of the ring. J. Cell Biol. *150*, F13–F19.

Vierling, E. (1991). The Roles of Heat Shock Proteins in Plants. Annu. Rev. Plant. Physiol. Plant. Mol. Biol. *42*, 579–620.

Walter, M., Chaban, C., Schütze, K., Batistic, O., Weckermann, K., Näke, C., Blazevic, D., Grefen, C., Schumacher, K., Oecking, C., et al. (2004). Visualization of protein interactions in living plant cells using bimolecular fluorescence complementation. Plant J. *40*, 428–438.

Wang, W., and Malcolm, B.A. (1999). Two-stage PCR protocol allowing introduction of multiple mutations, deletions and insertions using QuikChange Site-Directed Mutagenesis. Biotechniques *26*, 680–682.

Wang, Y., Carrie, C., Giraud, E., Elhafez, D., Narsai, R., Duncan, O., Whelan, J., and Murcha, M.W. (2012). Dual location of the mitochondrial preprotein transporters B14.7 and Tim23-2 in complex I and the TIM17:23 complex in Arabidopsis links mitochondrial activity and biogenesis. Plant Cell *24*, 2675–2695.

Wang, Y., Law, S.R., Ivanova, A., van Aken, O., Kubiszewski-Jakubiak, S., Uggalla, V., van der Merwe, M., Duncan, O., Narsai, R., Whelan, J., et al. (2014). The Mitochondrial Protein Import Component, TRANSLOCASE OF THE INNER MEMBRANE17-1, Plays a Role in Defining the Timing of Germination in Arabidopsis. Plant Physiol. *166*, 1420.

Waterhouse, A.M., Procter, J.B., Martin, D.M.A., Clamp, M., and Barton, G.J. (2009). Jalview Version 2—a multiple sequence alignment editor and analysis workbench. Bioinformatics *25*, 1189–1191.

Werhahn, W., Jänsch, L., and Braun, H.-P. (2003). Identification of novel subunits of the TOM complex from Arabidopsis thaliana. Plant Physiol. Biochem. *41*, 407–416.

Wideman, J.G., and Muñoz-Gómez, S.A. (2016). The evolution of ERMIONE in mitochondrial biogenesis and lipid homeostasis: An evolutionary view from comparative cell biology. BBA- Mol. Cell Biol. L. *1861*, 900–912.

Wideman, J.G., Gawryluk, R.M.R., Gray, M.W., and Dacks, J.B. (2013). The Ancient and Widespread Nature of the ER–Mitochondria Encounter Structure. Mol. Biol. Evol. *30*, 2044–2049.

Wiese, C., Hinz, J.M., Tebbs, R.S., Nham, P.B., Urbin, S.S., Collins, D.W., Thompson, L.H., and Schild, D. (2006). Disparate requirements for the Walker A and B ATPase motifs of human RAD51D in homologous recombination. Nucleic Acids Res. *34*, 2833–2843.

Winter, D., Vinegar, B., Nahal, H., Ammar, R., Wilson, G.V., and Provart, N.J. (2007). An "Electronic Fluorescent Pictograph" Browser for Exploring and Analyzing Large-Scale Biological Data Sets. PLOS ONE *2*, e718.

Wollweber, F., von der Malsburg, K., and van der Laan, M. (2017). Mitochondrial contact site and cristae organizing system: A central player in membrane shaping and crosstalk. BBA- Mol. Cell Res. *1864*, 1481–1489.

Wong, L.H., and Levine, T.P. (2017). Tubular lipid binding proteins (TULIPs) growing everywhere. BBA- Mol. Cell Res. *1864*, 1439–1449.

Xu, C., Moellering, E.R., Fan, J., and Benning, C. (2008). Mutation of a mitochondrial outer membrane protein affects chloroplast lipid biosynthesis. Plant J. *54*, 163–175.

Yakubovskaya, E., Mejia, E., Byrnes, J., Hambardjieva, E., and Garcia-Diaz, M. (2010). Helix Unwinding and Base Flipping Enable Human MTERF1 to Terminate Mitochondrial Transcription. Cell *141*, 982–993.

Yamaoka, S., Nakajima, M., Fujimoto, M., and Tsutsumi, N. (2011). MIRO1 influences the morphology and intracellular distribution of mitochondria during embryonic cell division in Arabidopsis. Plant Cell Rep. *30*, 239–244.

Zavilgelsky, G.B., Gnuchikh, E.Y., and Melkina, O.E. (2020). Thermostability and Refolding of Proteins in Bacteria Is Determined by the Activity of Two Different ATP-Dependent Chaperone Groups. Mol. Biol. *54*, 300–307.

Zhang, Y., Ma, K., Sadana, P., Chowdhury, F., Gaillard, S., Wang, F., McDonnell, D.P., Unterman, T.G., Elam, M.B., and Park, E.A. (2006). Estrogen-related Receptors Stimulate Pyruvate Dehydrogenase Kinase Isoform 4 Gene Expression. J. Biol. Chem. *281*, 39897–39906.

Zhao, Y., Sun, X., Hu, D., Prosdocimo, D.A., Hoppel, C., Jain, M.K., Ramachandran, R., and Qi, X. (2019). ATAD3A oligomerization causes neurodegeneration by coupling mitochondrial fragmentation and bioenergetics defects. Nat. Commun. *10*, 1371.

Zhou, X., Zhang, J., Pan, Z., and Li, D. (2019). Review of Methods for the Detection and Determination of Malachite Green and Leuco-Malachite Green in Aquaculture. CRC Cr. Rev. Anal. Chem. *49*, 1–20.

Zimmermann, G., Zhou, D., and Taussig, R. (1998). Mutations Uncover a Role for Two Magnesium Ions in the Catalytic Mechanism of Adenylyl Cyclase. J. Biol. Chem. *273*, 19650–19655.

Zorov, D.B., Vorobjev, I.A., Popkov, V.A., Babenko, V.A., Zorova, L.D., Pevzner, I.B., Silachev, D.N., Zorov, S.D., Andrianova, N.V., and Plotnikov, E.Y. (2019). Lessons from the Discovery of Mitochondrial Fragmentation (Fission): A Review and Update. Cells *8*, 175.